Cleveland State University
EngagedScholarship@CSU

ETD Archive

2008

Mems (Micro-Electro-Mechanical-Systems) Based Microfluidic Platforms for Magnetic Cell Separation

Pulak Nath
Cleveland State University

Follow this and additional works at: https://engagedscholarship.csuohio.edu/etdarchive

 Part of the Biomedical Engineering and Bioengineering Commons

How does access to this work benefit you? Let us know!

Recommended Citation

Nath, Pulak, "Mems (Micro-Electro-Mechanical-Systems) Based Microfluidic Platforms for Magnetic Cell Separation" (2008). *ETD Archive*. 218.
https://engagedscholarship.csuohio.edu/etdarchive/218

This Dissertation is brought to you for free and open access by EngagedScholarship@CSU. It has been accepted for inclusion in ETD Archive by an authorized administrator of EngagedScholarship@CSU. For more information, please contact library.es@csuohio.edu.

MEMS (MICRO-ELECTRO-MECHANICAL-SYSTEMS) BASED MICROFLUIDIC PLATFORMS FOR MAGNETIC CELL SEPARATION

PULAK NATH

Bachelor of Science in Chemical Engineering
Bangladesh University of Engineering and Technology
July, 1999

Master of Science in Chemical Engineering
University of Dayton
May, 2002

Submitted in partial fulfillment of requirements for the degree of
DOCTOR OF ENGINEERING IN APPLIED BIOMEDICAL ENGINEERING
at the
CLEVELAND STATE UNIVERSITY
February, 2008

This dissertation has been approved
for the Department of Chemical and Biomedical Engineering
and the College of Graduate Studies by

_____

Dissertation Committee Chairperson, **Aaron J. Fleischman, Ph.D.**
Department of Chemical and Biomedical Engineering

_____

Date

_____

George P. Chatzimavroudis, Ph.D.
Department of Chemical and Biomedical Engineering

_____

Date

_____

Shuvo Roy, Ph.D.
Department of Chemical and Biomedical Engineering

_____

Date

_____

P. Stephen Williams, Ph.D.
Department of Chemical and Biomedical Engineering

_____

Date

_____

Aimin Zhou, Ph.D.
Department of Chemistry

_____

Date

_____

Invited Committee member, **Maciej Zborowski, Ph.D.**
Department of Biomedical Engineering, Cleveland Clinic

_____

Date

Dedicated to my parents, Rohini and Arati Nath

ACKNOWLEDGEMENTS

I would like to express my sincere appreciations to my advisors Dr. Aaron Fleischman, Dr. Shuvo Roy and Dr. Maciej Zborowski for their guidance.

I am grateful to my peers at the BioMEMS laboratory and the Cell Separations Research Laboratory for providing a wonderful work environment. I would like to specially thank Anna Dubnisheva, Illya Gordon, Dr. Stephen Williams and Lee Moore for their trainings and directions.

Finally, my friends and my family – Thank you for your support and friendship.

MEMS (MICRO-ELECTRO-MECHANICAL-SYSTEMS) BASED MICROFLUIDIC PLATFORMS FOR MAGNETIC CELL SEPARATION

PULAK NATH

ABSTRACT

Microfluidic platforms for magnetic cell separation were developed and investigated for isolation of magnetic particles and magnetically tagged cells from a fluidic sample. Two types of magnetic separation platforms were considered: an Isodynamic Open Gradient Magnetic Sorter (OGMS) and a multistage bio-ferrograph. Miniaturized magnets were designed using magnetostatic simulation software, microfluidic channels were fabricated using microfabrication technology and magnetic separation was investigated using video microscopy and digital image processing.

The isodynamic OGMS consisted of an external magnetic circuit and a microfabricated channel (biochip). The biochip is placed inside the magnetic field of the external circuit to obtain nearly constant energy density gradient ($\nabla\left(\frac{B^2}{2\mu_0}\right)$) in the portion of the channel used for separation. A value of $\left|\nabla \boldsymbol{B^2}\right|$ = 0.51±0.01 T^2/mm was obtained over a desired location (850 μm × 250 μm) of the channel cross-section. The biochip consisted of an enclosed microfluidic channel (250 μm thick) with a set of discrete magnetic elements (120 μm thick) embedded in both sidewalls. The key challenge was to integrate enclosed microchannels on transparent substrates with electroplating molds on

the both walls of the channel. The microfabrication process involved improving adhesion of SU-8 to Pyrex, forming enclosed channels using a low temperature SU-8 adhesive bonding, and fabricating patterned plating molds on both sides of the bonded wafers. Adhesion of SU-8 to Pyrex was improved by using a highly crosslinked thin SU-8 adhesion layer, and enclosed microchannels were fabricated using selectively exposed SU-8 bond formation layers. Electroplating molds were fabricated using KMPR photoresists and were integrated on both sides of the bonded wafers.

The multistage bio-ferrograph consisted of a microfabricated enclosed channel placed on the surface of a multi-unit magnet (4 trapezoidal magnets placed in series) assembly such that magnetic cells from a flowing stream would be deposited on designated locations.

The OGMS system and the multistage bio-ferrograph were tested using different concentrations ($10^4 - 10^6/\mu L$) of magnetic particles ($6.4 \pm 0.5 \mu m$) and magnetically labeled Jurkat cells. The OGMS was able to deflect magnetic particles by 500-1000 μm and the capture efficiencies of magnetic particles and cells with the multistage bio-ferrograph were 80-85% and 99.5%, respectively.

TABLE OF CONTENTS

Pages

LIST OF TABLES

Table

LIST OF FIGURES

Figure

Chapter I
Introduction

The ability to isolate rare cells in a biological sample is like finding a few needles in a haystack. However, such ability can be utilized as a medical diagnostic and prognostic tool[1-6]. Certain disease conditions can lead to the presence of cells in the blood stream that are specific to the disease. For example, tumor specific cells can be introduced into circulating blood by the process of metastasis in cancer patients[6]. Nevertheless, the number of these cells can be as low as 1 cell per ml of blood[5,6]. In HIV infected patients, the number of $CD4^+$ cells can indicate the strength of the patient's immune system[7]. Then again, the number of $CD4^+$ cells can be as low as few hundreds per ml for HIV infected patients [8]. Whole blood is a complex mixture of cells (~5×10^9 /ml red blood cells, ~9×10^6 /ml white blood cells and ~3×10^8 /ml platelets) suspended in plasma. As a result, detecting disease specific rare cells from a blood sample for diagnostic purpose would require the superior ability to isolate them from the pool of normal blood cells.

Generally, separation of cells is a sample preparation step where complicated biological samples are simplified by removing unwanted cells. However, technological advances have made several devices available that are capable of separating cells with high specificity and selectivity[9,10]. One such technique is to target the rare cells with antibody coated magnetic micro/nano-particles and separating them with the help of an external magnetic field[11,12]. Most biological material is weakly magnetic and therefore magnetic separation can be highly specific and gentle on the samples. The simplicity of the separation technique also makes it very suitable for miniaturization[13]. Miniaturization of magnetic sorters can help the development of portable devices for medical diagnostic applications at a point of care settings. Point of care testing can reduce the time required to obtain valuable clinical information, which can improve the overall clinical outcome[14].

The long-term goal of the current project is to develop a portable, handheld device for point-of-care medical diagnostic applications based on magnetic separation of rare cells from a clinically relevant biological sample. Therefore, the device should be small, able to effectively isolate and detect disease-specific cells and easy to use. The current goal of this dissertation is to develop miniaturized magnetic and fluidic platforms that are able to perform magnetic separation and deposition of cells form a flowing solution. The separation will be carried out in an isodynamic open gradient magnetic field and the deposition will be performed in a multistage high gradient magnetic field (bio-ferrograph). Fabrication of the microfluidic channels will be carried out using microfabrication technology. Separation and deposition of cells will be analyzed using optical methods such as video microscopy and digital image processing. These

miniaturized separators will be essential components in the development of the final handheld device.

1.1. Specific aims

Specific Aim 1: Design and Fabricate Isodynamic open gradient magnetic module

- Design a magnetic module comprising of discrete pole-pieces with equal width and equal inter pole-piece gap, with height < 300 microns and aspect ratio < 5.
- Develop fabrication techniques of magnetic materials with high saturation magnetization to fabricate the discrete magnetic pole-pieces.

Specific Aim 2: Design and Fabricate microchannel network for separating and depositing cells

- Investigate a microfluidic module that will allow trapping of the fractionated cells on the chip.
- Design and develop a microchannel network to allow sample introduction, cell separation and fractionate collection on the chip.

Specific Aim 3: Investigate cell separation performance using model cell systems

- Construct a flow testing station for the biochip.
- Develop a protocol for separation analysis using fluorescence microscopy.
- Preliminary characterizations of the biochip for flow and cell separation.

1.2. Outline

This dissertation can be divided into three major sections – design, fabrication and demonstration. The first part of the dissertation (Chapter II) discusses the background and significance of key technologies involved in the development of this project. This is a multidisciplinary project that involves technologies such as magnetic cell separation and microfabrication. These fundamental concepts are discussed briefly in this chapter. The limitations with the current state of the art are also identified in this section to establish the challenges with respect to the current development. Finally, the significance of a miniaturized magnetic sorter for medical diagnostic applications is presented.

Chapter III addresses the design aspect of the proposed development. Designing the proposed device was divided into two sections – magnetic design and fluidic design. In each section, the design considerations based on the objective of the project and the limitations with the current technology standards are identified. The objective of the magnetic design was to develop a planar magnetic circuit that is capable of providing nearly constant magnetic field energy density gradient over a certain volume. The magnetic design was carried out using commercial finite element modeling software. Fluidic design was carried out based on the output of the magnetic designs and was performed using conventional fluid mechanics. The results of the design process are also presented in Chapter III.

Although significant attention was devoted to compatibility with microfabrication during the design stage, the final design still posed a few challenges with respect to fabricating the device. These challenges are identified and discussed in Chapter IV. The key challenges were (1) to fabricate enclosed microchannels using SU-8 photoresists on

Pyrex wafers, (2) to fabricate thick plating molds on Pyrex, (3) To electrodeposit Orthonol (Ni50Fe50) according to the molds, and (4) To integrate the microchannels with the electroplating molds. All of these steps except #3 (electrodeposition) was developed as a part of the current development. With respect to the plating, the molds were developed and sent to the external company for electrodeposition. It was critical that the plating molds were stable enough to withstand the plating process.

These individual steps of the fabrication process and challenges were addressed in Chapter V. The overall process development involved improving adhesion of thick SU-8 to Pyrex, bonding wafers to form enclosed microchannels, and preparing thick plating molds on Pyrex.

Although, the challenges associated with the device fabrication were successfully met, process reproducibility with one key material (SU-8) posed new challenges. Therefore, a new material (KMPR photoresist), which only became available in the last year, was investigated for redeveloping part of the fabrication process. The troubleshooting with the process reproducibility is presented in Chapter VI.

The microfabrication processes developed in Chapter V are then utilized to fabricate microfluidic devices for magnetic separation and deposition of cells. The primary apparatus for the proposed device was an open gradient cell sorter. However, the microfluidic cell sorters handle minute amount of samples which yields a very low concentration of fractionated cell sample. These fractions are difficult to quantify for their cell contents. Therefore, a second device (multistage bio-ferrograph), which can deposit cells in particular locations, was designed and developed. The idea was to conjugate the two devices so that magnetically fractionated cells are collected (deposited)

in a specific location for further analysis. Within the scope of this thesis, the two devices were developed and tested separately.

Chapter VII discusses microfluidic characterization of the Open Gradient Magnetic Sorter (OGMS). Experimental setups were developed to perform leak testing, hydrodynamic focusing and magnetic separation with the OGMS channel. Separation of particles was observed using video microscopy.

Chapter VIII presents the development of a multistage bio-ferrograph. A separate magnetic assembly was designed and fabricated for the multistage bio-ferrograph. The enclosed microchannel was fabricated using the process developed in Chapter V. The device was characterized using optical microscopy and digital image processing.

Finally, Chapter IX presents the conclusions and the future outlook for the research and development work presented in this dissertation.

1.3. Individual Contributions

Due to the multidisciplinary nature of the project, several individuals were involved in different aspect of the project. These individual contributions are itemized as follows:

- **Lee Moore, MS** (Cell Separation Research Laboratory, Cleveland Clinic, Cleveland, Ohio):
    - Developed the initial planar magnetic design for an isodynamic OGMS which was not compatible with MEMS fabrication.
    - Developed the computer model to generate contour plots of the magnetic energy density gradient distributions.

- Developed the computer models to simulate particle/trajectories under given magnetic fields.

– **Cell Separation Research Laboratory**, Cleveland Clinic, Ohio
  - Prepared buffer solutions for labeled cells and magnetic particles
  - Maintained cell culture
  - Measured Magnetophoretic Mobility of labeled cells and particles using CTV (Cell Tracking Velocimetry)

– **Joe Strelnik and Harjus Shethi,** Undergraduate Interns, University of Cincinnati, Cincinnati, Ohio
  - Assisted with performing repeat experiments of magnetic cell separation and deposition (e.g. labeling cells, maintaining cell culture, extracting data from digital image processing macros)

– **Anna Dubnisheva, MS** (BioMEMS Laboratory, Cleveland Clinic, Cleveland, Ohio)
  - Performed Scanning Electron Microscopy (SEM) image acquisitions

– **Illya Gordon, MS** (BioMEMS Laboratory, Cleveland Clinic, Cleveland, Ohio)
  - Performed wafer dicing

– **Amit Vasanji, PhD** (Imaging Core, Cleveland Clinic, Cleveland, Ohio)
  - Developed Image Pro macros for digital image analysis applied in this work

– **Integran Technologies, Toronto, Canada**
  - Developed the electroplating process for nanocrystalline alloys of Iron and Nickel in the plating molds developed in this work.

Chapter II
Background

The development of a miniaturized cell sorter was derived from two primary technologies: Magnetic cell separation and Micro-Electro-Mechanical-Systems (MEMS). Magnetic cell separation is a separation technique where specific cells are separated by tagging them with magnetic beads and then sorting them with the help of an external magnetic filed. MEMS technology, on the other hand, is an enabling technology that allows the development of miniaturized products comprising of sensors, actuators and microfluidic components with structures of micro- and nano- meter resolutions.

2.1. Magnetic cell separation

Magnetic separation is a technology that has been in use since as early as the middle of the 19th century for different industrial applications (e.g. mineral processing industry, wastewater management, etc.)[15]. However, the idea of using magnetic separation for biological applications has been considered only since the 1970's. Most biological entities are weakly diamagnetic. Therefore, cells of interest can be magnetically tagged by using magnetic microparticles to achieve magnetic separation by

an external magnet. Magnetic separation of cells using iron containing polymeric micro-spheres was reported by Molday *et al.* in as early as 1977 [16]. Since then, the use of magnetic force in conjunction with magnetic labeling has become an active area of research for cell separation. For example, immunomagnetic techniques that rely on cell surface antigen recognition by an antibody-magnetic particle conjugate have been used for the removal of tumor cells from peripheral blood[17], isolation of antigen specific CD8+ T cells[18], selective separation of CD34+ stem cells[19], etc. Commercial devices using magnetic cell separation techniques (e.g. MACS® technology by Miltenyi Biotec GmbH, Gladbach, Germany; Dynal MPC® by Dynal Biotech, Oslo, Norway; BioMag system by Qiagen, GmbH, Germany; Microtiter well vessel HGMS from Immunicon Corporation, Huntington Valley, PA, USA; MaxSep Magnetic cell separator by Baxter Healthcare Corp., Deerfield, IL; EasySep® by Stemcell Technologies, Vancouver, BC, Canada, etc) are also available in the market.

The magnetic force acting upon a magnetically susceptible particle whose magnetization is a linear function of the applied field is given by [20],

$$\mathbf{F_m} = V\Delta\chi\nabla\left(\frac{B^2}{2\mu_0}\right) \qquad (1)$$

where, V is the particle volume, $\Delta\chi$ is the net particle volumetric susceptibility relative to the medium, μ_0 is the permeability of free space, and $\nabla\left(\frac{B^2}{2\mu_0}\right)$ is the magnetostatic energy density gradient. Equation (1) also provides a satisfactory approximation for cells labeled with superparamagnetic nanoparticles. In this case, the parameter $\Delta\chi$ represents the "effective" net cell volume susceptibility, a weighted average susceptibility of the cell

with the ensemble of the attached nanoparticles, minus the susceptibility of the fluid carrier medium. Depending on how this force is utilized, magnetic separation can be classified into two different categories[21]: (1) High Gradient Magnetic Separation (HGMS)[22,23] and (2) Open Gradient Magnetic Separation (OGMS)[20,24,25]. In either case, the cells are suspended in a solution. For HGMS a high magnetic gradient is utilized to extract the magnetically tagged cells onto a stationary surface (e.g. test-tube wall, steel wool mesh) from either a stagnant or a flowing solution. Since the HGMS is operated under entrapment mode, the separation is carried out in two steps. First, the cells are trapped on a surface and then, the magnetic field is removed to recover the cells. OGMS, on the other hand, operates in 'flow through' mode. A moderate gradient is utilized to deflect the cells from the flowing solution into separate collection streams. OGMS can be operated in a singe step and is suitable for continuous mode of cell separation. Choice of a magnetic sorter generally depends on the type of the applications. For example, if the objective is to collect a large amount of cells so that the cells can be utilized for in vitro culture or cell therapy applications, a continuous OGMS will be more suitable than a two step HGMS system. Alternatively, if the objective is to investigate a small sample for diagnostic purpose, HGMS systems may be preferable. The advantage of HGMS systems is that they can be as simple as having an external magnet and a test-tube. But, the limitation is that standard HGMS systems can only separate cells into magnetic and non-magnetic fractions. OGMS systems, on the other hand, are more complicated than the conventional HGMS systems. They need to be interfaced with peripheral systems such as

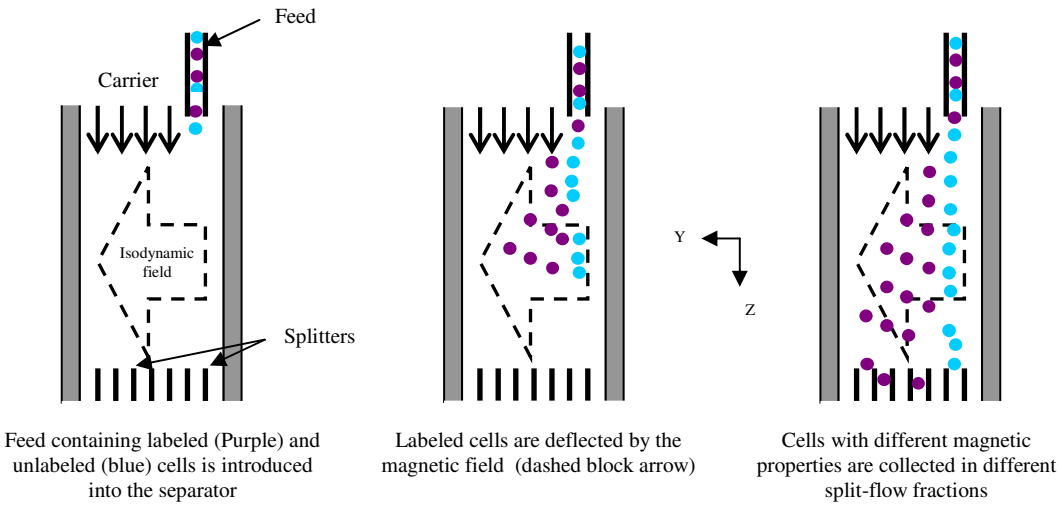

Figure 2.1-1: Schematic diagram showing the principle of an isodynamic open gradient magnetic cell sorter

pumps and collection systems. However, the advantages of OGMS systems are that they can separate cells into multiple fractions based on their magnetic susceptibilities[20,24-26].

The present work deals with the miniaturization of magnetic sorters and considers one type of sorter from each category. The long-term goal is to conjugate the two types of magnetic sorter and develop a high performance diagnostic device based on magnetic cell sorting. The OGMS and HGMS chosen for this application were an isodynamic OGMS and a bio-ferrograph, respectively.

2.1.1. Isodynamic OGMS

Isodynamic OGMS is the type of magnetic sorter where the separation is carried out under constant magnetic energy density gradient. The separation principle of an isodynamic OGMS is presented in Figure 2.1-1. A classic example of an isodynamic OGMS is the Frantz isodynamic OGMS[27]. In order to obtain the isodynamic magnetic field special designs of magnets are required[21]. Let us consider the isodynamic condition,

$$\nabla B^2 = \mathbf{const} \equiv \mathbf{A} \qquad (2)$$

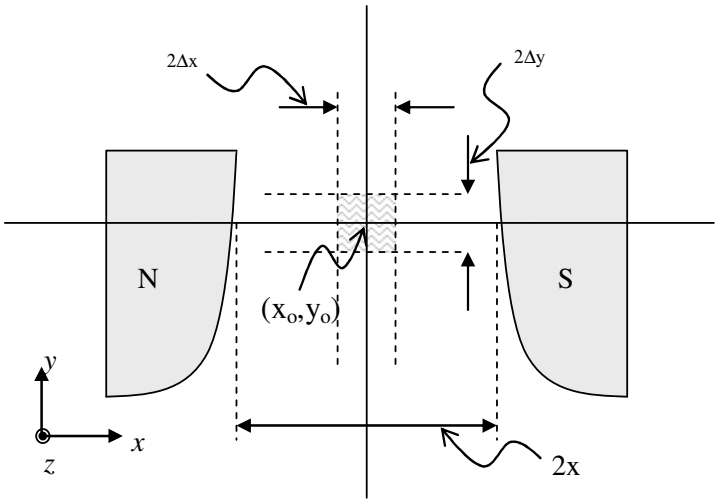

Figure 2.1-2: Schematic cross-section showing an example of magnetic circuit typically used in Open Gradient Magnetic Separation (OGMS)

where bold font is used to indicate vector quantities. A schematic cross-section diagram of an isodynamic OGMS is presented in Figure 2.1-2. If the direction of magnetic separation is intended to be along the *y*-axis while the flow is perpendicular to the *xy*-plane (*z*-axis in Figure 2.1-2), the desired condition in (2) can be rewritten as,

$$\frac{\partial B^2}{\partial y} = A \tag{3}$$

$$\frac{\partial B^2}{\partial x} = \frac{\partial B^2}{\partial z} = 0 \tag{4}$$

where italic font is used to indicate scalar quantities. Note that *A* denotes magnitude of the vector **A**. Integrating (3),

$$B^2 = Ay + C \tag{5}$$

Where, *C* is a constant of integration. Now, let us consider the region where the distance between the two surfaces is almost parallel to the center plane (Figure 2.1-2). Assuming that this distance is 2*x* and the magnetic scalar potential across the gap is *U,* according to the definition of the magnetic potential,

$$U = \int_{-x}^{x} H dl = 2xH \tag{6}$$

where, H is the magnetic field strength and can be defined in terms of B, the magnetic field intensity and μ, magnetic permeability as $\frac{B}{\mu}$.

So, from (6),

$$H = \frac{B}{\mu} = \frac{U}{2x} \tag{7}$$

Substituting (7) into (5),

$$\frac{U^2\mu^2}{4x^2} = Ay + C \tag{8}$$

The condition of the constant potential, $U(x,y)=U_o$ can be applied to the numerator on the left hand side of (8). As a result, (8) describes a hyperbolic function of y on x determining the shape of the equipotential lines, including the surface of the pole-pieces of the magnet. This means that constant magnetic energy density distribution can be obtained by using a magnet system consisting of two branches of non-confocal hyperbolic curves extended along the z-axis, acting as magnetic equipotential surfaces. Therefore most isodynamic OGMS devices are equipped with a magnetic system of hyperbolic pole faces[20,24,27]. An interesting discussion on the topic is included in Smolkin MR & Smolkin RD [28] .

The benefit of using constant magnetic energy density gradient is that magnetic particles of identical magnetization are subjected to comparable magnetic force. As a result, particles with different magnetization are deflected by different distances. Based on different deflected distances, multiple particles with different magnetic susceptibilities

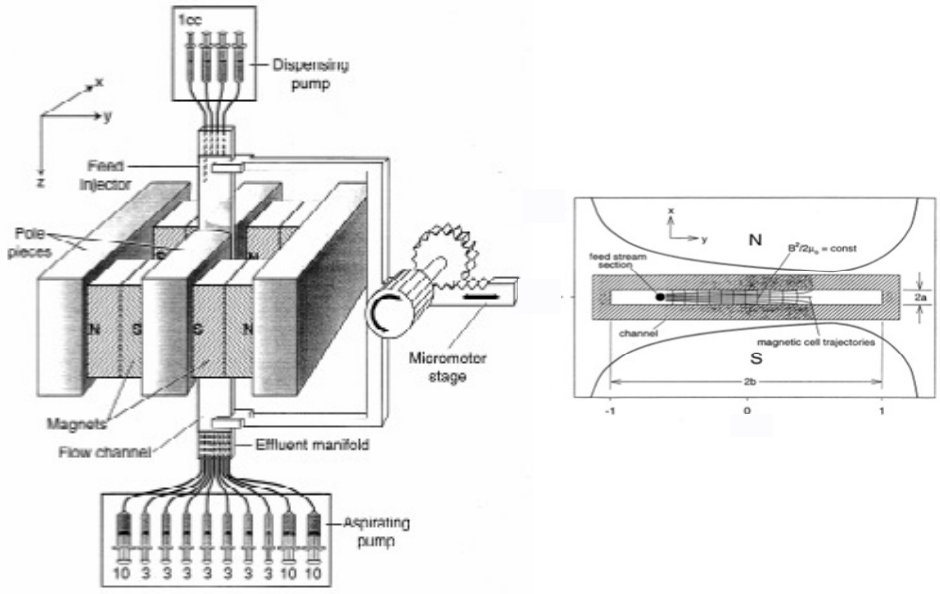

Figure 2.1-3: Schematic diagram of a conventional DMF system (adopted from reference 20)

can be separated in a single pass. Hwang et al. have shown that it is possible to separate three different particles with different magnetic susceptibilities in a single separation step from a mixture[24]. The Cell Separations Research Laboratory at the Cleveland Clinic developed a Dipole Magnetic Fractionator (DMF) that utilizes the same magnetic design to fractionate magnetically tagged cells into 8-10 different fractions[20,25]. Fractionation of cells is achieved using laminar flow of three fluid streams. One stream (feed) contains magnetically tagged cells while the other two (carriers) contain buffer solution. The feed stream is hydrodynamically focused into a desired location of the separation channel. Laminar flow condition allows these fluids to flow side by side with little or no mixing. When the fluid streams are passed through an isodynamic magnetic field, only the magnetically tagged cells experience the magnetic moment caused by the external field. As a result, the tagged cells move laterally to transport from the feed stream to the carrier stream. The total force imparted on the cell, which is a function of cell geometry and the

cells' magnetic dipole moment, determines the lateral distances that the tagged cells move into the carrier fluid. Thus, different types of cells, all immunomagnetically tagged, will move different distances and cell types can be identified by their lateral distribution. A schematic diagram of the DMF system[20] is presented in Figure 2.1-3. The DMF is composed of mainly a magnetic system with hyperbolic pole faces and a rectangular glass channel. The channel is placed between the poles of the magnetic circuit with the help of a translation stage. Inlet and outlet manifolds are used to introduce and withdraw feed and fractionate respectively.

2.1.2. Bio-ferrograph

The Ferrograph is an industrial instrument for wear analysis of mechanical equipment which operates in HGMS mode[29]. A strong permanent magnet is utilized to deposit magnetic entities from a flowing sample onto a designated location on a glass slide. The glass slide is then subjected to optical investigation for further analysis. Modified versions of the Ferrograph have been used for different biomedical applications[30-35]. The modified version, known as the Bio-ferrograph (Institute Guilfoyle, Belmont, MA) (has also been referred to as "thin film magnetophoresis"[36], "analytical magnetopheresis"[33], and "magnetic deposition microscopy"[30]). Bio-ferrographs (Figure 2.1-4, adapted from reference 32) employ a single magnetic deposition zone for deposition of cells/particles on a glass or polystyrene slide. The magnetic field is obtained from the inter-polar gap of a specially designed permanent magnetic circuit. The deposition slide is placed on top of the inter-polar gap such that the gap forms a magnetic barrier to the magnetically labeled cells. A flow channel is formed on top of the slide by placing a specially designed manifold on top. A spacer is placed between the slide and

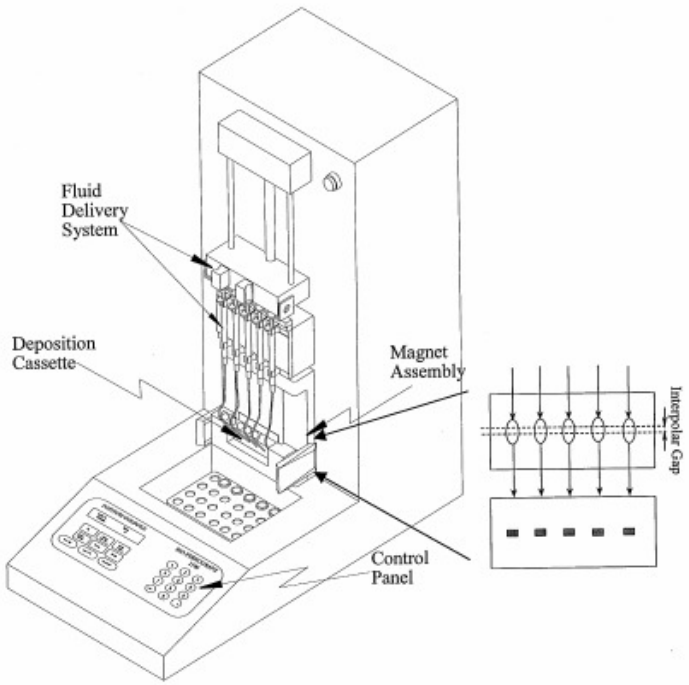

Figure 2.1-4: Schematic diagram of a conventional Bio-ferrograph (adopted from reference 32)

the manifold, which defines the channel. The manifold consists of inlet/outlet ports for establishing flow. This method has been utilized to detect breast cancer cells in peripheral blood[34], to count bacteria in ground water[32], malaria diagnosis[30], and to capture and separate polyethylene wear debris from hip simulator fluids[37].

2.2. Micro-Electro-Mechanical-Systems

The technology behind Micro-Electro-Mechanical Systems (MEMS) was initially derived from the Integrated Circuit (IC) manufacturing technology. It has the capability of devising functional components in the order of micrometer dimensions[38]. Relatively new, this technology involves adding and removing thin layers of different materials on silicon or glass substrates with processes such as thin-film deposition/removal, photolithography, selective etching, surface modification, bonding and electroplating of metals. Commercially successful devices and systems that use microfabrication and MEMS technologies include many microsensors (e.g., inertial sensors, pressure sensors,

magnetometers, chemical sensors, etc), microactuators (e.g., micromirrors, microrelays, microvalves, micropumps, etc), and microsystems (e.g., chemical analysis, sensor-feedback controlled actuators, etc). Moreover, batch fabrication and the capability of incorporating circuits make MEMS technology an attractive tool to realize miniaturized devices. Over the last fifteen years, numerous applications of MEMS technology have been considered[39]. One of the applications is the Lab-on-a-chip (LOC) technology that has become a growing research topic within the past few years with a potential to become a multibillion dollar industry[40]. The objective of a LOC device is to perform a complete biological or chemical analysis (e.g. separation, mixing, pumping, detection, etc.) on a single chip. A wide range of applications, including medical diagnostics, drug development and materials chemistry, are being considered for this technology. Separation of cells, which is the current topic of this thesis, has also been investigated using several approaches in a LOC platform[41].

A key benefit of MEMS devices is miniaturization. It can give portability to large-scale equipment and thereby can increase applicability of different technologies. However, a more important aspect of miniaturization is that some techniques just perform better at micro- and nano-scale. For example, laminar flow is a fluid mechanics phenomenon and to maintain true laminar flow conditions in a macro-scale device requires precise control and architecture. On the other hand, in MEMS based microfluidic devices the flow on the scale of the fluidic systems is so small that at any realistic fluid flow situation, the flow condition is always laminar[38]. This inherent laminar flow condition can be utilized with advantage for a number of different applications. It has been shown that multiple flow streams can flow side by side with only diffusion limited

mixing at the interface between the fluids up to several centimeters[42]. Such conditions have been used to transport and deposit cells in patterns determined by the laminar flow lines of the feed stream in microchannels[43], to precisely control flow of different fluids into the same channel (e.g. microfluidic valving[44]), and for hydrodynamic focusing of particles[45]. Additionally, microfluidic systems utilize reduced sample size, can provide increased surface to volume ratio, allow high throughput by parallel processing, and can reduce assay time[46].

The properties of microfluidic systems on a MEMS platform make it particularly attractive to the development of a miniaturized magnetic cell sorter. The ability of sustaining parallel flow of multiple fluids containing cells without significant mixing, precision structures on the order of microns and integration of magnetic components – all these capabilities will be very useful to develop miniaturized magnetic cell sorters.

2.3. State-of-the-art

There is significant motivation for developing miniaturized cell sorters. The ability to separate specific cells of interest from a biologically relevant sample can be very useful for different applications in the medical diagnostics industry, food processing industry, environmental monitoring and biological threat detection. High specificity (because of immunological selection) and very little or no effect on the carrier/medium and other non-magnetized cells make magnetic separations of cells a very suitable candidate for miniaturization. Other field-based particle manipulation techniques such as electric and acoustic fields have also been utilized to separate cells (e.g. free-flow cell electrophoresis, dielectrophoresis and ultrasonic focusing) based on the differences in electrical and physical properties of cells[47-49]. These techniques do not require any

immunological tagging as the separation is based on intrinsic properties of the cell. Nevertheless, the use of DC or AC current can interact with electrolytes present in the cell suspension solutions and generate destructive effects like electroosmotic flow and Joule heating and thereby, limit throughput and sensitivity of the method. Ultrasonic standing waves require a considerable difference in the physical properties (e.g. size) between cells to achieve satisfactory separation. Other methods such as immobilization on antibody-coated surfaces[50,51] or filtrations[50] are generally susceptible to clogging in the flow path, which can also be problematic for efficient cell sorting.

Fluorescence activated cell sorting (FACS) is another method of cell separation that is widely utilized for cell fractionation. In this method, cells are tagged with fluorescent labels and are analyzed using lasers one cell at a time. The cells are separated based on their fluorescent emissions[52]. FACS is used for both cell separation and cell analysis and it produces cell fractions with high purity and high recovery of target cells. However, FACS requires single files of cells and operates on "one cell at a time" mode, which results in low throughput. The high-powered lasers, which are essential for high quality results, are not suitable for miniaturization. Nevertheless, miniaturization of FACS using MEMS technologies has been attempted by several researchers[53-55], but they still deal with one cell at a time. These devices utilize optical sources that are much inferior to conventional high performance FACS and therefore are not as powerful as the original technology.

Several other techniques (e.g. PCR, microarrays) that utilize molecular techniques (e.g. polymerase chain reactions, hybridization) are quite popular for diagnostics. Obtaining purified samples by separation of cells is a prerequisite in their sample

preparation protocols. Microarrays have become well accepted for their ability to produce large amounts of data in a single experiment[56]. All these techniques require extensive sample preparation steps and are very sensitive to contaminations. In comparison to all other techniques, magnetic separation does not treat "one cell at a time"; does not interact with the medium/carrier; can be highly specific, gentle on the cells (due to laminar flow); could be a 'one step' separation process (providing high throughput, ease of automation and reduced labor cost) and hence, was chosen for miniaturization in this project.

MEMS for magnetic cell separations have been considered in the past[8,26,57-67]. At the Technical University of Denmark, a permanent square magnet was placed near the wall of microfabricated channels[58]. Immunomagnetic separation of cells tagged with magnetic beads was achieved in a continuous mode. More recently, this approach was further investigated to allow for separation of cells and particles based on their magnetic properties[26]. Work at the University of Cincinnati involved capturing target cells onto magnetic beads that had been treated with appropriate antigens, then, separating, and collecting the beads with target cells attached to the beads. An electrochemical immunoassay was also integrated with the separation step for the detection of cells[57]. Dipole magnets[62], an array of magnetic elements[60,63] or magnetized wire[66] has also been considered to separate cells from biological samples by other researchers. However, none of the previous work considered uniform magnetic field energy density distribution in the separation regime, which can allow a better control for separating multiple cells from a single sample. Very recently, a new approach is being formulated that utilizes a rotating/traveling magnetic field is utilized to separate magnetic beads based on their

size[61,64]. Although very innovative, the technology is still at an early development stage and requires a complicated algorithm to separate the particles.

2.4. Miniaturization – Outlook and Challenges

Miniaturizing magnetic cell sorters for a portable medical diagnostic system can have several benefits. For example, $CD4^+$ cell count is an important diagnosis for AIDS patients[1,3,7]. AIDS is in epidemic situation in the African third world countries and not everyone is receiving the proper medication and treatments due to lack of sufficient diagnostic information. The current standard practice is to establish a centralized location for providing diagnostic services. It is not always possible or feasible to bring samples to the centralized location for diagnosis. Currently, no handheld device is available that can give preliminary diagnosis for AIDS such as counting and monitoring $CD4^+$ cell population in a patient. Magnetic cell sorting can be an efficient way to monitor specific cells such as the $CD4^+$ cell count [68]. Thus, miniaturization of a magnetic cell sorter can be useful to obtain a portable device for this application. Instead of depending on a centralized location, the device can be brought to the bedside of the patients. Miniaturized devices will also require small sample volumes and less time to perform the tests. Rapid detection of pathogens can offer significant advantages over conventional culture procedures to provide early differential diagnosis.

Several diseases, if detected at an early stage, can be treated successfully before differential symptoms become apparent. In recent years, significant attention is devoted to detecting circulating cancer cells in blood as a method of detecting cancer at an early stage[2,4-6] The proposed system could find applications in detecting and monitoring disease stages of patients with cancers (e.g. breast cancer). The application of such a

device could also be extended for special circumstances like in the case of bioterrorism. Recent incidents have demonstrated that not only the warfronts but also common urban areas are at risk to deadly pathogens because of biological warfare proliferation, terrorist activities, or accidental contaminations. As a result, there is an increasing need for rapid and reliable detection of various pathogenic microorganisms. A compact portable system for detection of bio-warfare agents with high sensitivity and quantification capability can have enormous impact in dealing with such situations in both warfronts and urban areas.

Furthermore, since most molecular assays require cell separation as a sample preparation step, the proposed device could also be used in conjunction with other molecular diagnostics devices providing ease of automation and reducing processing time and cost. Lab-on-a-chip devices are an active area of research where a miniaturized cell separator can find valuable applications as a key sample preparative module. These devices can also find application in the food processing industry, drug manufacturing industry and environmental monitoring applications.

Research in MEMS and microfluidics shows great potential for developing miniaturized magnetic cell sorters. However, it is not necessary that the complete system is fabricated at the chip level. Initial cost of development for microfabricated devices is rather large, and therefore MEMS for miniaturization should only be considered when the technology can provide advantages that are not available with conventional fabrication techniques. One important section of magnetic separation is the magnetic field. The magnetic field can be obtained by using electromagnets [63,69] or permanent magnets [26,58]. A large magnetic field is desired to obtain high throughput – higher throughput can lead to shorter assay time. Strong permanent magnets such as NdFeB can generate a larger

magnetic gradient than the electromagnet. Moreover, the microfabrication of 3D complex electromagnets can be very complicated. As a result, electromagnets on the MEMS scale are usually not very strong. Microfabricated permanent magnets have also been investigated for magnetic MEMS application on different occasions [70]. In any case, a well-designed magnetic field is essential for the successful development of magnetic cell sorting. There are several examples in the literature where the magnet was not designed for the optimal use of the magnetic field [26,58]. One limitation with permanent magnets is that they are usually bulky and heavy components. However, since the working volume in a miniaturized system is reduced to sub-millimeter scale, the external magnet can also be designed sufficiently small to avoid bulky and heavy magnetic units. For this reason, the design of efficient magnetic circuits is an important aspect of miniaturizing magnetic cell sorters. These designs should also consider other practical situations with respect to the applicability of the device. For example, disposable cartridge-type applications are important in diagnostic devices to avoid cross contamination. The cartridge should also be designed such that it can be used with minimal professional training. The overall objective is to provide a tool that is not only effective, but also safe and easy to use.

Another aspect of developing MEMS based magnetic sorters is that MEMS is a relatively new technology. New microfabrication techniques are frequently being developed to achieve higher precision, minimize cost and enhance capabilities. There is always a significant cost and effort associated with the development of the first prototype for any MEMS based device. The initial development of the microfabrication processes can be grueling based on the type of development. Often times, new and improved techniques of fabrication are desired based on the specific applications and designs.

Finally, miniaturization leads to small sample sizes. Detection is an important part of the overall development and conventional detection techniques may not be sensitive enough to deal with sample sizes that are relevant to miniaturized devices. In that case, new and improved techniques will have to be developed to address these challenges.

While there are challenges associated with developing miniaturized systems for different applications, there are also significant benefits with miniaturization that is motivating a large scientific community to pursue novel and improved technologies to face these challenges. This thesis is another example of such efforts where new design, fabrication and detection mechanisms are addressed with the ultimate goal of developing miniaturized magnetic cell sorters.

Chapter III
Magnetic and Fluidic Design for the MEMS based Isodynamic OGMS

The current development was based on a macro-scale isodynamic OGMS system developed at the Cell Separations Research Laboratory, Cleveland Clinic, Cleveland, Ohio [20,25]. The macro-scale device is composed of a specially designed magnetic circuit (hyperbolicly shaped poles) and rectangular fluidic channel. Constant energy density gradient distribution is generally available in a certain volume within the air gap of the magnetic circuit[21]. The channel is aligned with the help of special alignment tools into the air gap of the magnet such that the magnetic energy density gradient is nearly constant inside the major portion of the channel. Nearly constant magnetic energy density gradient can provide a controlled magnetic environment where all the magnetic particles are subjected to the same magnetic gradient during their residence time in the channel. The complex shape of the magnetic poles and the need for precise alignment adds complexity, particularly when the device is to be used in a point-of-care setting. One could take the advantage of precision of MEMS to fabricate magnetic and fluidic components such that the alignment requirement is minimized. Moreover, OGMS devices require laminar flow

conditions, which is an inherent trait in MEMS based microfluidic devices[41,71]. The ability to fabricate flow splitters only a few tens of microns apart from each other at the end of the separation channel can also improve the resolution of separation significantly.

The objective of this chapter is to present a magnetic[72] and fluidic design of the miniaturized OGMS.

3.1. Magnetic Design

Since the hyperbolic shape is responsible for the nearly constant ∇B^2 distribution, embedding the hyperbolic portion of the circuit in the channel walls (Figure 3.1-1) may provide sufficient flexibility and eliminate the need for precise alignment. In this way, the embedded magnetic component would be aligned with the separation channel and integrated in a single chip. However, fabrication of a channel with embedded hyperbolic magnetic components on the walls is not easily amenable to MEMS fabrication process. MEMS devices rely on microfabrication techniques[38], which most easily can fabricate planar structures. We propose that the functionality of the hyperbolic pole shapes can be reproduced using a set of planar discrete rectangular pole-pieces. The planar design should allow compatibility with MEMS fabrication without compromising the desired magnetic field.

To design a magnetic circuit with planar discrete pole-pieces, we first consider the flow of a paramagnetic sample through the separation chamber. A schematic representation of the separation chamber is presented in Figure 3.1-2 (a). The flow is in the direction along *z*-axis and the magnetic force is acting in the direction along *y*-axis. Under the condition, the cells will move in the *y* direction.

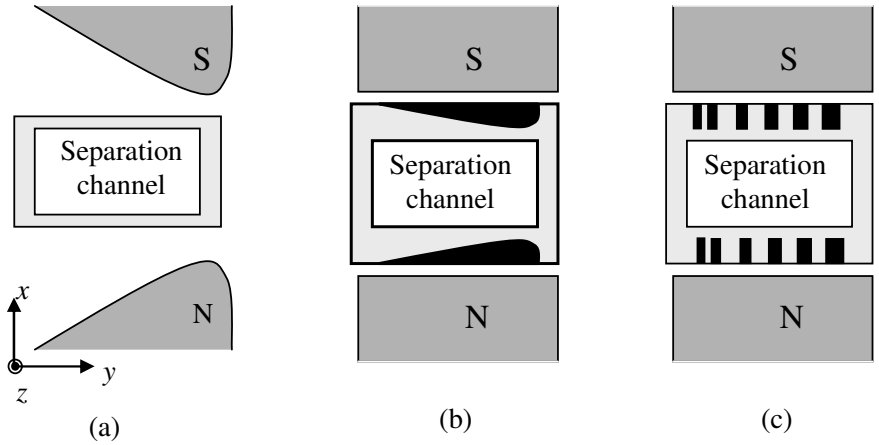

Figure 3.1-1: Schematic cross-section of (a) conventional hyperbolic magnet and separation channel arrangement; (b) Channels with embedded hyperbolic magnetic section on the wall; (c) Channels with embedded discrete pole-pieces

The $\left|\nabla B^2\right| = \frac{\partial B^2}{\partial y}$ distribution from a magnet with rectangular pole-pieces is schematically shown in Figure 3.1-2 (a) by the solid line. It is apparent that cells will be subjected to changing magnetic force as they travel along the *y*-axis if a rectangular magnet is used. The desired distribution of ∇B^2 along the *y*-axis is presented by the dashed lines – the traveling cells will experience a nearly constant magnetic force throughout their residence time.

The magnetic field was primarily investigated in 2D and at the mid-plane (*y*-axis) of the separation channel/external magnetic circuit ($\left.\frac{\partial B^2}{\partial y}\right|_{x=0}$). Models are developed in the graphic interface of MAGNETO 5.1 (Integrated Engineering Software, Manitoba, Canada) for 2D magnetostatic simulations. The material for the permanent magnet is chosen to be Neodymium-Iron-Boron and the ferromagnetic arms are assigned carbon steel. Materials with different saturation magnetization (B_s) ranging from 1.0T to 2.0T are used for the discrete pole-pieces.

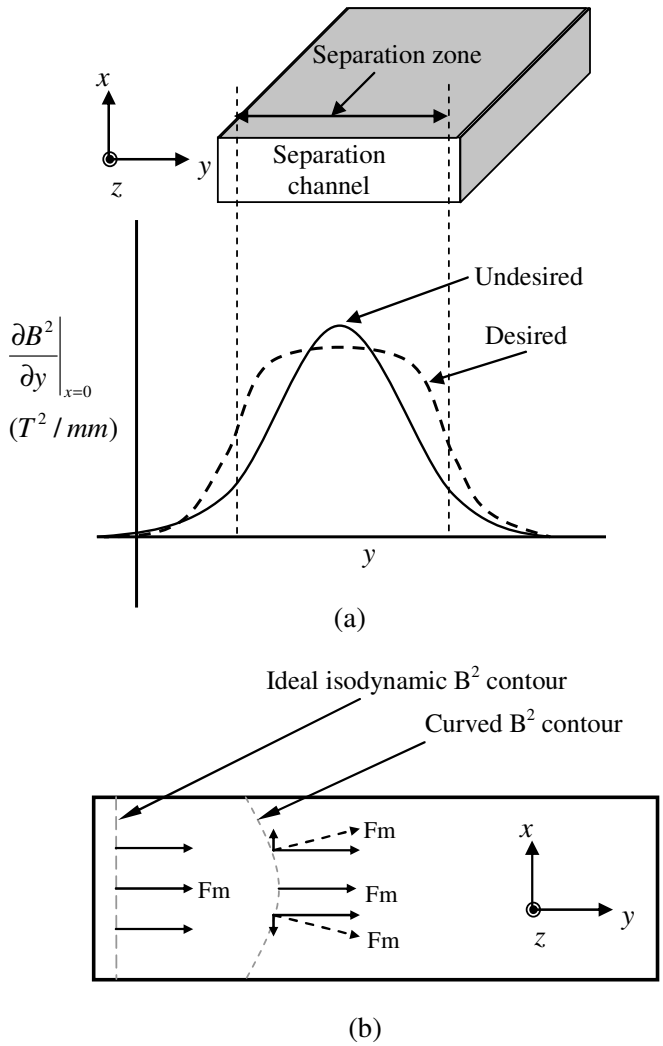

Figure 3.1-2: (a) Schematic diagram showing the desired and undesired $\left.\frac{\partial B^2}{\partial y}\right|_{x=0}$ distribution along the cross-section of the separation channel (b) Schematic diagram showing examples of B^2 contours (dashed lines) on a *xy-plane* of the flow-channel (The direction of flow is normal to the plane of cross-section).

The B-H curves of these magnetic materials are used to define magnetic properties of the materials used in the simulations. $\left.\frac{\partial B^2}{\partial y}\right|_{x=0}$ is analyzed for the model to check whether it is uniform over some distance along *y*-axis. The simulation is carried out using the boundary element method (~3,000 elements).

Although a nearly constant $\left.\frac{\partial B^2}{\partial y}\right|_{x=0}$ gives an initial indication of a satisfactory design, additional properties of the magnetic field are also investigated before reaching a final design. Due to symmetry, the value of $\frac{\partial B^2}{\partial x}$ is equal to zero at the plane of symmetry. However, away from the plane of symmetry $\frac{\partial B^2}{\partial x}$ will have a non-vanishing value that can influence the force profile on the cells. Therefore, away from the mid-plane the force acting on any cell will have two components due to $\frac{\partial B^2}{\partial y}$ and $\frac{\partial B^2}{\partial x}$. As a result, the cells will not be deflected strictly along *y*-axis, rather will follow the resultant of the two force components. If the contribution of $\frac{\partial B^2}{\partial x}$ is significant, the cells could be directed towards the top or bottom wall of the channel before satisfactory separation can be achieved. The situation is illustrated in Figure 3.1-2 (b) with the help of B^2 = const. contours on a channel cross-section. F_y and F_x are proportional to $\frac{\partial B^2}{\partial y}$ and $\frac{\partial B^2}{\partial x}$, respectively. If the $\frac{\partial B^2}{\partial y} >> \frac{\partial B^2}{\partial x}$ at different values of *x* along different *y* locations, it will be possible to obtain significant separation before the cells reach the top or bottom wall. For this reason, a satisfactory design with respect to nearly constant $\left.\frac{\partial B^2}{\partial y}\right|_{x=0}$ should be further investigated for the ratio of $\frac{\partial B^2}{\partial y}$ and $\frac{\partial B^2}{\partial x}$. In this work, such ratios are analyzed in terms of the angle, τ, where $\tau = \tan^{-1}\left(\frac{\frac{\partial B^2}{\partial x}}{\frac{\partial B^2}{\partial y}}\right)$.

Based on a satisfactory 2D analysis, a 3D model of the design is generated by extruding the 2D model to a desired depth in the graphic interfacing tool of AMPERES

5.2 (Integrated Engineering Software, Manitoba, Canada). Simulations were carried out on one symmetrical side of the 3D model about the *yz*-plane. Symmetry conditions are applied in the model on the *yz*-plane. The number of elements used for the model is ~7,000 and is solved using the boundary element method. Finally, the curves of $\left.\frac{\partial B^2}{\partial y}\right|_{x=0}$ at different points along *z*-axis of the 3D model are analyzed to investigate edge effects (along *z*-axis).

In summary, the criteria used for a satisfactory magnet design are as follows:

1. $\left.\frac{\partial B^2}{\partial y}\right|_{x=0}$ is nearly constant (within ±0.01 T^2/mm from a 2D analysis).

2. $\frac{\partial B^2}{\partial y} >> \frac{\partial B^2}{\partial x}$ at different values along *x*-axis for different *y*-positions ($\frac{\partial B^2}{\partial x}$ is less than 10% of $\frac{\partial B^2}{\partial y}$ from the 2D analysis).

3. $\left.\frac{\partial B^2}{\partial y}\right|_{x=0}$ is nearly constant at different values along *z*-axis (within ±0.01 T^2/mm from a 3D analysis).

The design that meets the abovementioned criteria is then investigated for different placement positions of the discrete pole-pieces inside the external magnet to determine the tolerance with respect to aligning the channel into the air gap of the magnet. For simplicity, only 2D analysis was performed on different placement positions.

3.1.1. Initial Design

To prove the concept that a constant energy density gradient can be obtained by using a combination of an external magnetic circuit and a set of discrete pole-pieces, a structure was developed in the graphic interface of the 2D magnetostatic simulation software (MAGNETO, Integrated Engineering Software Inc, Manitoba, Canada).

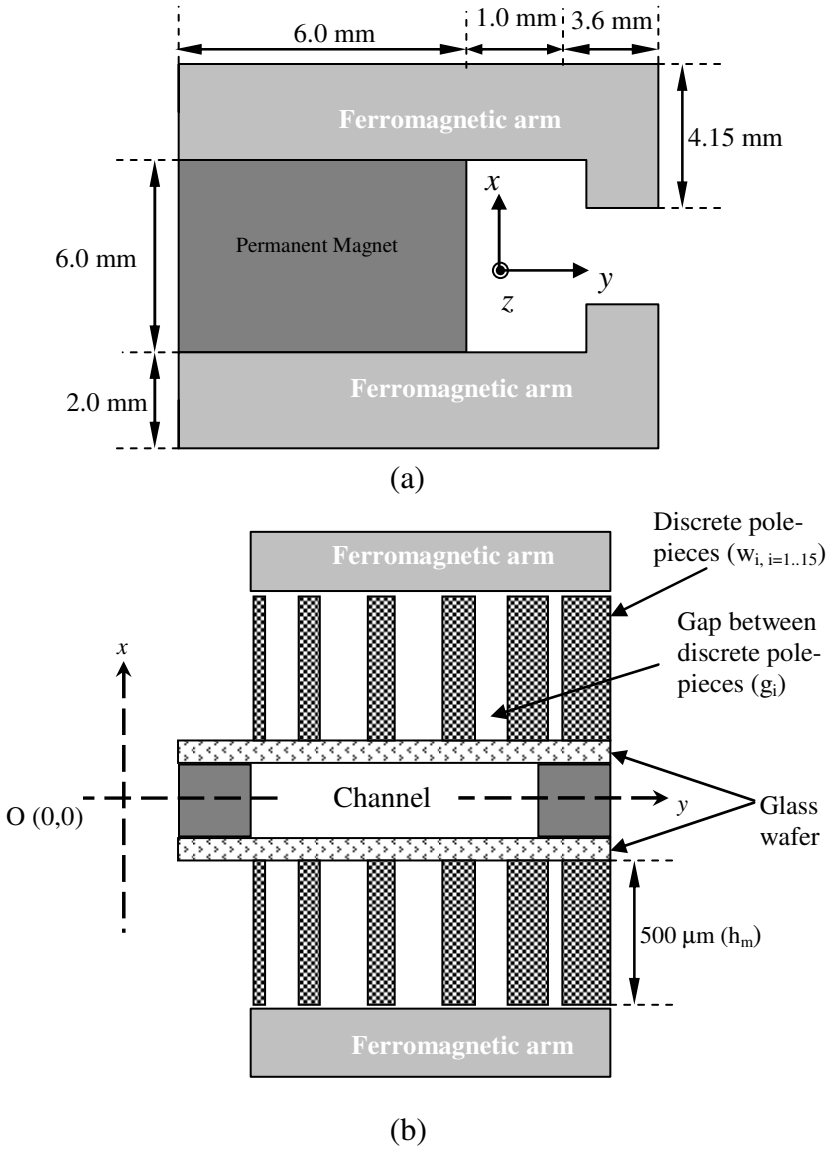

Figure 3.1-3: Schematic cross-section diagram (not to scale) (a) showing the external magnetic circuit for the initial design; (b) the biochip with embedded discrete pole-pieces for the initial design (The direction of the fluid flow is normal to the plane of the cross-section).

At this point for simplicity constraints that may arise from MEMS fabrication processes are not taken into account. Schematic diagram of the different components of the initial design is presented in Figure 3.1-3. The design is composed of two major sections:

1. An external magnet assembly with rectangular ferromagnetic "arms" to form a defined gap between the two pole-tips.

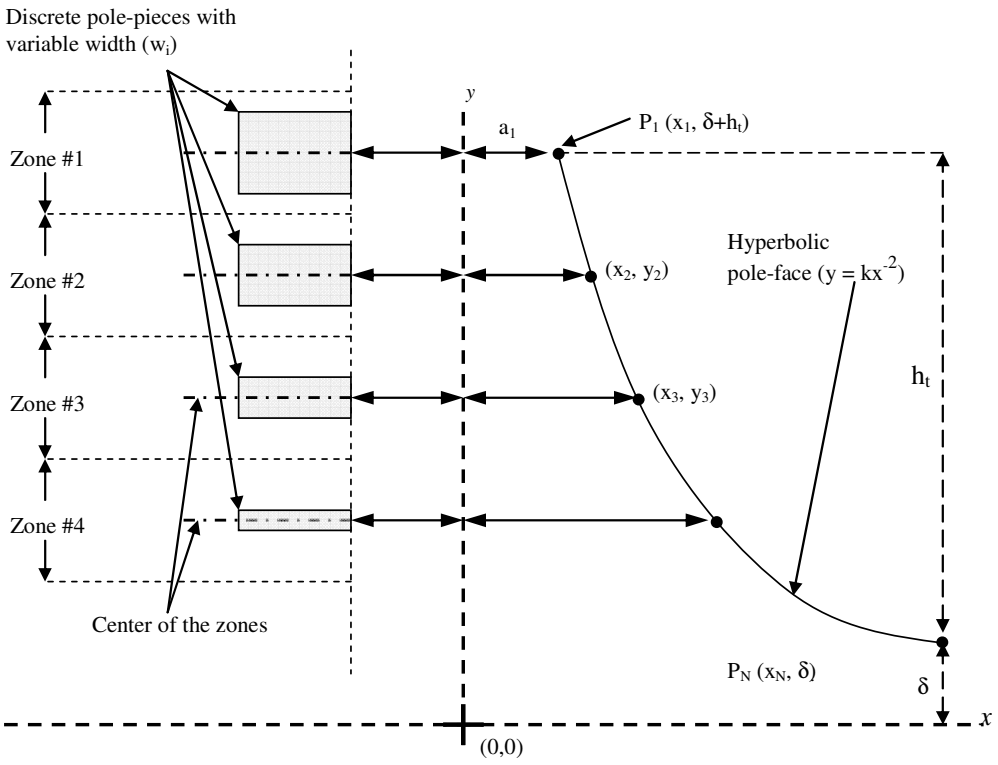

Figure 3.1-4: Graphics showing the discrete pole-pieces in relation to an equivalent hyperbola shaped pole face.

2. A set of discrete pole-pieces embedded on the side walls of a microfluidic chip (biochip) that can be positioned in the gap of the external circuit.

A set of 15 discrete pole-pieces (Figure 3.1-3 shows only six to represent the concept) was placed on both faces of the ferromagnetic arms. The distance between the set of pole-pieces was chosen to be 700 μm. This distance reflects the width of the flow channel plus the thickness of the walls. The pole-pieces were each 500 μm in height (h_m) with variable pole-piece widths (w_i) and variable inter-pole-piece gap widths (g_i) (Figure 3.1-3 (b)). Since hyperbolic pole-pieces have been shown to provide constant ∇B^2 over a substantial volume (Section 2.1.1), the widths of the discrete pole-pieces are determined such that they generate the same force on a paramagnetic particle on the plane of

symmetry (Figure 3.1-4). The following approach is used to determine the width of the pole-pieces.

Since hyperbolic pole shapes are responsible for the desired magnetic energy density gradient, we assumed that a hyperbolic function could be utilized to determine the size and gap width of the discrete pole-pieces. It was assumed that the sizeA hyperbolic function ($y = kx^{-n}$) is drawn in the first quadrant of a rectangular coordinate system and the variable pole-piece widths are found using the following expression.

$$\frac{w_i}{w_1} = \frac{x_1}{x_i} \qquad (10)$$

where, w_1 and w_i are the widths of the first (top) and the i-th pole-piece (i = 1 … 15) and x_1 and x_i are the distances from the center (x = 0) to the surface of the equivalent hyperbolic magnet, at the elevation of the pole-piece, for the first (top) and the i-th pole-piece (Figure 3.1-4). Each discrete pole-piece is placed at the center of a series of evenly spaced zones along the y-axis. Now, x_i can be evaluated from the hyperbolic function,

$$y_i = \frac{k}{x_i^{\,n}} \qquad (11)$$

To evaluate the constant k, two points P_N and P_1 lying on a hyperbola are chosen such that P_N had the coordinates (x_N, δ) and P_1 had coordinates (x_1, $h_t + \delta$). Substituting these into (11) gives,

$$h_t + \delta = \frac{k}{x_1^{\,n}} \qquad \delta = \frac{k}{x_N^{\,n}} \qquad (12)$$

From (12) the two unknowns k and δ are determined as

$$\delta = \frac{x_1^{\,n} h_t}{x_N^{\,n} - x_1^{\,n}} \qquad k = x_N^{\,n}\,\delta \qquad (13)$$

Table 3.1-1: Pole Piece and Gap dimensions for the initial design

Pole-piece #	w_i (mm)	g_i (mm)	h_m/w_i	h_m/g_i
1	0.225	0.034	2.22	14.55
2	0.198	0.038	2.52	13.07
3	0.174	0.064	2.88	7.82
4	0.15	0.088	3.32	5.58
5	0.129	0.110	3.88	4.53
6	0.109	0.131	4.59	3.81
7	0.091	0.150	5.51	3.33
8	0.074	0.168	6.74	2.98
9	0.059	0.183	8.43	2.73
10	0.046	0.197	10.84	2.53
11	0.035	0.210	14.47	2.38
12	0.025	0.220	20.28	2.27
13	0.016	0.229	30.43	2.18
14	0.01	0.237	50.66	2.11
15	0.005	0.243	100.60	2.06

The values of n, x_1, x_N, and h_t are properties of the hyperbola that have been chosen: $n = 2$; $x_1 = 0.35$ mm; $x_N = 480.0$ mm; and $h_t = 4.0$ mm.

Substituting k and δ into (11) and solving for x yields

$$x_i = \left(\frac{k}{y_i + \delta} \right)^{\frac{1}{n}} \tag{14}$$

Here y_i is the distance of a point on the hyperbola corresponding to the center lines of the evenly spaced zones (in this case, 0.25 mm wide zones) to the y-axis. w_1 is set to 225 μm and x_i is evaluated for zones 2 and onward - with the aid of (14) - and then substituted into (10) to find pole widths, w_i. The gap widths are found from the void space between the poles. The calculated results are listed in Table 3.1-1.

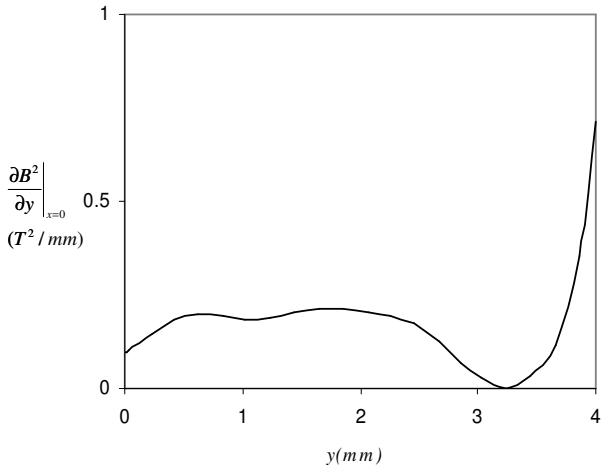

Figure 3.1-5: Graph showing 2D simulation of $\left.\frac{\partial B^2}{\partial y}\right|_{x=0}$ profile of the initial discrete pole-pieces design.

2D magnetic simulations found that constant $\left.\frac{\partial B^2}{\partial y}\right|_{x=0}$ of 0.2 ± 0.01 T^2/mm over ~2.0 mm along y-axis can be obtained (Figure 3.1-5). The preset tolerance of an acceptable value is ± 0.01 T^2/mm. This shows that it is possible to obtain uniform ∇B^2 distribution with a system of discrete pole-pieces. However, certain features of the design, such as 500 μm thick (h_m) discrete pole-pieces or structures with height to width aspect ratio as high as 100, are not readily suitable for MEMS fabrication process. Thick films are generally associated with high stress that can cause total device failure. In addition, the average $\left.\frac{\partial B^2}{\partial y}\right|_{x=0}$ value in the constant zone could be optimized to a higher value (~0.5 T^2/mm).

3.1.2. MEMS based model

Microfabrication involves selectively adding and removing thin layers of different materials on silicon or glass substrates. The described discrete pole-pieces can be fabricated using SU-8 plating molds and electroplating of suitable magnetic materials [73].

However, the thickness or the height to width aspect ratio of the discrete pole-pieces will be limited by processing restrictions of SU-8 and electroplating. For example, the complexity of fabricating SU-8 and electroplated structures increases with the increase in structure aspect ratio and thickness. Even fabricating pole-pieces with variable size and gap-widths can be more complex than pole-pieces that are equally spaced and are of equal size. The objective is to propose a design that would offer minimum difficulties with respect to microfabricating the biochip. Hence, as a general guideline for the biochip design, the following controls are followed:

(i) The height to width aspect ratio < 5.

(ii) The thickness of the discrete pole-pieces < 300 μm.

(iii) Equal size pole-pieces with equal gap widths.

The construction of the model also needs to be such that the biochip can be placed inside the air-gap of the external magnetic circuit i.e. the air-gap should be larger than the total thickness of the biochip. The total thickness of the biochip depends on its construction. The chip can be made with two 400 μm thick glass wafers bonded together with 250 μm high channels in between the wafers. The channel thickness was set to 250 μm based on fluidic design considerations, which will be discussed in Section 3.2 The discrete pole-pieces are placed on the exterior of the glass wafers, the maximum height of which is allowed to be 300 μm. Consequently, the maximum total thickness of the biochip is 1,650 μm. Therefore, the gap between the ferromagnetic arms is chosen to be 1,800 μm. A schematic cross-section of the final MEMS based device is presented in Figure 3.1-6.

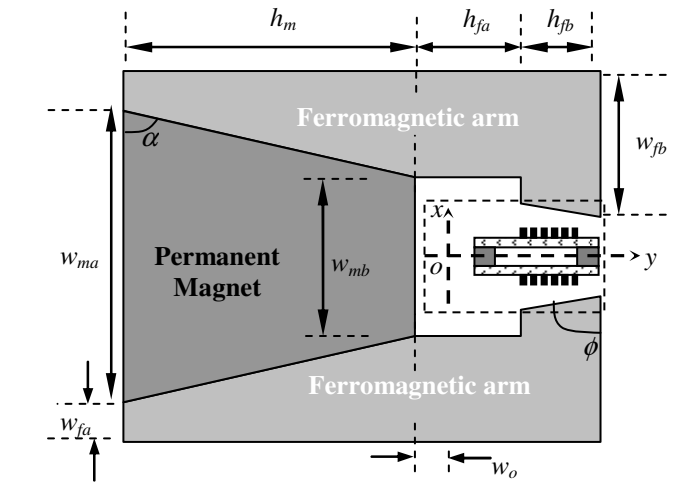

(a)

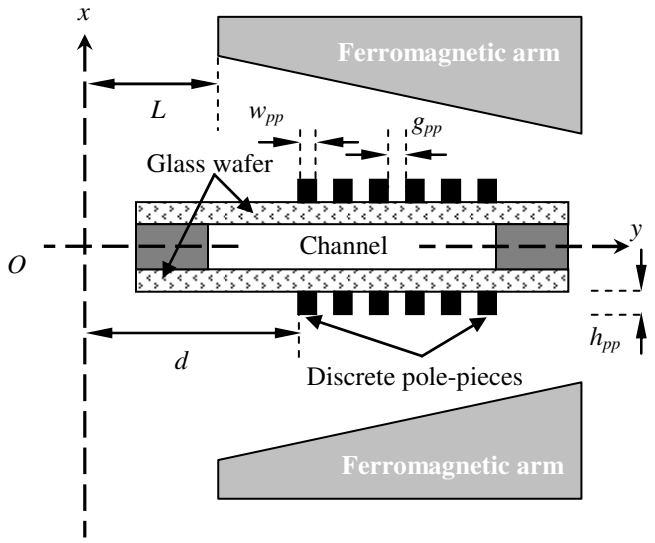

(b)

Figure 3.1-6: Schematic cross-section diagram (not to scale) showing (a) the external magnetic circuit for the final design; (b) the biochip with embedded discrete pole-pieces for the final design (The direction of the fluid flow is normal to the plane of the cross-section).

The size and shape of the permanent magnet and the ferromagnetic arm can be changed to obtain a stronger magnetic field. An iterative approach is undertaken to change the size (w_{pp}, h_{pp}), gap (g_{pp}) and position (d) of the sets of discrete pole-pieces from the initial design to fit the MEMS fabrication restrictions. The gap-widths between pole-pieces ranged from 100-200 μm and the width of the pole-pieces ranged from 50-

Table 3.1-2: Dimensions of the final design

Nomenclature[a]	*Dimensions*
w_{ma}	18.0 mm
w_{mb}	6.0 mm
w_{fa}	1.0 mm
w_{fa}	9.1 mm
w_o	0.5 mm
h_m	20.5 mm
h_{fa}	2.5 mm
h_{fb}	2.0 mm
L	2.0 mm
α	73.68°
ϕ	74°
d	2.0 mm
g_{pp}	185 μm
w_{pp}	75 μm
h_{pp}	100 μm

Nomenclature is explained in Figure 3.1-6

200 μm. The top corner angle (ϕ, Figure 3.1-6) of the ferromagnetic arm in the external circuit is also varied between 90° to 70° as a part of the iterative approach. The geometric parameters are changed based on the preceding simulation results until a nearly constant $\left.\frac{\partial B^2}{\partial y}\right|_{x=0}$ (within a preset tolerance limit of ±0.01 T^2/mm) distribution is obtained.

3.1.3. Results and Discussion

The dimensions of a satisfactory design for MEMS based applications are presented in Table 3.1-2. The saturation magnetization (B_s) of the pole piece material and the thickness of the discrete pole-pieces are found to be important parameters in

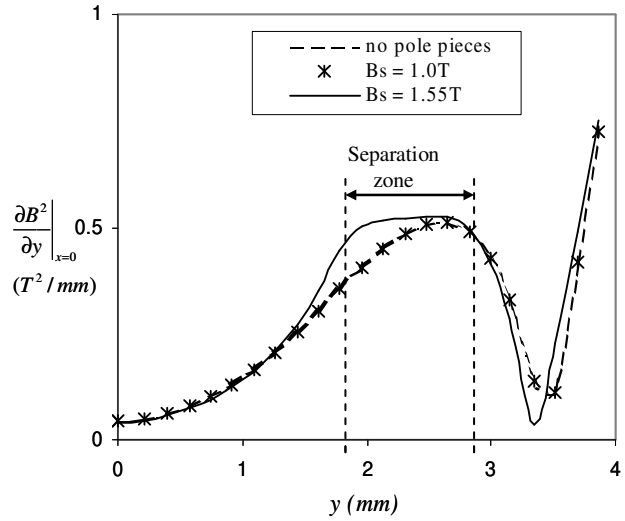

Figure 3.1-7: Graphs showing 2D simulation of $\left.\frac{\partial B^2}{\partial y}\right|_{x=0}$ profile of the final design with different pole-piece materials.

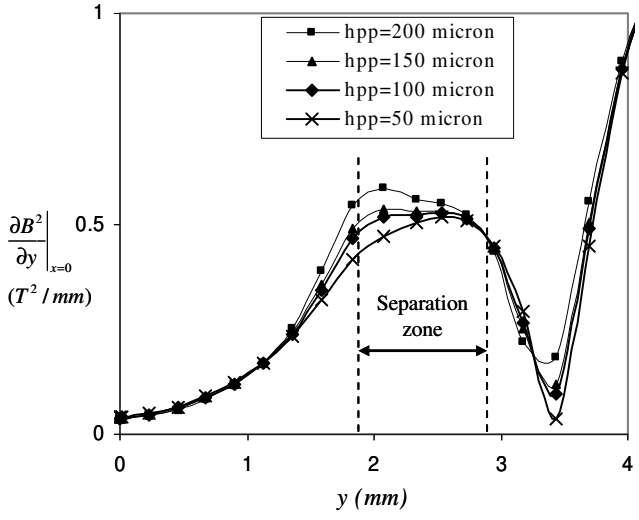

Figure 3.1-8: Graphs showing 2D simulation of $\left.\frac{\partial B^2}{\partial y}\right|_{x=0}$ profile of the final design with different pole-piece heights (h_{pp}).

generating the desired gradient of the magnetic field. From a microfabrication perspective, it is desired to design the pole-pieces with the minimum possible thickness (h_{pp}) and using electroplated materials such as Permalloy (Ni20Fe80), which are widely used for magnetic MEMS applications[74]. Figure 3.1-7 shows the effect of different saturation magnetization constants of the pole-pieces (h_{pp} = 100 μm) on the overall magnetic field gradient. It shows that discrete pole-pieces made of materials with $B_s \approx 1.0$T (e.g. Ni20Fe80) have the same profile as that of the design that has no pole-piece at all. On the other hand, materials with higher B_s (≈1.55T) were able to affect the overall $\left.\frac{\partial B^2}{\partial y}\right|_{x=0}$ profile and generate nearly constant distributions. Electroplated Ni-Fe alloys with higher Fe contents (>50%) has been shown to have B_s>1.55T [75] and would be suitable for this application.

Using materials of B_s = 1.55T, the thickness of the pole-pieces are varied and the resulting $\left.\frac{\partial B^2}{\partial y}\right|_{x=0}$ profiles are presented in Figure 3.1-8. It can be seen that a thickness of 100-150 μm is required to obtain the desired profile. All the simulations presented in this work beyond this point are based on 100 μm thick pole-pieces. Nearly constant $\left.\frac{\partial B^2}{\partial y}\right|_{x=0}$ of 0.51±0.01 T^2/mm is obtained with the final design over ~850 μm along the channel width (along y-axis).

The values of $\frac{\partial B^2}{\partial y}$ and $\frac{\partial B^2}{\partial x}$ are then evaluated at different points of the air gap cross-section to determine the area of the magnetic field throughout which the energy density distribution is nearly constant. This is done by picking a certain y location on the air gap

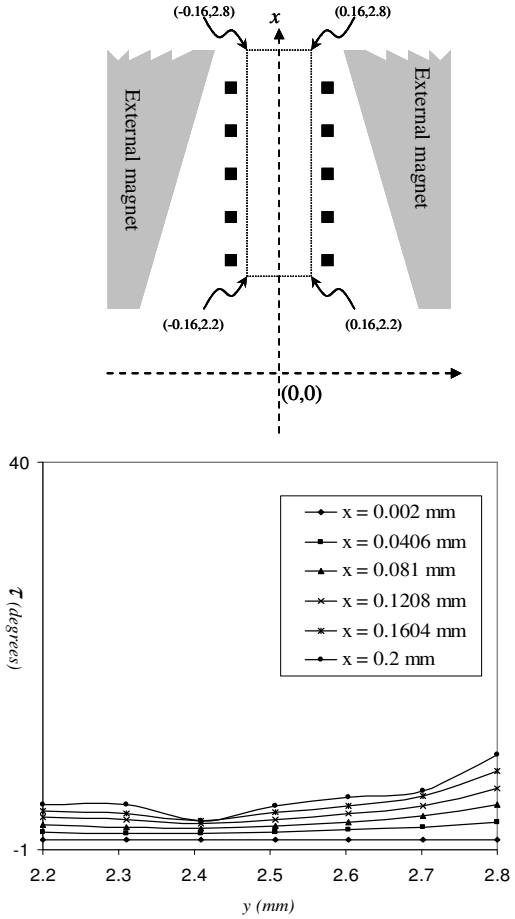

Figure 3.1-9: Graphs showing values of τ at different *y* location (range of *y* = 2.2 mm to 2.8 mm) for different *x* positions.

and evaluating $\frac{\partial B^2}{\partial y}$ and $\frac{\partial B^2}{\partial x}$ at different *x* locations corresponding to that *y*. Then another *y* location is chosen, to repeat the evaluation of $\frac{\partial B^2}{\partial y}$ and $\frac{\partial B^2}{\partial x}$. For a certain *y* location at each *x* position the value of τ (where, $\tau = \tan^{-1}\left(\frac{\frac{\partial B^2}{\partial x}}{\frac{\partial B^2}{\partial y}}\right)$) is then calculated. Figure 3.1-9 shows the τ value at different *y* location (range of *y* = 2.2 mm to 2.8 mm) for each *x* coordinate chosen for evaluation. The line of symmetry for the magnetic circuit passes through the center plane of the air gap, and therefore, only positive *x* values are shown in the graph. It can be seen that in the range of *x*= 0 - 0.1208 mm, the value of τ is less than 5 degrees for

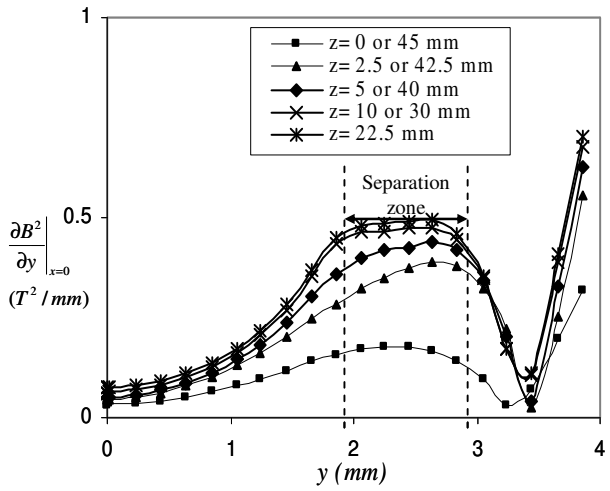

Figure 3.1-10: Graphs showing 3D simulation of $\left.\frac{\partial B^2}{\partial y}\right|_{x=0}$ profile of the final design.

different *y* positions (range 2.2 mm – 2.8 mm). This means $\frac{\partial B^2}{\partial x}$ is less than 10% of $\frac{\partial B^2}{\partial y}$ within a window covered by the above mentioned *x* and *y* ranges.

Next, the $\left.\frac{\partial B^2}{\partial y}\right|_{x=0}$ profile along different depths (*z*-axis) for a 45.0 mm deep magnetic module from a 3D simulation of the final design is evaluated (Figure 3.1-10). Magnetic flux loss near the edges along the depth of the magnet causes reduction in the magnitude of average $\left.\frac{\partial B^2}{\partial y}\right|_{x=0}$. Nevertheless, beyond 5.0 mm into the depth from the edges of the magnet the loss is negligible i.e. $\left.\frac{\partial B^2}{\partial y}(x, y, z)\right|_{x=0, y=2.2}$ varies only within ±0.01 T^2/mm for $0< z< 5$. This edge effect is not easily avoidable during magnetic cell separation. So, during the design of fluidic components of the cell separator, it is important to consider the edge effects. For example, for a 45.0 mm deep magnet the length of the separation channel should be 35.0 mm and needs to be placed inside the magnet where the magnetic field is not influenced by the edge effects. Additionally, the presence of discrete the pole-

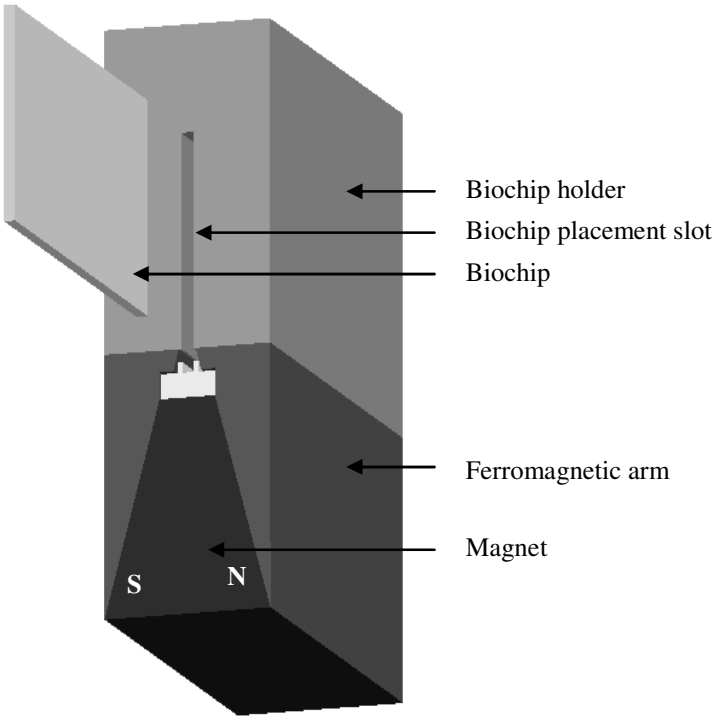

Figure 3.1-11: Schematic diagram of the proposed "slide-in" approach to insert the biochip into the magnetic field.

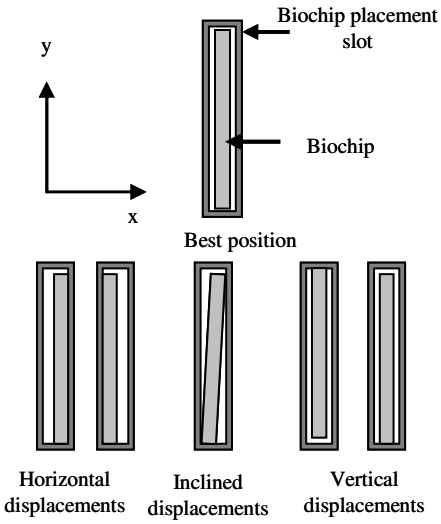

Figure 3.1-12: Schematic diagram showing different placement positions of the biochip inside the slot.

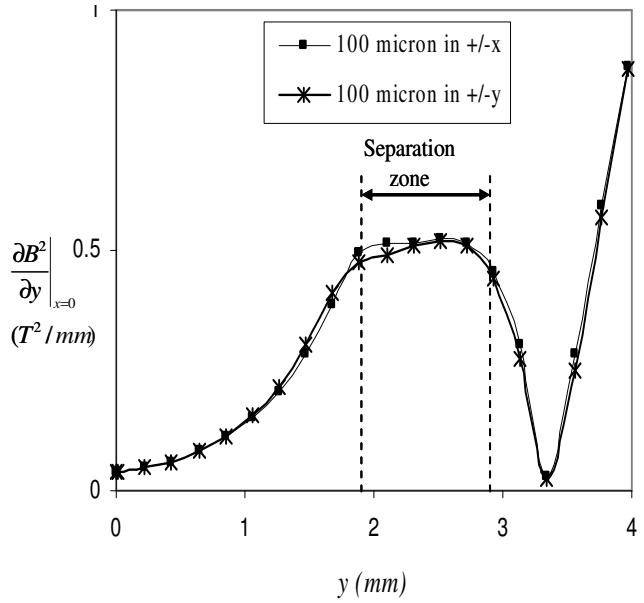

Figure 3.1-13: Graphs showing 2D simulation of $\frac{\partial B^2}{\partial y}\Big|_{x=0}$ profile with different horizontal (mid-plane of the biochip is placed ± 0.1 mm from the mid-plane of the magnetic circuit) and vertical displacements (*d* = 1.9 or 2.1 mm).

pieces also increase the magnitude of average $\frac{\partial B^2}{\partial y}\Big|_{x=0}$ by ~15% from the maximum that can be obtained without any discrete pole-pieces.

The final consideration for the design is to investigate the alignment tolerance of the biochip into the external magnetic field. It is desired to construct a slot into which one can "slide in" (Figure 3.1-11) the biochip without the requirement of any alignment tool. However, a "slide in" approach may result in different positions of the biochip with respect to the external magnetic circuit. Figure 3.1-12 shows different possible positions of the biochip in the slot. The effect of such misalignments is investigated using 2D simulations. It is found that misaligning the discrete pole-pieces ±100μm from the mid-plane (relative to *d)* does not change $\frac{\partial B^2}{\partial y}\Big|_{x=0}$ distribution significantly (Figure 3.1-13).

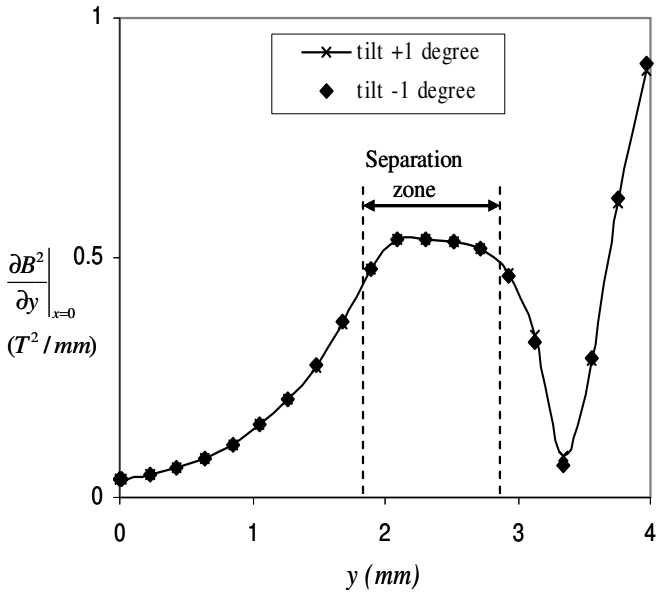

Figure 3.1-14: Graphs showing 2D simulation of $\frac{\partial B^2}{\partial y}\Big|_{x=0}$ profile with different inclined positions

Furthermore, if the set of discrete pole-pieces is rotated $\pm 1^{o}$ with the mid-plane, the uniformity of $\frac{\partial B^2}{\partial y}\Big|_{x=0}$ is maintained well within the preset tolerance (Figure 3.1-14). This analysis shows that the proposed design is well suited for adapting a "slide-in/out" cartridge installation.

3.2. Fluidic design

3.2.1. Channel layout

The channel section of the miniaturized OGMS was designed based on the layout of the macro-scale isodynamic OGMS. The channel consisted of three inlets and six outlets. A layout of the separation channel is presented in Figure 3.2-1.

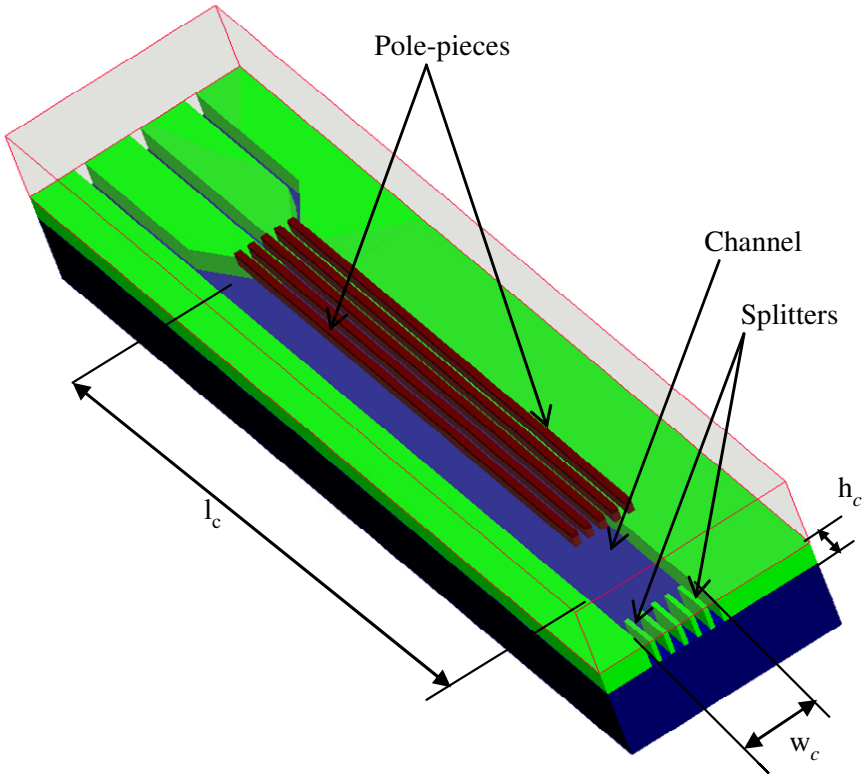

Figure 3.2-1: Schematic diagram showing the isometric view and the layout of the miniaturized OGMS channel

3.2.2. Channel thickness

The thickness of the channel was adjusted to the type of microfluidic interconnections. In most cases, interconnections to the microchannels are achieved by drilling suitable holes on the top or bottom of the device large enough to fit

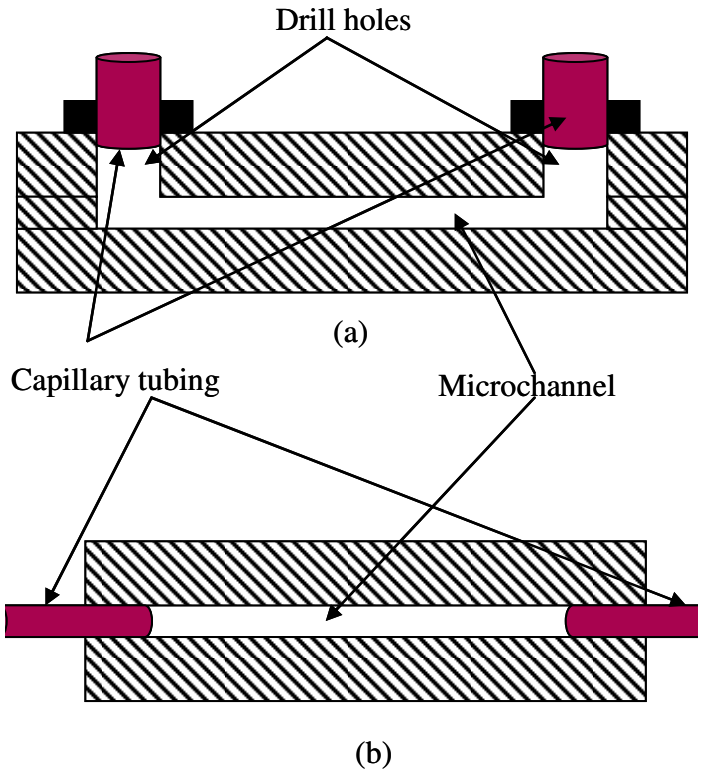

Figure 3.2-2: Schematic cross-section diagram showing microfluidic interconnections: (a) conventional interconnections where the capillary is inserted using drilled wholes on the cap/base wafer; (b) proposed interconnection scheme where the capillaries are inserted from the side opening which results from the premeditated design and wafer dicing

commercially available capillaries or tubing[76]. Connections made in this manner are generally cumbersome and often result in dead volumes in the flow system. An alternate approach to microfluidic connection was developed that did not require any drill holes. Instead of making the connection orthogonally from the top/bottom of the device, the connections were made from the side (Figure 3.2.2). Inlet and outlet connections were established using capillary tubing (MicroFil™, WPI Inc, Sarasota, Florida). The thickness of the channel was designed according to the outer diameter of the capillary tubes - the outer diameter of the capillaries should be slightly smaller than the thickness of the channels so that they can be inserted into the inlet/outlet ports at the both ends of the channel. In this case, the channel thickness was set to 250 μm based on the anticipated use of 31 gauge MicroFil™ capillaries (outer diameter of 234 μm).

3.2.3. Length of the channel

The separation principle is based on the trajectory of the cells under the applied magnetic field through the channel. The trajectory of a magnetically tagged cell under an external magnetic field depends on cell characteristics such as volume, mass, and fluid velocity, as well as the number and susceptibility of the attached labels. Assuming that the magnetic force acts only along *y*-axis when the flow is in the direction of *z*- axis and the magnetic particles stay only in the mid-plane of the channel cross-section, the velocity components acting on the cells will be,

$$v_m = \frac{dy}{dt} \qquad (15)$$

$$v_f = \frac{dz}{dt} \qquad (16)$$

Where, v_m= velocity component due to magnetic field

v_f = velocity component due to fluid flow

dividing Equation (15) with Equation (16),

$$\frac{dy}{dz} = \frac{v_m}{v_f} \qquad (17)$$

Now, v_m can be defined in terms of the magnetophoretic mobility (m) and the magnetostatic field energy density gradient ($\frac{\left|\nabla B^2\right|}{2\mu_0}$) as[77],

$$v_m = m\frac{\left|\nabla B^2\right|}{2\mu_0} \qquad (18)$$

where as, v_f is equal to the maximum velocity of the fluid (v_{max}). v_{max} can be defined in terms of known quantities of the flow system such as the volumetric flow rate (Q), the the height (h_c) and the width (w_c) of the channel, and the constant n,

$$v_{\max} = \frac{3(n+1)}{2n}\frac{Q}{h_c w_c} \qquad (19)$$

where,

$$\frac{3(n+1)}{2n} = \frac{v_{\max}}{v_{mean}} \qquad (20)$$

and, n can be calculated from the following relationship [20],

$$n(n+1) = 2\left(\frac{w_c}{h_c}\right)^2 \qquad (21)$$

Now, if we assume that the magnetophoretic mobility of magnetized cells are uniform and the magnetic energy density gradient is constant throughout the cross-section of the channel, integrating equation (17),

$$v_{\max}\int_0^d dy = m\frac{\left|\nabla B^2\right|}{2\mu_0}\int_0^l dz \qquad (22)$$

where, d is the distance traveled by the cells along y and l is the length of the separation zone where constant magnetic force is acting on the cells. Combining Equation (22) and (19)

$$d = \frac{mlh_c w_c \dfrac{\left|\nabla B^2\right|}{2\mu_0}}{Q\dfrac{3(n+1)}{2n}} \qquad (23)$$

Equation (23) can used to estimate the length of the separation channel based on known or desired values of all the parameters. For example, Jurkat cells can be utilized as a

model cell system for performing magnetic cell separation experiments. The average magnetophoretic mobility of labeled Jurkat cells is 5.25×10^{-4} mm^3/TAs. The width of the channel can be determined from the magnetic design. It should approximate the width of the region where uniform magnetic energy density distribution is available. In this case, w_c can be set to 1.9 mm. The thickness of the channel was set to 0.25 mm based on the design criteria. Flow rate can be set to 50 µl/min based on desired throughput. If the desired lateral movement is set to ~1 mm, the length of the channel can be calculated from Equation (10), (21) and (23) and was found to be ~31 mm. Based on the desired separation characteristics and throughput, the channel could be designed to any length. However, the length of the channel was limited based on the process capabilities in the MEMS fabrication steps. The available equipments for the MEMS fabrication processes were compatible with processing 4" wafers. Since, the idea was to use these available facilities and make the channels using microfabrication techniques; it was found that ~35 mm channels would be best suited with the current development process.

3.3. Conclusions

Magnetic and fluidic design aspects for the development of the isodynamic OGMS are presented. It is shown that a nearly constant magnetic energy density gradient can be obtained using a combination of a specially designed external magnet and a set of discrete pole-pieces. The discrete pole-pieces are integrated in the walls of the microfluidic channels (biochip), which is placed inside the air gap of the external magnetic circuit. The biochip was designed with planar structures that made it suitable for fabrication using microfabrication technology. The design is also suitable for slide in/out approach for placing the biochip inside the external magnet without using any

precision alignment tool. Fluidic design of biochip was performed based on practical considerations such as the anticipated microfluidic interconnection scheme and magnetic energy density gradient. Although significant attention to compatibility with the microfabrication processes was given during the design process, the final design still posed certain limitations. These fabrication challenges will be identified and discussed in Chapter IV.

Chapter IV
Microfabrication of the Isodynamic OGMS – Strategy and Challenges

4.1. Introduction

Microfabrication is an enabling technology – techniques that allow the fabrication of micro and nano scale components with high precision and reproducibility. It is essentially a method of adding and removing layers of different materials on a substrate. It involves a number of techniques such as spin coating, vapor deposition, sputtering, photolithography, solvent developing, etching, bonding and electroplating. Most of these techniques have been adapted from the microelectronics sectors and therefore, commercial production of MEMS devices can benefit from already available manufacturing infrastructure. Increasing interests in microfabrication and miniaturizations have been driving the development of a variety of applications including the successful commercialization of MEMS based accelerometers in the auto industry, micro-nozzles for inkjet printing and micro-mirrors for electronic displays[39,78]. Additionally, there is a large scientific community that is involved in improving the

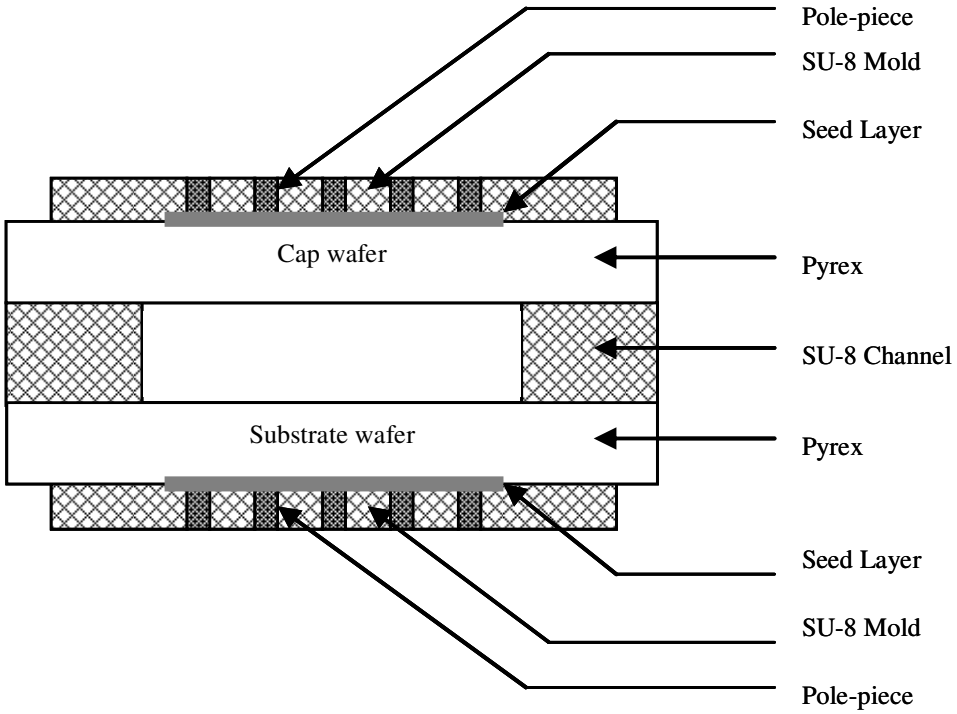

Figure 4.1-1: Schematic diagram showing the cross-section of the proposed isodynamic OGMS

capabilities of MEMS from both a fabrication and an application perspective. Ongoing developments include applications in the area of chemical and biological analysis (Lab on a chip[79]), clinical applications (Implantable MEMS[80,81]), optical devices[82], RF MEMS[83] and even micro combustion systems[84].

Our objective of utilizing MEMS technology has already been discussed in the earlier sections. The objective of this section is to address the proposed magnetic and fluidic design from a microfabrication perspective. Figure 4.1-1 shows a cross-section of the proposed microfabricated component (Biochip). It consists of an enclosed microchannel network and a set of discrete elements on both sides of the walls. From a fabrication point of view, it will be essentially a microdevice consisting of nine levels of materials –

Level 1: Substrate Pyrex wafer.

Level 2: Open microchannel

Level 3: Cap Pyrex wafer to for the enclosed microchannels

Level 4: Plating Seed layer on the Substrate

Level 5: Plating Seed layer on Cap

Level 6: Plating Mold on the Substrate

Level 7: Plating Mold on the Cap

Level 8: Discrete Pole-pieces on the Substrate

Level 9: Discrete Pole-pieces on the Cap

The development of the microfabrication process for a nine level microdevice can be very complex for any MEMS development process. Following any design work, the first step of a MEMS fabrication process is to choose the suitable materials and then formulate a fabrication strategy that would allow the successful development of the device. The next step is to design masks (e.g. L-Edit) based on the design and the fabrication strategy. The masks are used to define patterns of structures on the substrates via photolithography. Finally, the fabrication strategy is executed in a clean room environment to obtain the actual device. To summarize, the development of any MEMS device (post design) the following steps are necessary:

- Materials Selection
- Fabrication strategy development
- Mask development
- Microfabrication process development

4.2. Materials Selection

4.2.1. The Substrates

The magnetic design was performed based on a substrate thickness of 400 μm. Since,

there will be structures on both sides of the substrates, a double side polished substrate is essential. Single crystal silicon wafers, Pyrex wafers and quartz wafers are common substrates in MEMS. However, silicon substrates are not transparent and therefore, would not be suitable for this application. The proposed device was designed such that, cell separation could be analyzed by optical observations. As a result, it was important to select a substrate material that is optically transparent. Transparent Pyrex or quartz wafers would be more suitable for the current application. Therefore, 400 μm thick double side polished 4" Pyrex wafers were chosen to be the substrate material for this project.

4.2.2. Seed layers

A conductive metal layer is generally sputtered on the substrates to obtain the seed layer. The purpose of the seed layer is to allow electrical connections and flow of electrical currents. A very thin layer of a conductive metal such as Copper or Nickel is generally sputtered onto the substrate to obtain the seed layer. For this work, sputtered Chromium (~200 Å) and Nickel (~2000 Å) was chosen as the seed layer. The Chromium acts as the adhesion layer for the Nickel and Nickel acts as the conductive seed layer. Both Nickel and Chromium are CMOS compatible and are readily available for sputtering in a Class 100 clean room environment.

It is a simple process when the metal is sputtered throughout the substrate wafer. In this case, it was important that the substrate is transparent in selected locations so that the separation can be investigated via optical measures. As a result, a seed layer sputtered throughout the substrate was not feasible. Instead, the seed layer was 'patterned' such

that the metal layer is removed from selected areas on the chip to allow optical access into the device.

4.2.3. Microchannel

Based on the fluidic design of the proposed device, the thickness of the microchannels was determined to be 250 μm. Generally, microfabrication processes are involved with thin films that can range anywhere between a few nanometers to a few microns. Structures of 100-250 μm thickness are very thick for common microfabricated applications. However, there have been significant developments in thick and high aspect ratio structures[85,86]. Processes like LIGA[87], stereolithography[88,89] and deep RIE (Reactive ion etching)[90] have been developed to obtain thick and high aspect ratio structures for MEMS applications. Nevertheless, these processes require complex and sophisticated equipment that can be expensive, slow and of limited accessibility.

Soft-lithography with PDMS (Polydimethylsiloxane) is another common approach for fabricating microchannel structures for microfluidic applications[91,92]. These processes are comparatively inexpensive and suitable for rapid prototyping. PDMS is also nontoxic to cells, which makes it attractive for biological applications. However, PDMS is a flexible material and application of PDMS in microfluidics is often associated with rigid supporting substrates[93-97]. While complicated structures such as 3D multilevel microfluidic channel networks have been reported with PDMS[98], microchannels integrated with magnetic elements in PDMS (such as required for this project) is not common. In this project, design requirements such as the embedded discrete pole-pieces on both sides of the channel walls would preclude the development the biochip using soft materials such as PDMS. SU-8, an epoxy based thick photoresist, may be a preferable

alternative. Cured SU-8 is a hard, optically transparent, chemically resistant polymer that can be used for the fabrication of thick (up to few hundreds of microns) and high aspect ratio structures using common microfabrication tools[85,99-101]. SU-8 is capable of forming a thick film in a single coat and is curable through UV exposure. The material is available from MicroChem Corp, Newton, MA at different viscosities to aid the development of structures of different thicknesses. SU-8 has been utilized to obtain microfluidic channels[102-109], electroplating molds[110-113], micro-molds for replica molding[114-116], optical waveguides[102,117] and as other microstructures for MEMS based applications[118,119]. Even three dimensional structures have been obtained using multi-level SU-8 processing for different applications such as fabricating tissue engineering scaffolds[120] and complex microfluidics[121]. The flexibility in fabrication capabilities and properties such as chemical resistance and optical transparencies have made SU-8 a very desirable material in the field of microfluidics. Therefore, SU-8 was selected as the structural material for fabricating the microchannels.

4.2.4. Discrete pole-pieces

Electroplating is a technique of applying layers of metal or metal alloys on a substrate. It is a process frequently used in microfabrication technology to obtain functional metal structures such as micro-electrodes, magnetic elements and micro-coils[122-124]. The choice of material for the discrete pole-pieces was governed by the magnetic design. The design showed that the optimum thickness of the pole-pieces would have to be between 80-100 μm and the saturation magnetization of the material would have to be at least ~1.5 T. Nickel[74,125] and Permalloy[74,123,126,127] are the magnetic materials that are generally utilized in most magnetic MEMS devices. Neither of these

materials meets the saturation magnetization criterion defined by the magnetic design of the proposed device. Therefore, it was important to find a material that can be electroplated and have a saturation magnetization of at least ~1.5 T.

The development of electroplated high moment magnetic materials has been primarily driven by the electronic data storage industry[128,129]. Several electroplated materials such as CoFe alloy, CoNiFe alloy, High iron NiFe alloy and CuFeCo alloys have been shown have saturation magnetizations that are greater than 1.5 T. However, the thickness requirements in the data storage industry are generally on the order of only a few microns or less. Conversely, the thickness requirement of this application is in the order of 80-100 microns. Residual stress in thick electrodeposited materials can be an obstacle in utilizing the materials available from the electronic data storage industries, since stress generally increases with the increment in thickness[74]. Park et al reported the development of thick high moment magnetic materials such as Ni50Fe50 and CoFeCu for MEMS applications[130]. But the maximum thickness reported by this group was <20 μm.

The closest match for the desired magnetic material was found from a nanotechnology based company (Integran Technologies Inc.) from Ontario, Canada. They were using their proprietary pulse plating technology to develop electrodeposited nanocrystalline alloy of NiFe (Ni: 0-100%) with thicknesses up to 250 μm. For this reason, an alloy of electrodeposited 50% Ni and 50% Iron was chosen as the material for the discrete pole-pieces.

4.2.5. Electroplating molds

One important aspect of developing electroplated structures for microfabrication is the electroplating mold. The plating mold defines the area where the metals are

deposited. These molds can be made of different kinds of photoresist materials that are patterned on a substrate material coated with a conductive seed layer. Since the molds are a part of the electroplating process, it is important that the mold material can withstand the harsh environment of the plating solution. With respect to this particular application, the thickness of the mold was a determining factor in choosing an appropriate material. Not all photoresists available for electroplating are capable of forming 100 μm thick structures. However, SU-8 is capable of forming such thick electroplating molds and generally stable in common electroplating solutions[85]. Since, SU-8 is already being used as the material for fabricating the microchannels it would be convenient to use the same material for the electroplating molds.

4.3. Fabrication strategy

It is important to develop a strategy before the actual fabrication process is initiated – the sequence by which each of these levels can be fabricated. The sequence is determined based on different parameters such as the alignment requirements between the features on the different levels and the availability of the processing equipment. In this case, the strategy was to first lay down the 'patterned' seed layer (Level 4) on a 'transparent' substrate wafer (Level 1). 'Open' microchannels (Level 2) can then be fabricated on the other side of the wafer such that the channels are aligned with the patterned seed layer. Next, a second seed layer (Level 5) can be deposited and patterned on the transparent cap wafer (Level 3). The other side of the cap wafer can then be grossly aligned and brought

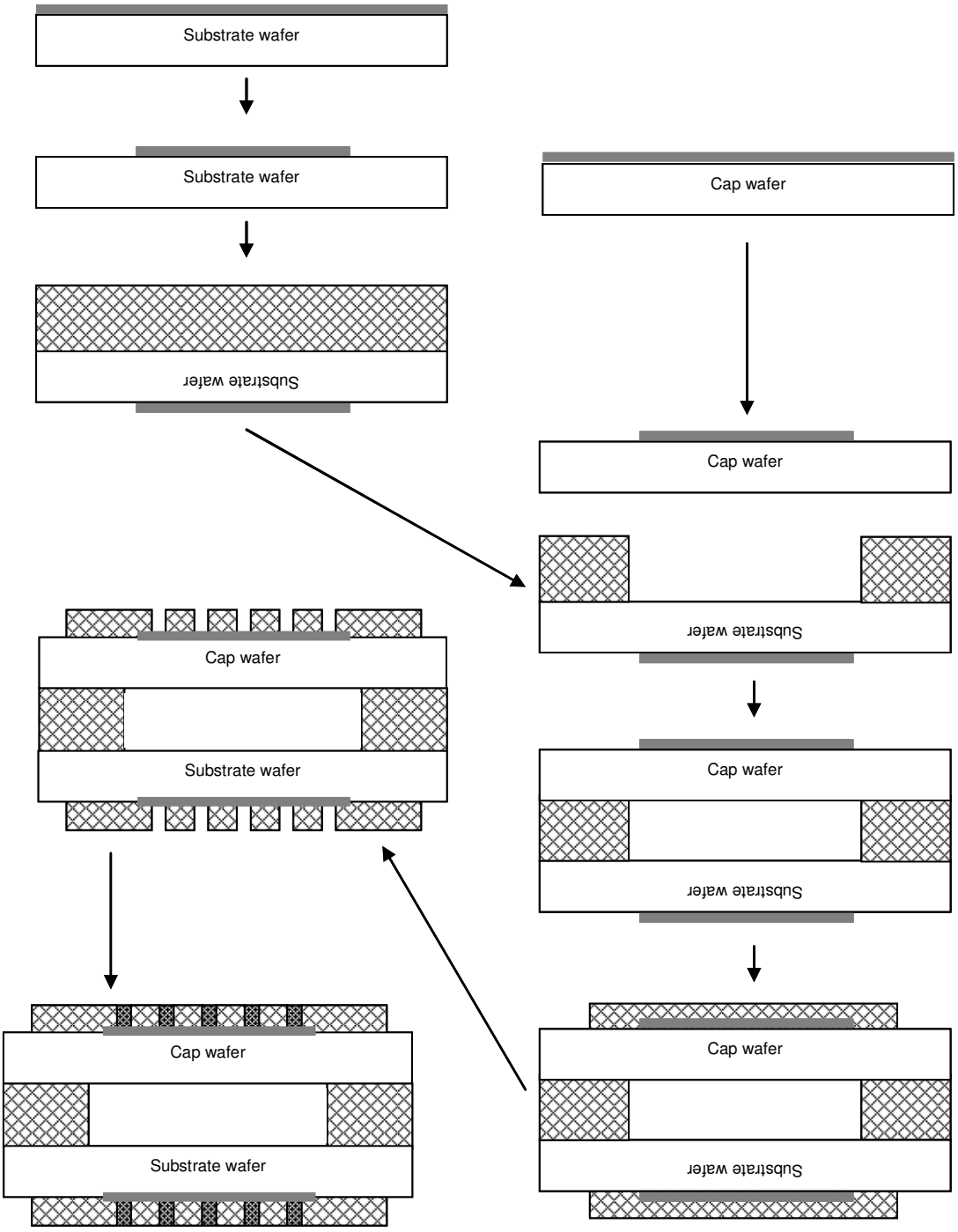

Figure 4.3-1: Schematic diagram showing fabrication strategy for the proposed isodynamic OGMS

into contact with the open microchannels. The wafer stack can then be bonded to obtain the enclosed microchannels. After bonding, plating molds (Level 6 and Level 7) of desired thickness can be placed on both sides of the bonded wafer. The molds should be patterned such that they are aligned with the underlying seed layers and with each other. Finally, discrete pole-pieces (Level 8 & Level 9) can be electroplated on areas defined by the plating molds to the desired thickness. The fabrication strategy is schematically presented in Figure 4.3-1.

4.4. Mask Development

Photolithographic masks are essentially glass plates with patterned metal films on one side. The masks are key components of any photolithographic process. Photoresist coated substrates are exposed through a mask using UV light to obtain the desired pattern on the substrate. Multiple masks may be needed to obtain multilayer devices. For example, based on the proposed fabrication strategy, 5 masks should be required:

Mask #1: To define the seed layer on the substrate wafer

Mask #2: To define the microchannel network on the substrate wafer

Mask #3: To define the seed layer on the cap wafer

Mask #4: To define the electroplating mold on the substrate wafer

Mask #5: To define the electroplating mold on the cap

Mask layouts were designed using commercial CAD software (L-Edit^{TM}, softMEMS, Los Gatos, CA). The layouts were based on the magnetic and fluidic designs. In addition to the device layout, alignment marks were placed so that each level can be sequentially aligned during the fabrication process. The mask layouts were sent to Photo Sciences Inc. (Torrance, CA) for fabrication. Initially, the process was developed using five masks.

However, based on the progress in the process development the masks had to be modified and new mask designs were required. Schematic diagrams of the masks are presented in Appendix A.

4.5. Microfabrication process development

The key structural materials involved in the development of the proposed device are Pyrex, Ni seed layer, SU-8 and Electroplated NiFe (Fe~50%) alloys. There are certain limitations with respect to processing these materials according to the fabrication strategy described in section 4.2. For example,

- Adhesion of SU-8 on metal and Pyrex is known to less than ideal[107,131,132]. There is also significant mismatch between the thermal expansion coefficient between cured SU-8 and common substrate materials such as silicon or glass[133]. As a result processing thick (100-250 μm) SU-8 film on Pyrex substrates or Ni seed layers can be a challenge.
- The formation of enclosed microchannels would require the development of a wafer bonding technique that is suitable for the current development. Since the microchannels will be made of SU-8, it is important to utilize a low temperature wafer bonding technique. The wafer bonding temperature should be similar to the processing temperature of SU-8. SU-8 itself can be utilized to obtain low temperature adhesive bonds[102,103,106,134-137]. However, the available SU-8 bonding techniques are generally sensitive to the thickness variation of the SU-8 film and are not suitable for large area integration. The proposed device is about 35 mm long and the layout of the device extends from one end of the wafer to the other end – only three devices can fit

into one 4" wafer. As a result, common SU-8 based bonding techniques may not be sufficient to obtain proper sealing throughout the channel.

- The proposed device is comprised of SU-8 structures on both sides of the wafer. Any process regarding the development of SU-8 films on both sides of a wafer has never been demonstrated.
- Finally, Integran Technologies developed their electrodeposited nanocrystalline NiFe for conventional plating applications. They have never demonstrated the ability to utilize the same material for MEMS and SU-8 applications.

4.6. Conclusions

Different aspects of the initialization of the microfabrication process development and the associated challenges have been discussed. In order to address these challenges, it was important that the different aspects of the overall fabrication process be addressed separately. The process development was therefore broken down into several components.

- Develop enclosed microchannels – In this part of the development, processes that could improve the adhesion of 250 μm thick SU-8 to Pyrex was addressed. A SU-8 based wafer bonding technique was also developed that is not very sensitive to the film thickness variation.
- Develop plating molds – Microfabrication processes to obtain the seed layers and the plating molds was addressed.
- Develop plated materials – Although Integran Technologies had demonstrated the ability to develop eletrodeposited thick alloys of Nickel and Iron, their applications had never been demonstrated for a microfabricated device. Therefore, the development

of the discrete pole-pieces in collaboration with Integran Technologies was also an essential step in obtaining the final Biochip.

- Develop microchannels integrated with plating molds – The ability to integrate the enclosed microchannels and the plating molds would require a process where SU-8 could be processed on both sides of the bonded wafers.

These individual processes will be addressed and discussed in details in Chapter V.

Chapter V
Microfabrication of the Isodynamic OGMS – Process Development

5.1. General processing steps for SU-8 materials

SU-8 (2000 series, Microchem, Newton, MA,USA) is an epoxy based negative photoresist[138]. It is a thick material that is available in different viscosities controlled by adjusting the amount of solvent (Cyclopentanone) in the formulation. It is generally coated onto substrate wafers using a conventional spinner. After coating, the solvent is evaporated by baking the coated wafer at a suitable temperature (generally at 65-95C). This step is known as the 'Soft-bake' or the 'Pre-bake' step. Following soft bake the film is exposed to UV light using a UV aligner. Masks are utilized at this step to selectively expose the film to define patterns on the film. Cross-linking is initiated with the UV excitation. The film is then baked (generally at 95C) to allow the further polymerization of the exposed region. This step is known as the 'Post Exposure Bake (PEB)'. During PEB the patterns become hardened. Next, the film is immersed in a developer solution (SU-8 developer, Microchem, Newton, MA, USA) to dissolve unexposed SU-8 and thus,

the desired structure are photolithographically fabricated. Following the 'development' step, the film may be further hardened by baking it at 95-120C (Hard bake). These are the generalized steps for processing SU-8. However, different parameters (e.g. Film thickness, Soft bake time, exposure dosage, PEB time, development time, etc) in all the steps have to be optimized to obtain a desired product. Once crosslinked, SU-8 is an optically transparent-plastic like material that is highly resistant to other chemicals.

5.2. Development of enclosed microchannels via wafer bonding

Wafer bonding is an important process in microfabrication[137,139]. From packaging sensors[140] to fabricating microfluidic channels[141], Micro-Electro-Mechanical-Systems (MEMS) have benefited significantly from the wafer bonding technology. One common method of wafer bonding is to utilize an intermediate layer of polymeric adhesives to form the bond. The advantages of using adhesives for wafer bonding are that it is simple, cost effective, suitable for bonding different types of materials, and carried out at comparatively low temperatures. Different kinds of polymers have been considered for adhesive wafer bonding[137], among which BCB (Benzocyclobutene) and SU-8 have been the most popular[103,135,136,142,143]. However, in a direct comparison study by Pan *et. al.*, SU-8 was found to be a better bonding agent than BCB in terms of bonding strength and processing parameters[144].

Microfluidics is the science of understanding and utilizing fluid flow at micro- and nano-scale. Enclosed micro- and nano-channels are fundamental to microfluidic devices. Formation of these channels is a critical step. It is relatively simple and inexpensive to fabricate 'open' microchannels using SU-8 compared to conventional approaches (e.g. deep RIE). While there have been a few reports on the SU-8 based fabrication of

enclosed microchannels without any bonding steps[108,109,145,146], wafer bonding has been the more prevalent choice[103,106,107,134-136,143,147]. The SU-8 based bonding process is generally associated with the formation of a thick structural layer and crosslinking that structural layer to a cap wafer directly[134,147] or by means of an intermediate layer of SU-8 [103,106,135] The two layers are brought into contact by stacking the wafers and applying sufficient load on the wafer stack. Crosslinking can be achieved by either UV light[135] or heat[102]. A limitation of crosslinking by UV exposure is that at least one wafer has to be transparent. On the other hand, crosslinking by heat requires the temperature to exceed the glass transition temperature of the un-crosslinked intermediate SU-8 layer, which can cause the SU-8 to reflow into the channel due to capillary actions, and clog the channels. In either case, it is very important to maintain intimate contact between the structural and bonding layers to achieve a satisfactory bond. Intimate contact between the two layers depends on the thickness uniformity of SU-8 film, which can vary significantly in common SU-8 processes[120]. Such variation of thickness can impede proper bonding/sealing characteristics in SU-8 based microfluidic systems. To address this challenge, Svasek *et. al.* developed a method by combining SU-8 and metal layers[147]. In their method, a metal layer is deposited and patterned on top of a patterned SU-8 structural layer. The patterned metal layer is then used as a mask to form SU-8 walls that are selectively crosslinked such that the mid section of the wall remains un-crosslinked. When a cap wafer is brought into contact and heated to a desired bonding temperature, the un-crosslinked SU-8 in the middle can reflow to compensate for the thickness non-uniformity. The crosslinked section of the wall, on the other hand, limits this flow of un-crosslinked SU-8 into the channels. While this is a clever method for obtaining

satisfactory bonds, it requires additional steps of patterning and removing metal layers on top of the SU-8 structural layer. This involves additional equipment and makes the bonding process a fairly complicated one.

The objective of this section is to present a simple, cost effective SU-8 based wafer bonding technique that is free from the common limitations of existing SU-8 based bonding techniques. This method utilizes a selectively exposed SU-8 intermediate layer which is aligned with the structural layer such that the hardened portion of the intermediate layer sits on the open end of the channels and the un-crosslinked portion of the intermediate layer sits on the channel walls during the bonding process. In this manner, flow of un-crosslinked SU-8 at the glass transition temperature does not cause clogging of channels during the bonding process and can compensate for the film thickness non-uniformity of the structural layer as well. Bonding is achieved by thermal means and thus a transparent cap wafer is not necessary. Moreover, the process does not require additional equipment (e.g. metal deposition) that is not common to SU-8 processing.

5.2.1. Wafer bonding – Materials and methods

5.2.1.1. Materials

SU-8 2100 and SU-8 2010 (Microchem Corp., Newton, MA) were chosen to obtain thick (>50 μm) and thin (~10 μm) film of SU-8, respectively. SU-8 was processed using a *WS-400A-6NPP/Lite* spinner (Laurell Technologies, North Wales, PA), a hot plate (VWR Scientific Products, West Chester, PA), a *C-005* convection oven (Lindberg/Blue M, Asheville, NC) and a *MA6/BA6* mask aligner (Karl Suss Inc., Garching/Munich, Germany). SU-8 developer from Microchem was used to develop the processed SU-8

films. Wafer bonding was performed in an EV-501 (EV Group, Tampe, AZ, USA) wafer bonder. 400 -500 μm thick 4" Pyrex 7740 wafers (Mark Optics, Santa Ana, CA) were used as the primary substrate. Pyrex wafers were chosen over Silicon wafers so that wafer bonding results could be investigated via optical methods. 31 gauge (ID 100 μm, OD 238 μm) non metallic syringe needles (MicroFil^{TM}, World Precision Instruments, Sarasota, FL) were used for microfluidic interconnections. Film thickness was measured using an ABSOLUTE Digimatic Indicator (Model # ID-C-112E, Mitutoyo USA) and an optical microscope to focus on the top and bottom of the SU-8 layers.

5.2.1.2. Open microchannel fabrication

The Pyrex wafers were cleaned in Piranha solution and then dehydrated at 150C overnight. The desired thickness of the open channels on the Pyrex wafer (base wafer) was ~250 μm. In order to obtain the desired thickness of the open channels, a multilayer approach was utilized. The first layer (~10 μm) was fully cross-linked and acted as the 'adhesion layer' to improve adhesion to Pyrex[107]. The variation of thickness within a spin coated SU-8 film at a spin speed (rpm) less than 2000 rpm has been shown to vary significantly[120]. Based on Microchem specifications, SU-8 2100 would have to be spun at less than 2000 rpm to obtain the desired thickness in a single coat. To avoid spinning at less than 2000 rpm, two coats of SU-8 were applied at a spin speeds greater than 2000 rpm. The microfabrication scheme and the parameters for the open microchannel formation are presented in Figure 5.2-1 and Table 5.2-1, respectively.

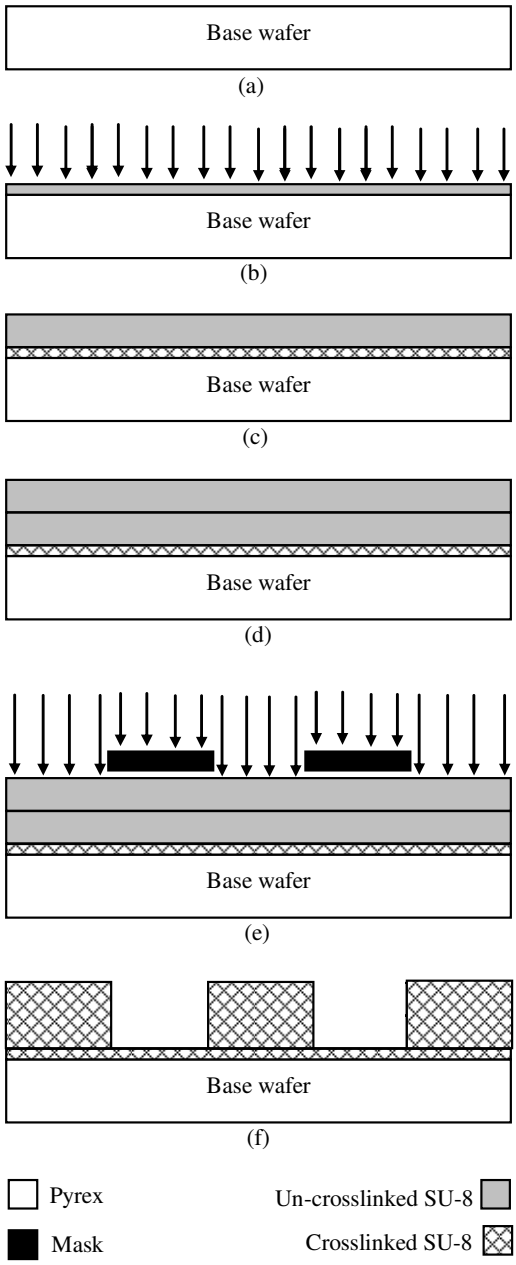

Figure 5.2-1: Schematic cross-section diagram showing the processing steps for the fabrication of open microchannels on Pyrex: (a) Piranha cleaned and dehydrated Pyrex wafer; (b) Apply ~10 µm SU-8 2010, soft bake, blanket expose and PEB; (c) Apply ~125 µm SU-8 2100 and soft bake; (d) Apply ~125 µm SU-8 2100 and soft bake; (e) Expose through mask to pattern the layers of SU-8 2100 simultaneously and PEB; (f) Develop SU-8 2100 layers

Table 5.2-1: Process parameters for the fabrication of open microchannels with SU-8

Layer 1	**Target**	**10 microns, SU-8 2010**
	Spin	2250 rpm, 45 sec
	EBR	300 rpm, 30sec
	Soft-bake	1 min 65C, 6 min 95C
	Cool down	5 min
	Expose	15 sec @ 15mW, Blanket
	PEB	95C, 15 min
	Cool down	5 min
Layer 2	**Target**	**125 microns, SU-8 2100**
	Spin	2250 rpm, 45 sec
	EBR	300 rpm, 30sec
	Soft-bake	2 min 65C, 55 min 95C
	Cool down	5 min
Layer 3	**Target**	**125 microns, SU-8 2100**
	Spin	2250 rpm, 45 sec
	EBR	300 rpm, 30sec
	Soft-bake	2 min 65C, 55 min 95C
	Cool down	5 min
	Expose	35 sec @ 15mW, Through-mask
	PEB	95C, 60 min
	Develop	SU-8 developer, 12-15 min

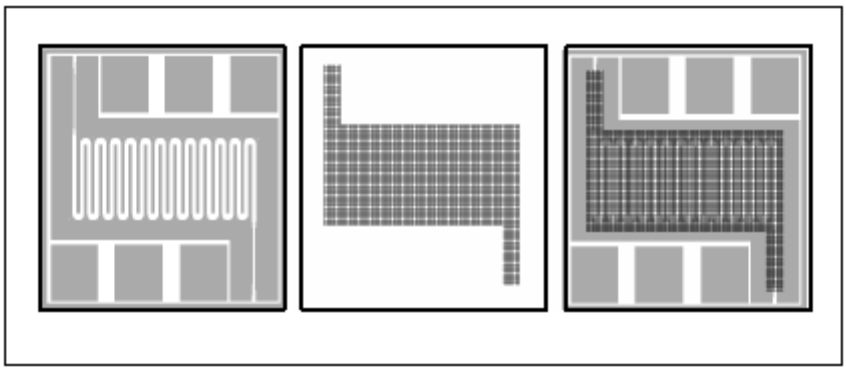

(a)

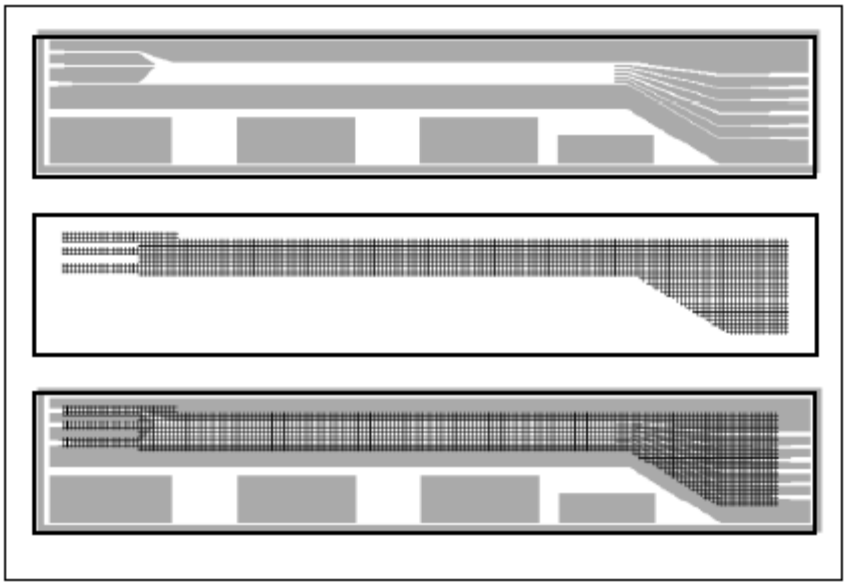

(b)

Figure 5.2-2: Schematic diagram showing mask designs for different kinds of channels: (a) serpentine channel design; (b) channel design for hydrodynamic focusing

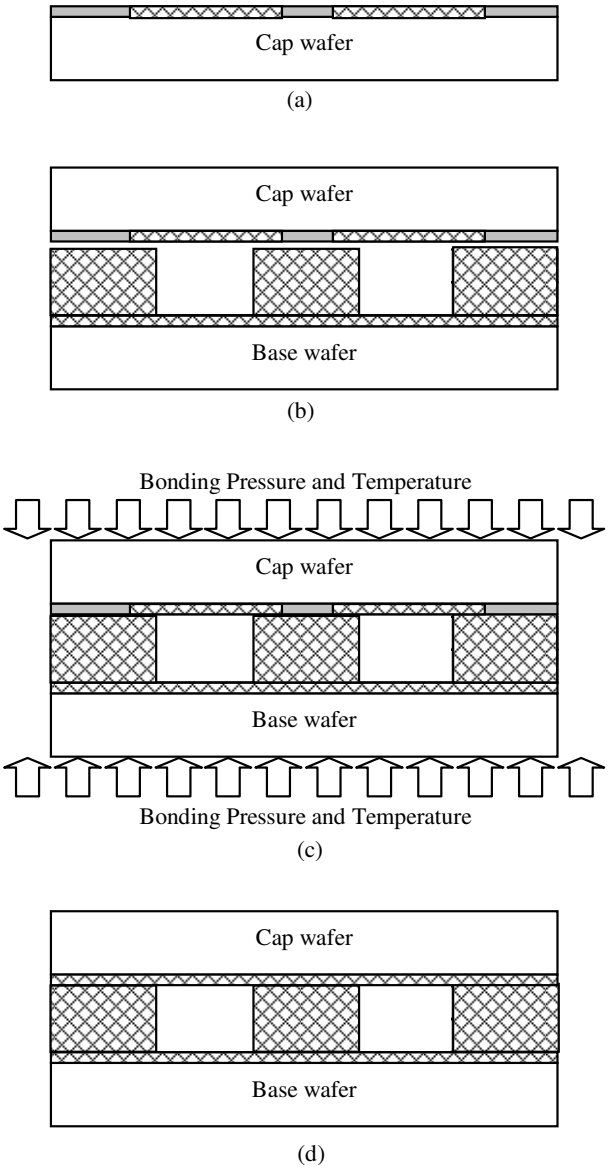

Figure 5.2-3: Schematic cross-section diagram showing the bonding technique (a) A cap wafer is coated with SU-8 2010 and selectively exposed as per table 2; (b) The cap wafer is aligned to the open microchannel such that the exposed section of the cap wafer sits on top of the open ends of the microchannels; (c) Apply heat and pressure in a bonder; (d) Enclosed microchannels.

5.2.1.3. Bonding

Three thin layers of SU-8 were applied on a second Pyrex wafer (cap wafer). The first layer (~10 μm) was fully cross-linked and acted as the 'adhesion layer' to improve adhesion to Pyrex. The second (~10 μm) and third (~5 μm) layer ('Bond formation layers') were exposed through a mask using a special sequence such that the exposed portions were crosslinked to a point that they were hard enough not to deform significantly but can crosslink further during the final bonding step. The masks (Figure 5.2-2) were designed according to the open microchannel network so that the exposed portion sits on top of the open sections of the channels. The cap wafer was then aligned on top of the base wafer with the SU-8 films facing each other on the stage of the bonder. Bonding was performed at 400N and 95C for 1 hour. The processing parameters for the bond formation layers are presented in Table 5.2-2 and the bonding steps are schematically presented in Figure 5.2-3.

5.2.2. Wafer bonding – Results and Discussion

5.2.2.1. Adhesion of thick SU-8 to Pyrex

Pyrex is a common substrate used in microfluidic devices. Oftentimes it is desired to have optical access inside the microchannels to obtain desired information from the microfluidic device. Adhesion of thick (~100 μm) SU-8 on Pyrex substrates is known to be less than ideal[107,131,132]. However, the adhesion can be improved by using a thin (~10 μm), fully crosslinked layer of SU-8 as an intermediate adhesion layer[107] We investigated SU-8 adhesion to Pyrex by observing the adhesion of 10 mm by 10 mm square structures on Pyrex at different thicknesses. Thin (~10 μm) SU-8 did not show any adhesion problem whereas thick (~100 μm) layers showed immediate delamination at the corners

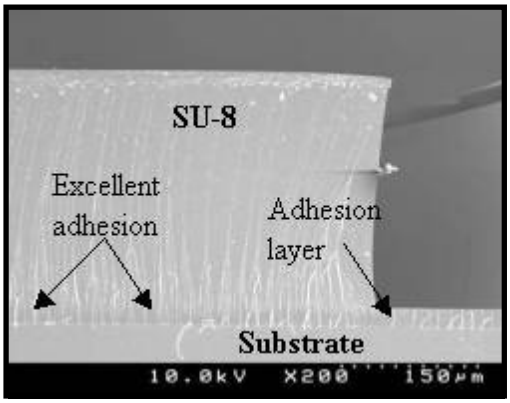

Figure 5.2-4: SEM micrograph showing the cross-section of an open SU-8 channel on Pyrex substrate

following the solvent development step. Residual stress in SU-8 increases with the increase in film thickness. Good adhesion from the thinner SU-8 films indicated that the residual stress build up in thicker SU-8 was the underlying cause for the adhesion failure. When a highly crosslinked thin SU-8 layer was used as an intermediate layer (adhesion layer), the adhesion properties improved significantly. This improvement may be due to the fact that the thick SU-8 layer is no longer adhering to Pyrex directly, rather, it is adhering to a more flexible SU-8 surface. This can allow the intermediate layer to act as a stress buffer to compensate for the extra residual stress buildup on the thick layer and improve the overall adhesion characteristics. Evidence of overall stress reduction can also be investigated by observing crack-like distortions in the SU-8 film. Crack-like distortion is common in SU-8 structures and is known to occur due to residual stress in the film[120]. In our experiments, hardly any crack-like distortions were visible in the multilayered structures. This also indicates that the stress in the overall film is reduced by utilizing the highly crosslinked intermediate layer of SU-8. Figure 5.2-4 shows a cross-section of an open SU-8 channel fabricated on Pyrex using the proposed adhesion layer.

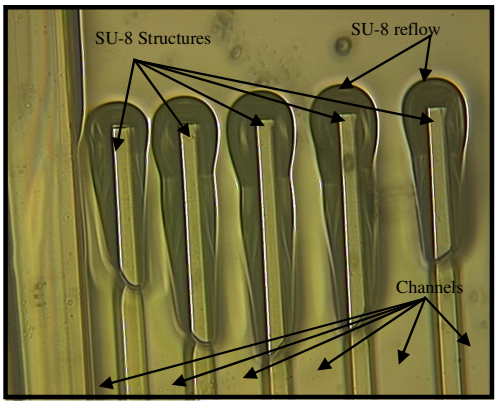

(a)

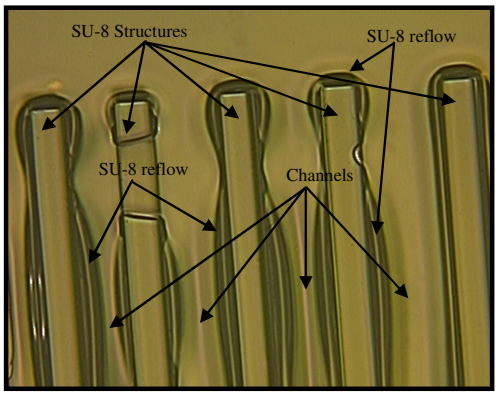

(b)

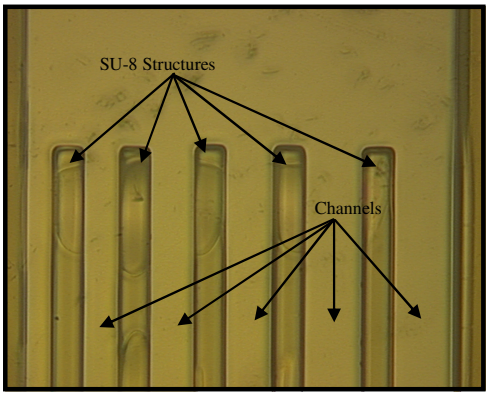

(c)

Figure 5.2-5: Optical microscope (5x) pictures showing bonding outcome from the top of the bonded channel (through the transparent cap wafer) based on different exposure dosage of the bond formation layer: (a) 0 seconds; (b) 4 seconds; and (c) 8 seconds

5.2.2.2. Bond formation

The critical components to a sustainable bond are (1) the thickness uniformity of the open microchannels and (2) the ability of the bond formation layers to obtain sufficient crosslinking with the open ends of the microchannels.

The thickness uniformity of the spin coated SU-8 can depend on the type of spinners utilized for spin coating. In our spinner, the thickness variation was very large (± ~50 μm) when a film of thickness ~250 μm was obtained on a single coat (1000 rpm). However, the thickness variation was reduced to ± ~15 μm when the thickness of ~250 μm was obtained using two coats of SU-8 at a higher spin rate (2250 rpm).

It was important that the bond formation layer was soft enough so that when the two wafers are stacked together and held under pressure, there is intimate contact in locations where crosslinking between the structural layer and bond formation layer is desired. One way to compensate for the thickness variation of the structural layer was to use a soft bond formation layer. This way, when the two wafers are stacked together and subjected to sufficient load, the bond formation layer can deform to compensate for the thickness non-uniformity of the structural layer. A soft bond formation layer can be obtained by reducing the exposure dosage on the SU-8 film[116]. We investigated the effect of exposure dosage reduction on the bond formation layer with respect to the outcome on the bonding. The bonded wafers were investigated under a microscope through the transparent cap wafers. Figure 5.2-5 shows the effect of different exposure times on the bonding. Bond formation layers exposed at 0 seconds and 4 seconds showed evidence of SU-8 reflow into the channels during the bonding process. On the other hand, at 8 seconds exposure, the bonds showed no evidence of SU-8 reflows into the channels. All

these bonded wafers were then subjected to dicing tests - Bonded wafers were diced using a dicing saw (DAD 320, Disco Corporation, Tokyo, Japan). A successful bond was determined by the ability of the bond to withstand the dicing process where the wafers are subjected to high shear and water jets. Bonded wafers that were exposed at 0-6 seconds were able to withstand the dicing process where as the wafers exposed at 8-10 seconds failed during dicing. These experiments resulted into two important findings: (1) Bond formation layers exposed at 8-10 second were able to form bonds that did not cause reflow but the bond quality was not strong enough to undergo the wafer dicing process, and (2) Bond formation layers exposed at 0-6 seconds resulted in reflow but the bond quality was strong enough to undergo the wafer dicing process. In order to benefit from both cases, a new bonding protocol was formulated. The bond formation layer could be exposed selectively using a mask (cap design mask) such that, (1) the part of the bond formation layer that sits on top of the open portion of the microchannels be exposed for > 8 seconds, and (2) the part of the bond formation layer that sits on the walls of the microchannels be exposed for < 6 seconds. When the wafers were bonded using this combination, no reflow was observed into the microchannels and the bonded wafers were able to withstand the wafer dicing process. However, when these diced channels were tested for leakage around the channels, the devices still showed insufficient bonding throughout the device. The leakages were especially evident in large area microchannels. This indicated that there was not sufficient reflow of the SU-8 over the channel walls to form leakage free enclosed microchannels. Leakage free bonds depended on the ability of SU-8 to reflow on the channel walls and compensate for the non-uniformity of the structural layer. When the bond formation layer was soft baked at 95C to evaporate all

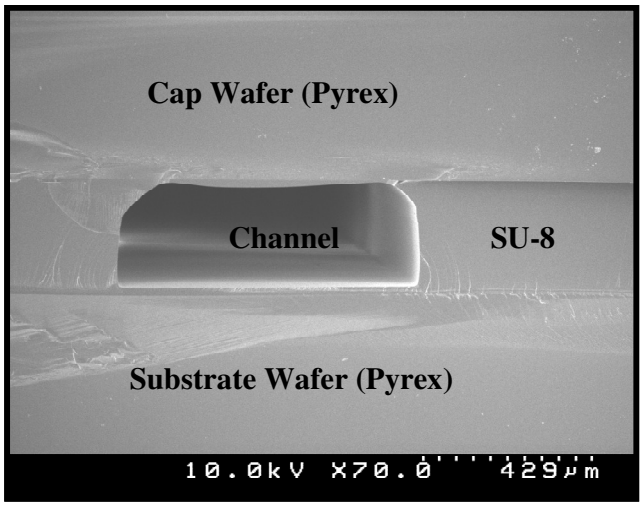

Figure 5.2-6: SEM micrograph showing the cross-section of an enclosed microchannel.

the solvents, the viscosity of SU-8 alone may not have been suitable to create sufficient reflow. For this reason, the bond formation layer was subjected to a maximum soft bake temperature of 65C. The thickness of the bonding layer was also critical to the ability of forming a proper bond. We have found that one layer of SU-8 2010 spun at 2250 rpm was not sufficient to form a leakage free bond. Therefore, the thickness was increased by adding a second layer of thin (spun at 3500 rpm) SU-8 on top of the first bond formation layer. It was then aligned and exposed through the cap design mask for 10 seconds. This additional step remarkably improved the overall bonding characteristics of the proposed method and was essentially added to the final bonding protocol. In all these experiments, the cap wafer was first coated with a highly crosslinked adhesion layer of SU-8 as described in section 3.1. We found that this layer was also very important for the bonding process. Bonded wafers without the adhesion layers frequently failed during the dicing process. An SEM micrograph of the cross section of an enclosed microchannel is presented in Figure 5.2-6.

One limitation of this bonding process is that the cap wafer has to be aligned with the bonded wafer before bonding is performed. Depending on the type of structures, the masks can be designed such that only gross alignment is sufficient for the bonding. The smallest microchannel we fabricated was 100 μm wide. The channel walls were at least 500 μm wide. As a result, in our case we did not require fine alignment tools to align the wafers. However, with the use of aligner/bonder equipment one could easily fabricate channels with much smaller dimensions.

5.3. Electroplating mold formation

There have been significant reports on the utilization of SU-8 as an electroplating mold in the literature[110-113]. One limitation with SU-8 is that it is difficult to process and remove after electroplating[148]. There are other thick photoresists such as the epoxy based negative photoresist KMPR[149], the novalak based positive photoresist SPR 220-7[150] and acrylate based dry film negative photoresist Ordyl P-50100[151]. However, there is limited information available with respect to the processing parameters, stability and capabilities of these photoresists in the literature. Koukharenko *et al* carried out a comparative study on the applications of SU-8, SPR 220-7 and Ordyl P-50100 photoresists as thick electroplating molds[152]. Within their limited study of plating Nickel in a Nickel Sulphamate bath, they concluded that Ordyl P-50100 was a better alternative to SU-8 as thick electroplating molds. Nevertheless, this study was limited to alkaline plating baths and the conclusion was drawn based on the ease of removal of the photoresist after plating rather than the quality of the photoresist as the plating mold. For the development of our devices, it is not necessary to remove the photoresist after plating and therefore, the complexity of the removal of the mold after plating was not considered. One

limitation with SU-8 is that the adhesion of SU-8 is poor to Pyrex and metallic surfaces[107,131,132] Early in 2007, MicroChem introduced the KMPR photoresists which have better adhesion properties to glass and metal surfaces and are specially marketed for electroplating applications. However, KMPR was not available at the time this research project was started.

The objective of this section is to present the development of electroplating molds that can be utilized to obtain the discrete pole-pieces. The mold is composed of a patterned seed layer and a patterned SU-8 layer. Adhesion of SU-8 mold to an underlying Pyrex and Ni seed layer was improved by using a highly crosslinked, patterned SU-8 layer. Patterned adhesion layers ensured better adhesion without insulating the seed layer on the desired location.

5.3.1. Mold formation – Materials and methods

An electroplating mold is composed of a conductive seed layer and layer of photoresist structures to define the metal components.

5.3.1.1. Patterned seed layer formation

Un-patterned seed layers can be obtained by depositing metal layers using a commercial sputtering tool. The metal layer is then selectively etched using appropriate metal etchants. Standard photoresist is used to coat and define photolithographic patterns on the metal surface. During the etching process the coated portion is not exposed to the etchant and the rest of the metal film is etched away. Several parameters need to be optimized to obtain the final patterned seed layer. In this work, ~200Å Cr and ~2000Å Ni were deposited on a piranha cleaned Pyrex wafer using a commercial sputtering tool (Discovery ^{TM} – 24, Vacuum Deposition System, Denton Vacuum Inc, Moorestown, NJ).

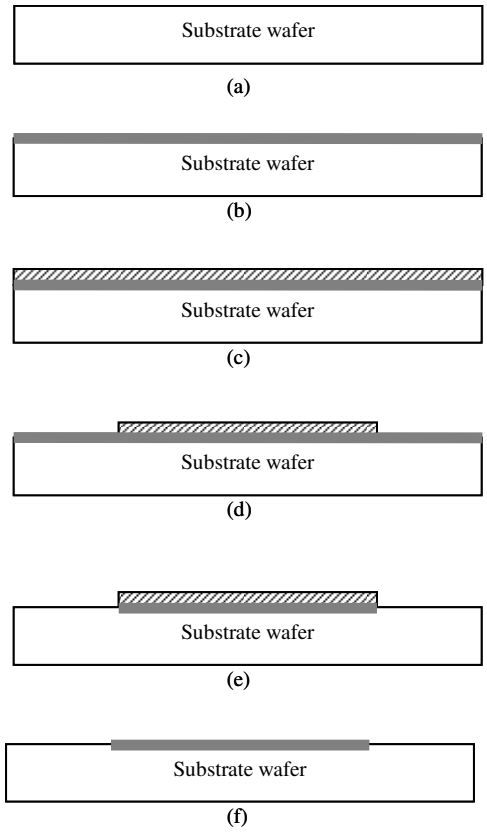

Figure 5.3-1: Schematic cross-section diagram showing the development of the patterned seed layers: (a) Start with the substrate wafer; (b) Deposit metal layer on the substrate wafer; (c) Spin-coat standard photoresist; (d) Pattern photoresist; (e) Etch metal layer; (f) Remove residual photoresist

Standard Photoresist (Microposit ™ S1813™ Positive Photoresist, Rohm and Haas Electronic Materials, Marlborough, MA) was utilized for photolithography using a commercial spinner (Model# 5110/C, Solitec Inc., Santa Clara, CA) and MA6/BA6 mask aligner (Karl Suss Inc., Garching/Munich, Germany). Exposed photoresist was removed using an appropriate developer solution (MicroDev, Microposit ™ developer concentrate, Rohm and Haas Electronic Materials, Marlborough, MA). Two types of metal etchants, nickel etchant solution (Nickel Etchant, Type TFB, Transene Company, Danvers, MA) and Ni-Cr etchant (Nichrome Etchant, Type 10, Transene Company, Danvers, MA) was utilized for the metal etching process. The microfabrication scheme and the parameters

Table 5.3-1: Process parameters for conductive seed layer

Step 1		**Photolithography**
	Spin	4000 rpm, 30 sec, Std Photoresist
	Soft Bake	1 min, 95 C, Hot Plate
	Expose	15 sec @ 15mW, Through Mask
	Develop	1:1 MicroDev & DI water, 100 sec, gentle agitation
	PEB	115C, 1 min
Step 2		**Metal Etch**
	Dip	Ni etchant, until complexion changes, 30C, moderate agitation
	Rinse	DI water, 3 times
	Dip	Ni-Cr etchant, until clearing of surface, 25C, gentle agitation
	Rinse	DI water, 3 times
Step 3		**PR removal**
	Rinse	Acetone, spinner at 4000rpm, 30 sec

for the patterned seed layer formation are presented in Figure 5.3-1 and Table 5.3-1, respectively.

5.3.1.2. Mold formation layer

The development of 100 μm thick SU-8 molds on the Pyrex wafers with patterned seed layers is somewhat similar to the development of thick microchannels on Pyrex substrate as described in section 5.1.1.2. However, there is a key difference. Utilization of a highly cross-linked and 'un-patterned' adhesion layer is not feasible for a plating mold. The underlying metal seed layer must be exposed so that electrochemical reactions can take place during the plating process. For this reason, the adhesion layer was patterned before cross-linking the layer. The parameters and microfabrication scheme

Table 5.3-2: Process parameters for the fabrication of the SU-8 molds

Layer 1	**Target**	**10 microns, SU-8 2010**
	Spin	2250 rpm, 45 sec
	EBR	300 rpm, 30sec
	Soft-bake	1 min 65C, 6 min 95C
	Cool down	5 min
	Expose	15 sec @ 15mW, Through-mask
	PEB	95C, 15 min
	Cool down	5 min
Layer 2	**Target**	**20 microns, SU-8 2010**
	Spin	1750 rpm, 45 sec
	EBR	300 rpm, 30sec
	Soft-bake	2 min 65C, 10 min 95C
	Cool down	5 min
Layer 3	**Target**	**125 microns, SU-8 2100**
	Spin	2250 rpm, 45 sec
	EBR	300 rpm, 30sec
	Soft-bake	3 min 65C, 55 min 95C
	Cool down	5 min
	Expose	26 sec @ 15mW, Through-mask
	PEB	95C, 30 min
	Develop	SU-8 developer, 12-15 min

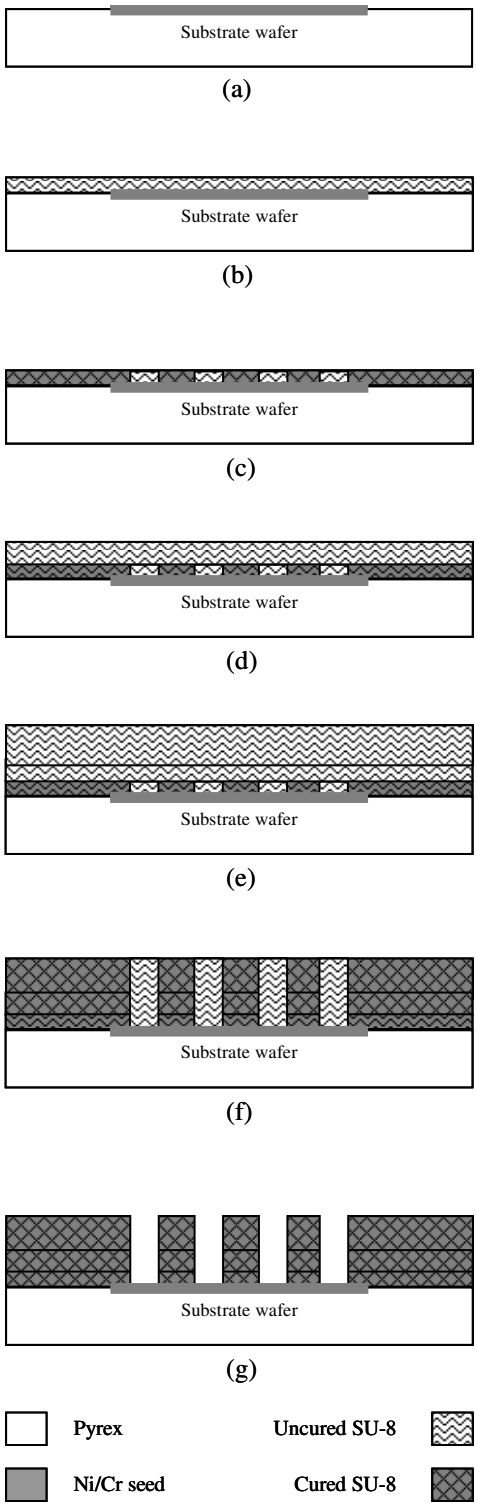

Figure 5.3-2: Schematic cross-section diagram showing different steps in fabricating the plating molds: (a) Start with substrate already patterned with the metal layer; (b) Spin-coat layer 1 (~10 μm) SU-8 and pre-bake; (c) Expose and PEB thin layer; (d) Spin-coat layer 2 (~20μm) SU-8 and pre-bake; (e) Spin-coat layer 3 (~100μm) SU-8 and pre-bake; (f) Expose layer 2 & 3 simultaneously; (g) Develop the three layers simultaneously

for the mold layer formation are presented in Table 5.3-2 and Figure 5.3-2, respectively.

5.3.2. Mold Formation – Results and discussion

5.3.2.1. Seed Layer

The metal etch involved a two step process. Ni etchant alone should be able to etch the thicker Ni layer and the thinner Cr layers. However, the Ni etchant seemed to react with the underlying Cr layer faster than the Ni layer on the top. As a result, the metal layers protected by the patterned photoresist were experiencing anisotropic etching and resulted in significant undercuts. In fact, smaller features (~8 μm) in the alignment marks were lifted off due to the undercuts. In order to avoid lift off of smaller features in the alignment marks, the two step metal etching was adopted. Since the ratio of thickness between Ni and Cr was about 10, the wafers were immersed under Ni etchant for a period sufficient to etch most of the Ni away. It was observed that when a large portion of the Ni is etched away the complexion of the wafer surface undergoes a sharp change in appearance. The shiny Ni is no longer visible at this point. Rather, the surface becomes darker (gray) and the photoresist patterns become more visible. At this point the wafer is taken out from the etchant and washed. The wafer appears semi-transparent at this point (objects under the wafer can be visible through the dark layer of Cr). The wafer is then dipped in a second etchant that is specially designed to etch Ni and Cr simultaneously. This etchant is designed to etch Cr and Ni at a similar rate and thus, any left over Ni and the Cr is dissolved. When the wafer becomes completely transparent (except in the patterned locations), the wafer is taken out and washed in DI water. The use of this two step approach showed significant improvement in the etching process. Investigation

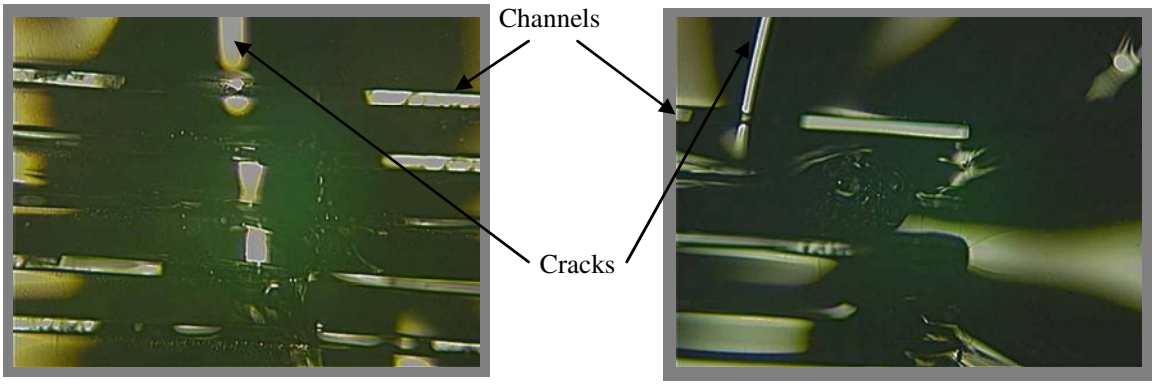

Figure 5.3-3: Optical microscopic (5X) picture showing large cracks formed during the fabrication of a two layers plating mold with SU-8.

under the microscope revealed successful etching of the metal layer without any undercuts. The metal etching process is very sensitive to the thickness of the films. In this case, there was often variation in sputtered film thickness from wafer to wafer. For some wafers the initial Ni etching took longer (10 - 40 sec) than the others. Therefore, multiple wafers were not suitable to be etched simultaneously. Each individual wafer was etched separately to ensure that they were etched properly.

5.3.2.2. Plating Mold

The initial approach was to apply the adhesion layer and pattern that layer such that the features are aligned with the underlying seed layer. After the Post Exposure Bake (PEB) step for the adhesion layer, the thick (~120 μm) mold layer is applied in 'one' coat and exposed with proper alignment using the same mask. Following the PEB step of the mold layer, both the layers can be developed simultaneously. In this way, the patterned adhesion layer and the patterned structural layer would be aligned. When they are developed simultaneously, uncrosslinked portion of both the adhesion layer and the structural layer would be removed – leaving the seed layer exposed and the structural layer adhering to the adhesion layer. However, during the soft baking step after the

second thick layer is applied, it was found that large cracks (Figure 5.3-3) were forming on the thick SU-8 layer. These cracks were very large and were clearly visible with the naked eye. The cracks caused significant deformation in the areas where the mold was to be patterned making the layers ineligible for further processing. The formation of cracks was very consistent between experiments. The cracks may have been caused by inconsistent reflow of the thick SU-8. Since the underlying layer has been selectively exposed – part of this layer is hardened. When the thick layer is applied on top of the selectively exposed layer and is subjected to the soft bake temperature, part of the underlying layer becomes soft and viscous whereas the rest of the film stays hardened. This difference in hardness/densities in the underlying layer may cause the cracks to originate and propagate in the overlaying SU-8 film. The cracks seem to originate at the interface of the exposed and unexposed SU-8 in the underlying SU-8 layer. The cracks form within the first few minutes of the soft baking step and get bigger with time at the soft baking temperature.

Since the cracks may have been caused by the difference in densities in the underlying layer, it may be possible to minimize crack formation by reducing the amount of SU-8 placed on top of this layer, i.e. apply a thinner film on top of the patterned adhesion layer instead of applying the thick SU-8 layer. Therefore, the effect of the thickness of the overlying layer on the formation of the cracks was investigated by applying SU-8 of different thicknesses (e.g. ~10 μm, ~20 μm & ~50 μm). It was found that no cracks were formed with ~10 μm and ~20 μm overlying layer. While this result was encouraging, our objective was to obtain molds that were ~100 μm thick. In order to achieve the desired thickness, 100 μm thick SU-8 was applied following the soft bake

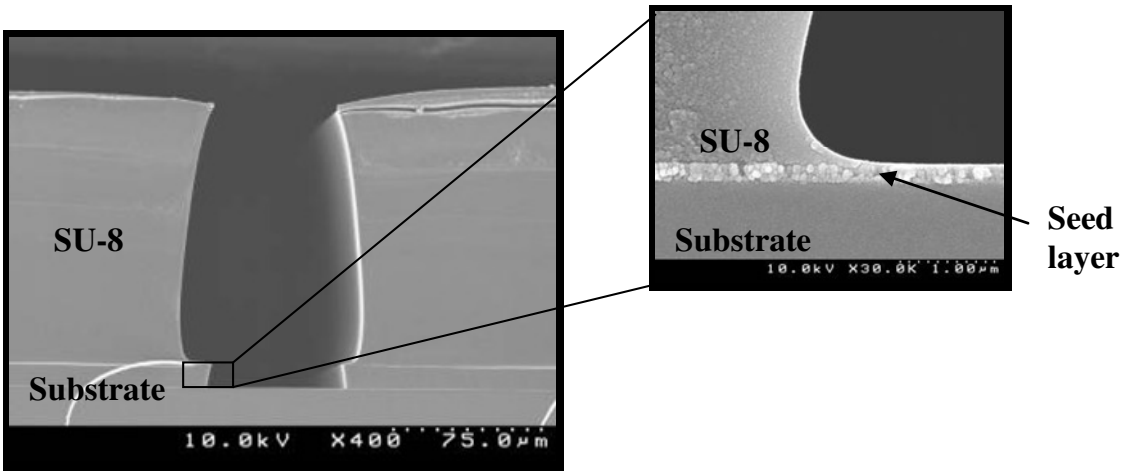

Figure 5.3-4: SEM micrograph showing cross-section of plating mold – the seed layer is exposed to allow flow of electrical charge

step of the second layer (10 µm and 20 µm thick). The soft baking step of this third layer was then carefully observed to check for any crack formation. It was found that cracks were still forming when the thickness of the second layer was at 10 µm. However, at 20 µm thickness of the second layer, no cracks were observed. Based on these results, the final fabrication of the electroplating mold was formulated using a three layer approach. The first layer (~10 µm thick) was photolithographically patterned and cured. Then the second layer (~20 µm thick) was applied and soft baked to remove solvents. The third layer (~ 100 µm) was applied on top of the second layer, which had already been soft baked and cooled. Following the soft bake of the third layer, both the second and third layer was exposed (aligned with the first exposed layer) and cured in PEB, simultaneously. Finally all three layers were developed at the same time to obtain the finished plating molds. SEM micrograph of the cross-section of a successfully developed electroplating mold is presented in Figure 5.3-4. It can be seen the adhesion of the mold to SU-8 was excellent and the seed layer is not covered with the adhesion layer.

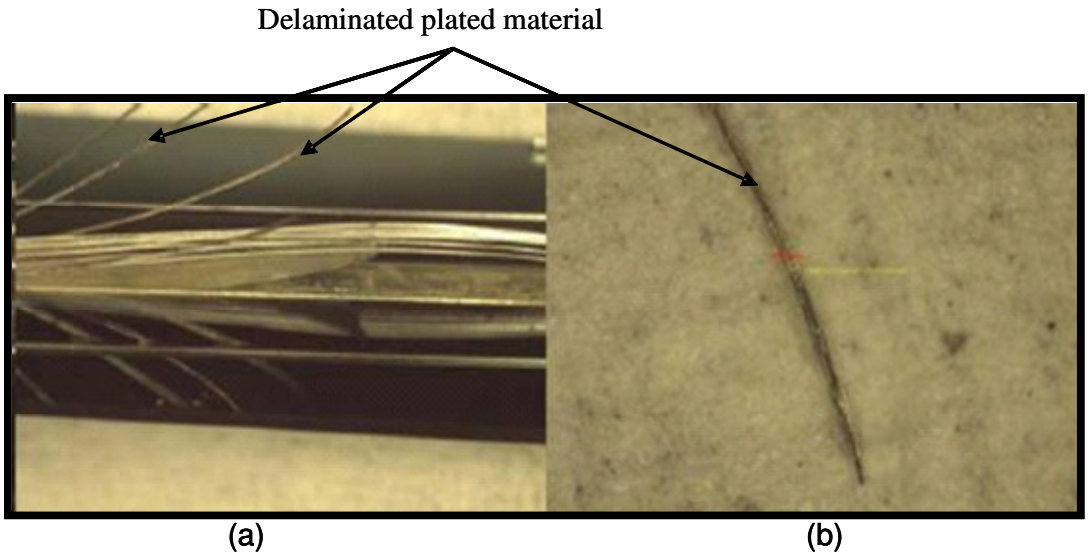

Figure 5.4-1: Photograph showing delaminated plated materials

5.4. Electrodeposition of thick Ni50Fe50

The electroplating molds were sent to Integran Technologies Inc., Toronto, Ontario, Canada to develop a process for depositing ~100 μm thick alloy of Ni-Fe (50/50). After the first and second set of experiments Integran was able to plate the material with moderate success. Stress in the plated films was the key problem. Although the alloy was plated in the desired region, the material buckled due to the high film stress which caused the material to delaminate (Figure 5.4-1) from the substrate. Nevertheless, the results were still encouraging since,

- The plating molds were stable enough to withstand the plating condition and the plating process
- It was possible with Integran's proprietary technology to plate ~100 μm thick Ni-Fe (50/50) alloy. Integran reported that the Fe content in the plated material was between 50-52%.

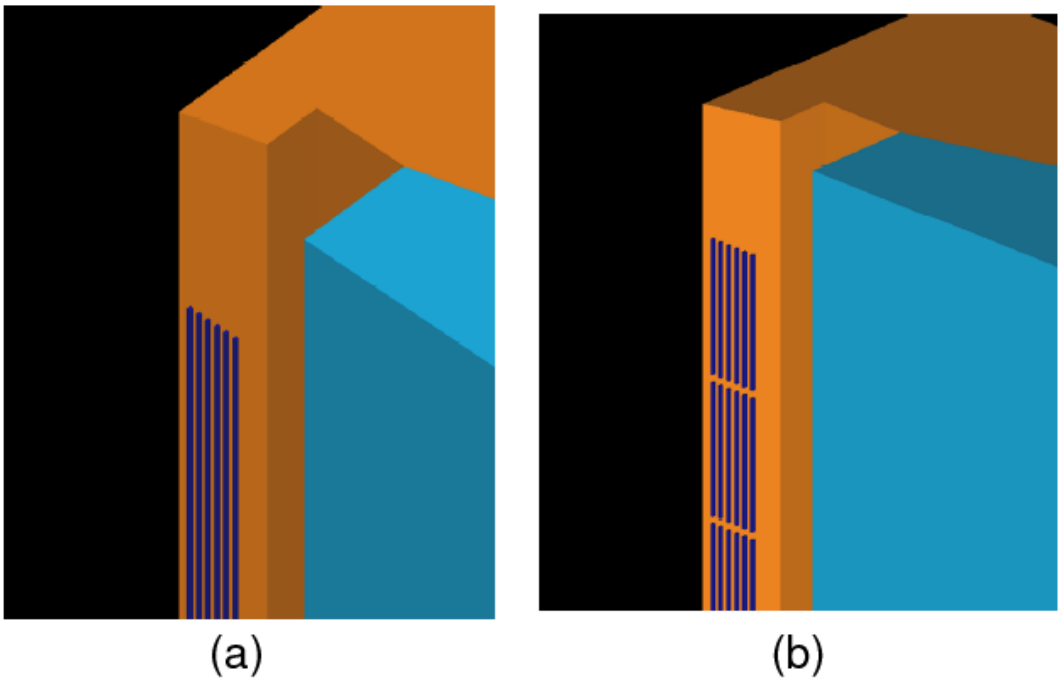

Figure 5.4-2: Schematic diagram showing (a) continuous and (b) segregated discrete pole piece

In order to address the delamination problem of the deposited structure, the magnetic design was further investigated for alternate options to 30 mm long discrete pole-pieces. The magnetic design was modified such that the 30 mm long continuous discrete pole-pieces were replaced by segmented discrete pole-pieces – a set of 1 mm long pole-pieces

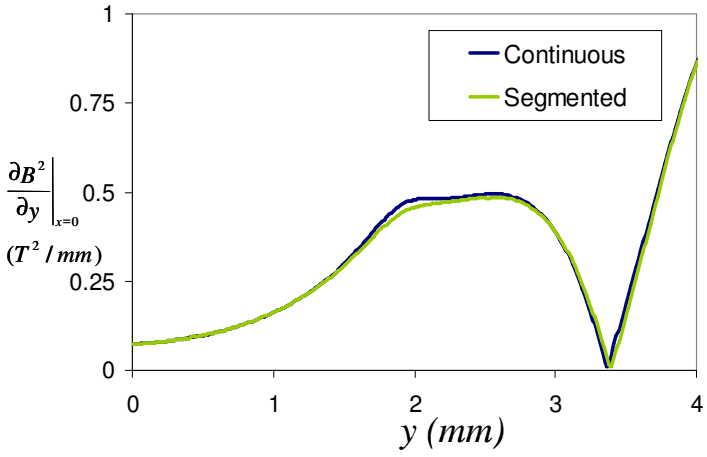

Figure 5.4-3: Graphs showing magnetic energy density distribution with continuous and segregated discrete pole-pieces

separated by 200 µm gaps along the z axis (Figure 5.4-2). 3D magnetic simulation showed that the segmented pole-pieces could produce the same kind of magnetic field that was obtained by the continuous pole-pieces (Figure 5.4-3). Therefore a new design with the segregated pole-pieces was incorporated into the plating mold and sent to Integran. Integran utilized the same electroplating process that was optimized based on the first two set of experiments. Reducing the length of the discrete pole-pieces improved the adhesion of the discrete pole-pieces and the pole-pieces were deposited successfully. Figure 5.4-4 shows the optical and SEM micrographs of the deposited materials.

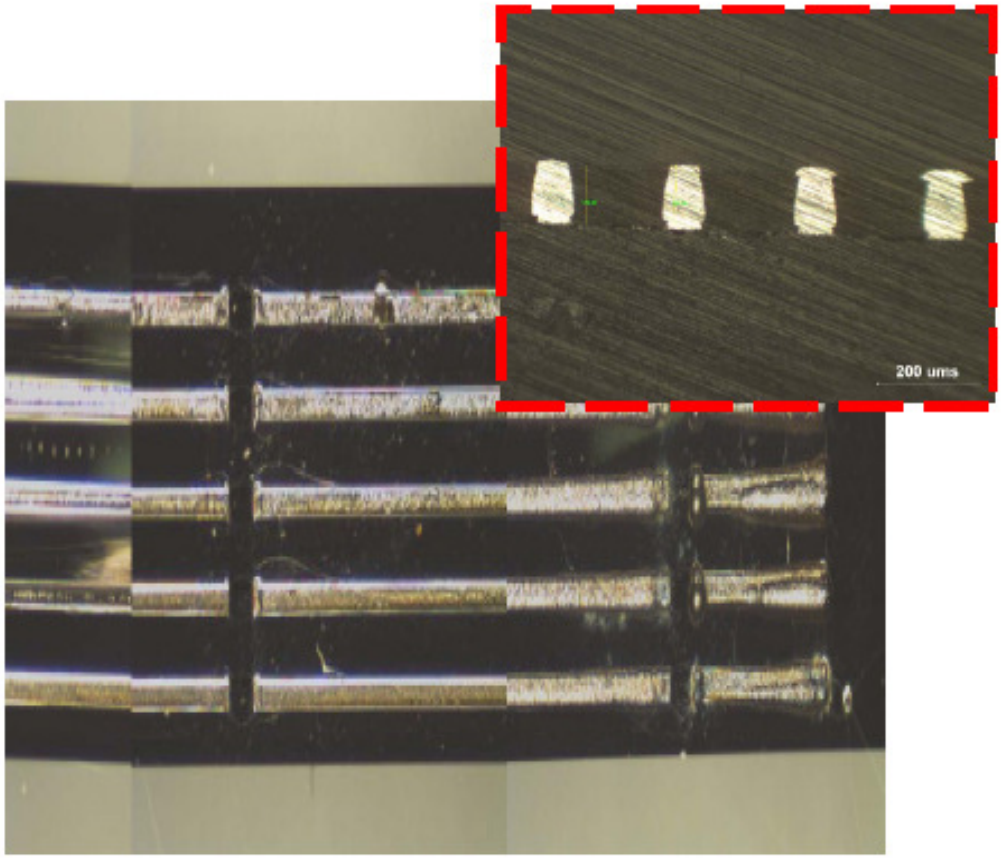

Figure 5.4-4: SEM micrograph showing the electrodeposited materials in the molds (Inset: SEM cross-section of the plated materials)

5.5. Integration of enclosed microchannels and electroplating molds

The integration of the enclosed microchannels and the electroplating molds was a critical part of the overall device development. The separate development of the enclosed channels and the plating molds have already been discussed in the previous sections. However, the integration of the two processes presented new challenges. For example, the SU-8 cannot be completely processed on one side at a time. SU-8 is applied using a spinner. The spinner uses a high vacuum chuck to hold the wafer down during the spinning process. If finished SU-8 structures are present on one side of the wafer, it would not be possible to use the vacuum chuck to hold the wafer to apply the SU-8 on the other side of the wafer. This limitation was addressed by processing the SU-8 on the first side all the way until the development step. At this point the SU-8 layer was patterned and the surface of the film is still fairly uniform to allow the vacuum chuck to hold the wafer. Therefore, the second side was processed all the way until the development stage by placing the first patterned but undeveloped layer facing the vacuum chuck. To protect the features on the first side from getting destroyed from the vacuum chuck, a ~20 μm thick SU-8 layer was applied and soft baked before subjecting the side to the vacuum chuck. Both sides were then developed at the same time. Limitation with this approach was that during the processing of the second side, the hot plates could not be used for baking application. The portions that have not been exposed on the first side can stick to the surface of the hot plate which can lead to contamination of the hot plate and perhaps destruction of the SU-8 features. A simple solution to this problem is to use a bake oven for all the baking steps and use a specially designed tray that can allow the baking of the

Table 5.5-1: Process parameters for the Integration of enclosed microchannels and the SU-8 molds

Substrate **Pyrex wafer with patterned seed layer**		
Layer 1	**Target**	**10 microns, SU-8 2010**
	Spin	2250 rpm, 45 sec
	EBR	300 rpm, 30sec
	Soft-bake	1 min 65C, 6 min 95C
	Cool down	5 min
	Expose	15 sec @ 15mW, Blanket
	PEB	95C, 15 min
	Cool down	5 min
Layer 2	**Target**	**125 microns, SU-8 2100**
	Spin	2250 rpm, 45 sec
	EBR	300 rpm, 30sec
	Soft-bake	2 min 65C, 55 min 95C
	Cool down	5 min
Layer 3	**Target**	**125 microns, SU-8 2100**
	Spin	2250 rpm, 45 sec
	EBR	300 rpm, 30sec
	Soft-bake	2 min 65C, 55 min 95C
	Cool down	5 min
	Expose	35 sec @ 15mW, Through-mask
	PEB	95C, 60 min
	Develop	SU-8 developer, 12-15 min
Cap **Pyrex wafer with patterned seed layer (Table xx)**		
Layer 4	**Target**	**10 microns, SU-8 2010**
	Spin	2250 rpm, 45 sec
	EBR	300 rpm, 30sec
	Soft-bake	1 min 65C, 6 min 95C
	Cool down	5 min
	Expose	15 sec @ 15mW, Blanket
	PEB	95C, 15 min
	Cool down	5 min
Layer 5	**Target**	**10 microns, SU-8 2010**
	Spin	2250 rpm, 45 sec
	EBR	300 rpm, 30sec
	Soft-bake	2 min 65C, 6 min 95C
	Cool down	5 min
	Expose 1	5 sec @ 15mW, Blanket
	Expose 2	10 sec @ 15mW, Through-mask
	PEB	65C, 1 min
	Cool Down	5 min

Table 5.5-1: Continued

Layer 6	**Target**	**5 microns, SU-8 2010**
	Spin	3500 rpm, 45 sec
	EBR	300 rpm, 30sec
	Soft-bake	1 min 65C
	Cool down	5 min
	Expose	10sec @ 15mW, Through-mask
Bond		**Bonder, 95C, 400N, 1 Hr**
	Substrate **side processing**	
Layer 7	**Target**	**10 microns, SU-8 2010**
	Spin	2250 rpm, 45 sec
	EBR	300 rpm, 30sec
	Soft-bake	1 min 65C, 6 min 95C
	Cool down	5 min
	Expose	15 sec @ 15mW, Through-mask
	PEB	95C, 15 min
	Cool down	5 min
Layer 8	**Target**	**20 microns, SU-8 2010**
	Spin	1750 rpm, 45 sec
	EBR	300 rpm, 30sec
	Soft-bake	2 min 65C, 10 min 95C
	Cool down	5 min
Layer 9	**Target**	**125 microns, SU-8 2100**
	Spin	2250 rpm, 45 sec
	EBR	300 rpm, 30sec
	Soft-bake	3 min 65C, 55 min 95C
	Cool down	5 min
	Expose	26 sec @ 15mW, Through-mask
	PEB	95C, 30 min
	Cool down	5 min
Layer 10	**Target**	**20 microns, SU-8 2010**
	Spin	1750 rpm, 45 sec
	EBR	300 rpm, 30sec
	Soft-bake	2 min 65C, 10 min 95C
	Cool down	15 min

Table 5.5-1: Continued

	Cap **side processing**	
Layer 11	**Target**	**10 microns, SU-8 2010**
	Spin	2250 rpm, 45 sec
	EBR	300 rpm, 30sec
	Soft-bake	1 min 65C, 6 min 95C
	Cool down	5 min
	Expose	15 sec @ 15mW, Through-mask
	PEB	95C, 15 min
	Cool down	5 min
Layer 12	**Target**	**20 microns, SU-8 2010**
	Spin	1750 rpm, 45 sec
	EBR	300 rpm, 30sec
	Soft-bake	10 min 95C
	Cool down	5 min
Layer 13	**Target**	**125 microns, SU-8 2100**
	Spin	2250 rpm, 45 sec
	EBR	300 rpm, 30sec
	Soft-bake	3 min 65C, 55 min 95C
	Cool down	5 min
	Expose	26 sec @ 15mW, Through-mask
	PEB	95C, 30 min
	Develop **both sides** ***simultaneously***	
	Develop	SU-8 developer, 12-15 min

SU-8 on both sides of the wafer. It should also be considered that the SU-8 layer on the first side would undergo the same baking steps twice.

Due to all these restrictions, the process to integrate the microchannels with the plating molds was not just simply a matter of adding the two processes. A new process had to be optimized to obtain the final integration. The microfabrication parameters for integration of the enclosed microchannels and the plating molds are presented Table 5.5-1. Optical and SEM micrographs of a successfully integrated device (without the plated materials) are presented in Figure 5.5-1.

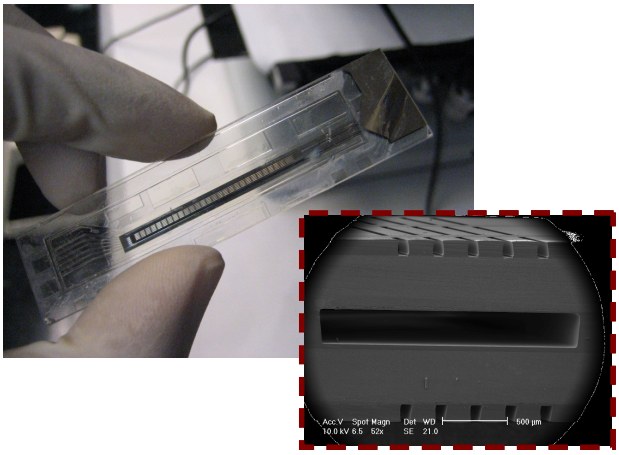

Figure 5.5-1: Picture of the integrated biochip (inset: SEM cross section)

5.6. Conclusions:

Fabrication processes to develop the integrated microchannel and the plating molds were developed. Each individual step was developed separately and then was integrated into a single process. However, the integration process was not a straightforward translation of the individual steps. Instrumental limitation required some modification of the processes before they could be successfully integrated.

Chapter VI
Microfabrication of the Isodynamic OGMS – SU-8 Process repeatability and Troubleshooting

6.1. Reproducibility problems with SU-8 2010

Fabrication of 250 μm thick enclosed microchannels, 100 μm thick electroplating molds and their integration in a single device have been successfully demonstrated in Chapter V. The plating molds showed good compatibility with the plating solution and thick NiFe (50/50) alloys were successfully plated into the molds. The fabrication process was reproducible and three sets of molds were fabricated. These three sets of molds were utilized to develop the plating process. One of the raw materials used for developing all these samples was SU-8 2010. For the first three set of experiments, all the SU-8 2010 utilized was from the same batch. A new batch of SU-8 2010 was obtained to fabricate the forth batch of devices as the SU-8 from the previous batch was all utilized to fabricate the first three set of devices. Unfortunately, it was found that the new batch of SU-8 2010 behaved differently from the first batch of SU-8. For example, the new batch of SU-8

formed blister like features on the film during the soft baking steps, which were never encountered with the previous batch. Additionally, with the new batch of SU-8 2010 the three layer process (section 5.2.1.2) that was able to fabricate the molds without forming cracks was no longer reproducible and cracks were consistently formed during the soft baking of the ~100μm third layer. The process for the formation of the enclosed microchannels, however, was reproducible.

MicroChem is the only supplier of SU-8 and it was not possible to obtain SU-8 from the previous batch. During this time MicroChem also notified that they had made changes in the solvent that is used in the SU-8 formulation. Moreover, within a few months of these changes, MicroChem updated the general guidelines for the processing of SU-8 2000 series. The updated guideline was significantly different from the previous guidelines. For example, the previous guideline clearly mentioned that the soft bake should be carried out in two steps – pre-bake at 65C and soft-bake at 95C. Baking could be carried out either in an oven or on a hotplate. On the other hand, the updated guidelines suggested that the baking can be carried out in only one step at 95C and no pre-bake is necessary. It was also mentioned that convection ovens for baking should be avoided - a skin may form on the resist during convection oven baking. However, we did not encounter any skin formation during any of our SU-8 processes and a convection oven was an important part of our development process – particularly to process SU-8 structures on both sides of the wafers.

6.2. Troubleshooting

With the new batch of SU-8 2010 the process to obtain the electroplating molds had to be modified and redeveloped. These molds were developed using five layers of SU-8

Table 6.2-1: Process parameters for the five layer fabrication of the SU-8 molds

Layer 1	**Target**	**10 microns, SU-8 2010**
	Spin	2250 rpm, 45 sec
	EBR	300 rpm, 30sec
	Soft-bake	1 min 65C, 6 min 95C
	Cool down	5 min
	Expose	15 sec @ 15mW, Through-mask
	PEB	95C, 15 min
	Cool down	5 min
Layer 2	**Target**	**20 microns, SU-8 2010**
	Spin	1750 rpm, 45 sec
	EBR	300 rpm, 30sec
	Soft-bake	2 min 65C, 10 min 95C
	Cool down	5 min
Layer 3	**Target**	**20 microns, SU-8 2010**
	Spin	1750 rpm, 45 sec
	EBR	300 rpm, 30sec
	Soft-bake	2 min 65C, 10 min 95C
	Cool down	5 min
Layer 4	**Target**	**20 microns, SU-8 2010**
	Spin	1750 rpm, 45 sec
	EBR	300 rpm, 30sec
	Soft-bake	2 min 65C, 10 min 95C
	Cool down	5 min
Layer 5	**Target**	**20 microns, SU-8 2010**
	Spin	1750 rpm, 45 sec
	EBR	300 rpm, 30sec
	Soft-bake	2 min 65C, 10 min 95C
	Cool down	5 min
	Expose	26 sec @ 15mW, Through-mask
	PEB	95C, 30 min
	Develop	SU-8 developer, 12-15 min

2010. It was found that, reducing the thickness of the third layer to 20 μm allowed soft-baking of the films without any formation of cracks. Hence, the desired thickness of the plating mold was obtained by applying four layers of ~20 μm thick SU-8 on the ~10 μm adhesion layer. The four 20 μm thick layers were exposed and cured simultaneously and

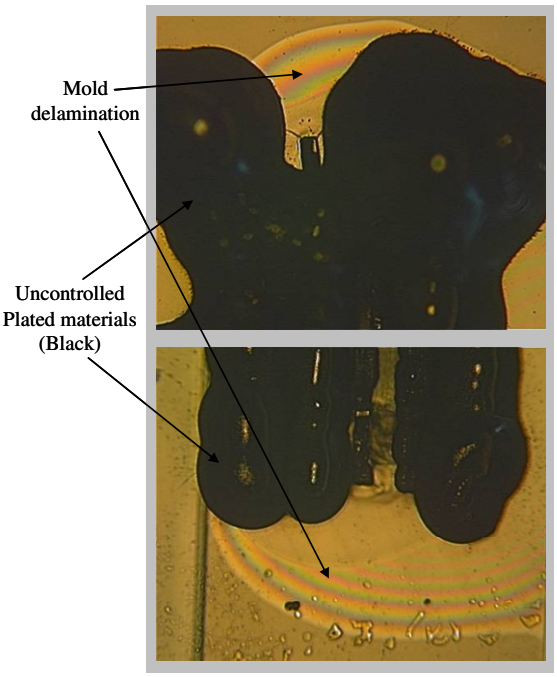

Figure 6.2-1: Optical microscope picture (5X) showing uncontrolled deposition of NiFe alloys due to delamination of the molds (five layer process) in the plating solution.

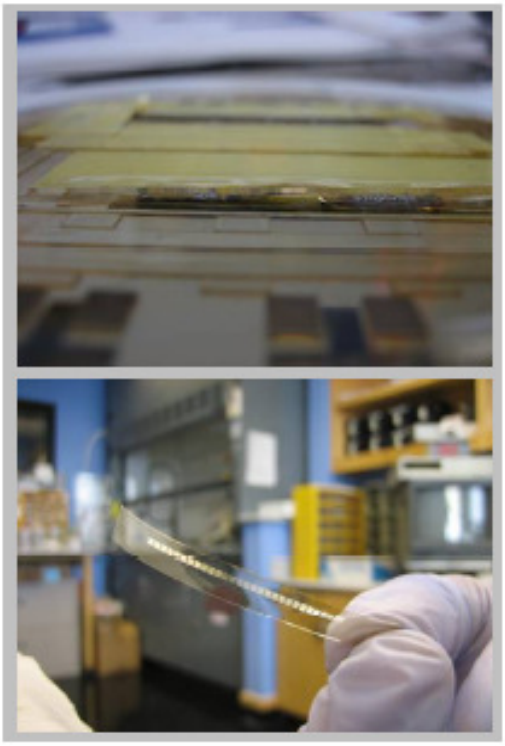

Figure 6.2-2: Pictures showing delaminated plating molds (five layer process).

all five layers were developed in a single step. The microfabrication parameters for the five layer SU-8 process are presented in Table 6.2-1.

Optical and SEM investigation of the electroplating molds that were made using the five layer process showed very good adhesion to the underlying Pyrex and Nickel layer. However, the molds failed during the electroplating process. Delamination of the molds was observed after the plating process. NiFe was plated inconsistently on the masks. Figure 6.2-1 shows an optical microscopic image of the erratic deposition of the material on and around the electroplating molds. The delamination seems to occur at the corners of different features in the mold. In some cases the mold delaminated completely (Figure 6.2-2). No chemical deterioration of the molds was observed in any of the molds during the electroplating process. This probably means that the SU-8 delamination occurred due to the mechanical/thermal reasons. The optimum temperature of the electroplating solution reported by Integran was 60C and the plating process lasts for about 1 hour, with moderate agitation. It is possible that the combination of agitation and temperature can lead to the loss of adhesion.

In order to investigate the effect of the plating conditions on the plating molds a ‘mock’ plating solution was set up at the Cleveland Clinic location. The ‘mock’ plating solution consisted of the same kind of materials (Table 6.2-2) that is used by Integran in their plating solution. However, this solution is called a ‘mock’ solution because the solution was not used to perform actual electroplating. It was just utilized to create the plating conditions with respect to agitation, pH and temperature.

Table 6.2-2: Composition of mock plating solution

Components	g/L
$NiSO_4.6H_2O$	168
$FeSO_4.7H_2O$	81
$NiCl_2.6H_2O$	135
pH	3-4

The idea was to dip the plating molds in this solution at different conditions (e.g. agitation, temperature, time etc.) and investigate the outcome of these conditions on the molds – whether the mold delaminated or not. It was found that that the five layer plating molds delaminated in the mock solution in a consistent manner. The severity of the delamination depended on the length of time it was dipped into the solution. The sample that was dipped for an hour showed greater delaminated regions than the samples that were dipped for 30 minutes. After several trials (three experiments from three different batches of fabrication), it was concluded that even with the five layer approach the new batch of SU-8 2010 was not suitable for fabricating the plating molds.

During this time, MicroChem introduced a new product - KMPR 1000 series photoresists. They also published an adhesion study where they show that this material has very good adhesion properties to Pyrex.[149]. Therefore, it was decided to investigate KMPR 1050 as the material for plating molds in our applications.

6.3. Process development with KMPR 1000 Series

KMPR is also an epoxy based negative photoresist that was introduced by MicroChem in early 2007. It is capable of forming thick microstructures for MEMS based electroplating applications. The processing steps are the same as the processing steps for SU-8. However, the processing parameters were significantly different from SU-8. Similar to SU-8, KMPR is also marketed at different viscosities to obtain a range

Table 6.3-1: Process parameters for the development of one sided KMPR mold

Layer 1	**Target**	**50 microns, KMPR 1050**
	Spin	3000 rpm, 30 sec
	EBR	300 rpm, 30sec
	Soft-bake	95C, 60 min, Bake Oven
	Cool down	5 min
Layer 2	**Target**	**50 microns, KMPR 1050**
	Spin	3000 rpm, 30 sec
	EBR	300 rpm, 30sec
	Soft-bake	95C, 60 min, Bake Oven
	Cool down	5 min
	Expose	150 sec @ 15mW
	PEB	95C, 15 min, Bake Oven
	Develop	SU-8 developer, 5 min

Table 6.3-2: Process parameters for the development of double sided KMPR mold

***Substrate* side processing**		
Layer 1	**Target**	**50 microns, KMPR 1050**
	Spin	3000 rpm, 30 sec
	EBR	300 rpm, 30sec
	Soft-bake	95C, 15 min, Bake Oven
	Cool down	5 min
Layer 2	**Target**	**50 microns, KMPR 1050**
	Spin	3000 rpm, 30 sec
	EBR	300 rpm, 30sec
	Soft-bake	95C, 40 min, Bake Oven
	Cool down	5 min
	Expose	150 sec @ 15mW
	PEB	95C, 5 min, Bake Oven
	Cool down	30 min
***Cap* side processing**		
Layer 3	**Target**	**50 microns, KMPR 1050**
	Spin	3000 rpm, 30 sec
	EBR	300 rpm, 30sec
	Soft-bake	95C, 20 min, Bake Oven
	Cool down	5 min
Layer 2	**Target**	**50 microns, KMPR 1050**
	Spin	3000 rpm, 30 sec
	EBR	300 rpm, 30sec
	Soft-bake	95C, 40 min, Bake Oven
	Cool down	5 min
	Expose	150 sec @ 15mW
	PEB	95C, 15 min, Bake Oven
	Develop	SU-8 developer, 5 min
Develop* both sides *simultaneously		
	Develop	SU-8 developer, 12-15 min

of film thicknesses. KMPR 1050 was chosen for the development of the new plating molds. The advantage of using KMPR mold was that it has excellent adhesion with Pyrex wafers[153] and therefore, no adhesion layer was required.

However, the suggested equipment for baking applications was a hotplate. Since, our objective was to use KMPR molds on both sides of the wafers, hot plates were not suitable for our application. Therefore, new process parameters were needed to be developed where the baking is carried out in a convection oven. The initial approach was to develop one sided plating molds and test them in the mock plating solution. The processing parameter for the fabrication of KMPR molds on one side of the wafer is presented in Table 6.3-1. A two layer approach was utilized to maintain thickness uniformity of the ~100 µm KMPR film. The KMPR molds showed excellent adhesion to Pyrex. Upon fabrication, the KMPR mold was dipped in the plating mold solution at 60C

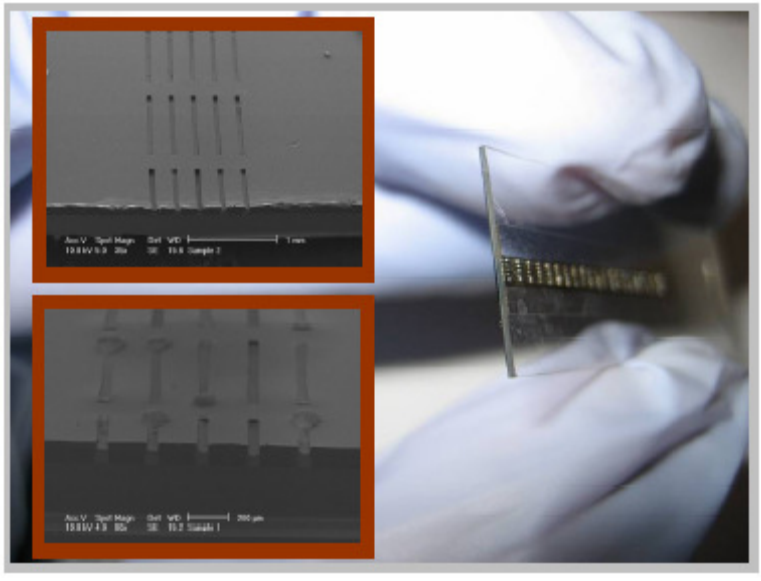

Figure 6.3-1: Picture showing a diced plated KMPR mold (inset: SEM micrographs of two diced KMPR molds with plated paterials)

for 1 hour with moderate agitation. No delamination of the Molds was observed. The molds were then sent to Integran for Plating experiments. The molds were successfully plated (at 45C) without any hint of delamination. Both the mold and the plated material showed good adhesion to the underlying Nickel and Pyrex. The plated mold was also able to withstand the wafer dicing. Figure 6.3-1 shows a picture of a diced plated mold with SEM micrographs in the inset.

Following the successful outcome of the one sided KMPR molds, a second process was developed to obtain SU-8 molds on both sides of the wafer. During the development of the double sided molds, it was observed that KMPR is sensitive to heat polymerization. If a layer of KMPR is kept at its baking temperature (100C) for ~ 4 hours, the KMPR can start to polymerize even without any exposure to light. Since the one sided KMPR molds were fabricated using a two layer process, the first layer actually experience the baking temperature for as long as 2 hours and 15 minutes. If the same process is transferred to the double sided molds, the first layer of KMPR would have to experience the baking temperature for about 4 hours and 30 minutes. With this process, when the KMPR was developed, it was found that the first layer of the KMPR began to polymerize and became a sticky layer. The sticky KMPR was not soluble in the developing solution. As a result, the fabrication process for the KMPR molds had to be optimized such that heat polymerization could be avoided. It was done by keeping the baking time for the total process less than 2 hours and 15 minutes. The optimized process is presented in Table 6.3-2.

6.4. Conclusions

Based on the excellent adhesion results from the KMPR 1050 molds, the KMPR based mold development process was integrated with SU-8 based enclosed microchannels (Process development protocols are presented in detail in Appendix B). The fabrication of the overall device up to the electroplating process was produced in a reproducible manner at the Cleveland Clinic Facility. However, the plating process developed by Integran technologies was not optimized completely. A close up of the SEM image revealed that thickness of the plated materials varied in different locations. In some areas (near the corners of the rectangular grooves) significant overplating was observed. Although frequent, the overplating was not consistent for every plating groove. The thickness was measured at different locations and was found to be around 50 μm. EDX (Energy Dispersive X-ray) analysis showed that the iron content was about 70% in the plated material. The goal of this project was to obtain 100 μm thick electrodeposited NiFe with Fe content equal to ~50%. As a result, the process for electrodeposition will have to be optimized.

However, the ability to fabricate enclosed microchannels integrated with electroplating molds that are stable in the electroplating solution is a critical part of the overall development process. Several new techniques such as (1) fabricating enclosed microchannels with selectively exposed bond layers; (2) fabricating electroplating molds with KMPR photoresists; and (3) fabricating microstructures on both sides of a wafer; were successfully developed to obtain the integrated components.

Chapter VII
Microfluidic Characterization of the OGMS channel

7.1. Introduction

Individual aspects of the overall fabrication of the five-layer isodynamic OGMS channel were addressed in the previous chapters. The enclosed microchannels were formed using a selectively exposed SU-8 bond layer, interconnects were developed using capillaries inserted from the side of the channels, and thick electroplating molds were fabricated on both sides of bonded wafers. Although it was shown that the plating molds were sufficiently strong to withstand the harsh environment of the electroplating bath for the desired plating materials (50%Ni-50% Iron), the plating process is yet to be optimized by Integran, Inc. As a result, it was not possible to obtain the completed isodynamic channel in time for inclusion in this project. Nevertheless, it was important that the microchannels are characterized for their bond qualities and flow properties. The objective of this chapter is to present the characterization of the OGMS channel for bond

quality and flow. Different sets of experiments were developed to characterize the microfabricated channels. The flow properties and magnetic separation was investigated using video microscopy and digital image analysis.

7.2. Bond Characterization

7.2.1. Bond quality

The bonded channels were tested for qualitative bond strength and sealing properties at different operating conditions. Conventional bond testing techniques such as the crack opening test or the blister test generally do not represent the operational environments of a microfluidic device[154]. Therefore, customized bond testing protocols were developed to investigate the bond characteristics. Bonded wafers were diced using a dicing saw (DAD 320, Disco Corporation, Tokyo, Japan). A successful bond was determined by the ability of the bond to withstand the dicing process where the wafers are subjected to high shear and water jets. The bonded wafers that could pass the dicing test were then investigated under Scanning Electron Microscopy (SEM) to visually inspect the bond quality (e.g. channel clogging, proper sealing around the channels, etc.).

Although qualitative, these characterization steps were sufficient to approximate normal operating conditions in our microfluidic devices. For example, the dicing test did not give any quantitative information on the bond strength. However, wafer dicing is an essential step in the fabrication of most microfluidic devices. The ability of a bond to withstand the dicing process can certainly indicate the ability of the bond to sustain mechanical stresses in most microfluidic applications. Figure 7.2-1 shows an SEM cross-section of bonded wafers that were diced across a set of ~250 μm thick microchannels.

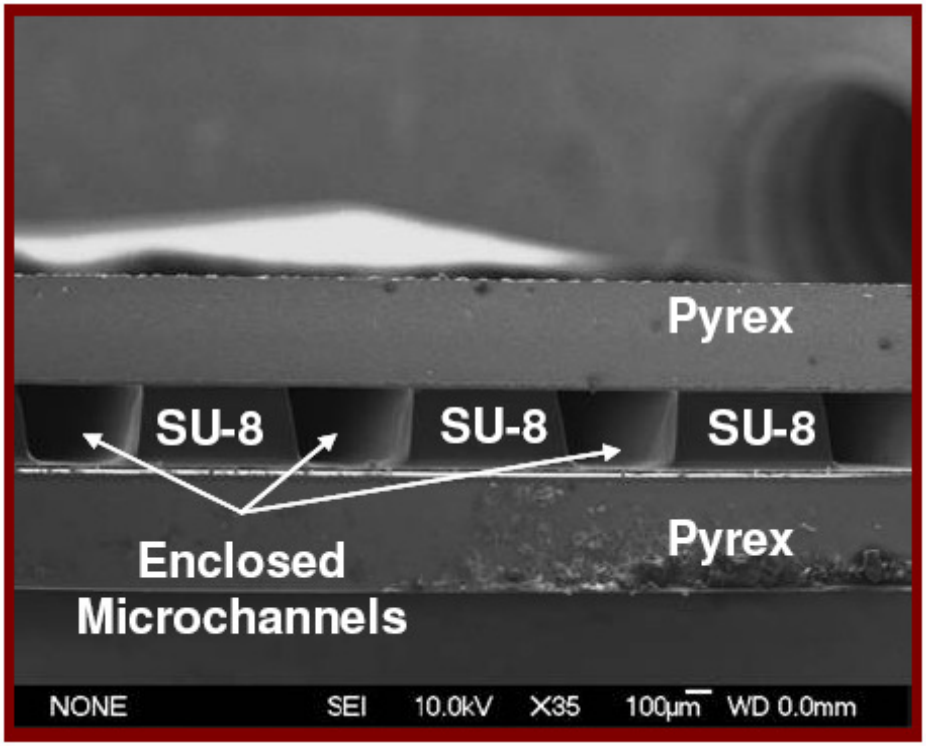

Figure 7.2-1: SEM micrograph showing cross-sections of a set of enclosed microchannels -the channels are not clogged and the wall between the channel are properly bonded to Pyrex

One important aspect of the development of microfluidic devices is to connect the microfluidic devices with macro-scale peripheral devices (e.g. syringe pumps). The microfluidic interconnection scheme presented in Chapter III provides a seamless way to connect the channels with external devices. A limitation of this method is that the channel thickness is determined by the OD of the capillary tubing used for the interconnections. The interconnections were established using (31 Gauge, Sarasota, FL, USA) MicroFil™ capillaries. The smallest OD available of these capillaries is 90 µm. However, it is not necessary that the channel thickness be limited by the OD of the capillaries. Multilayer structures can be utilized to account for smaller channels[107]. Bonding of these capillaries to the microchannels was performed using adhesives. Special attention to the selection of the adhesive was required. If the viscosity of the adhesive was too low (e.g. cyano-

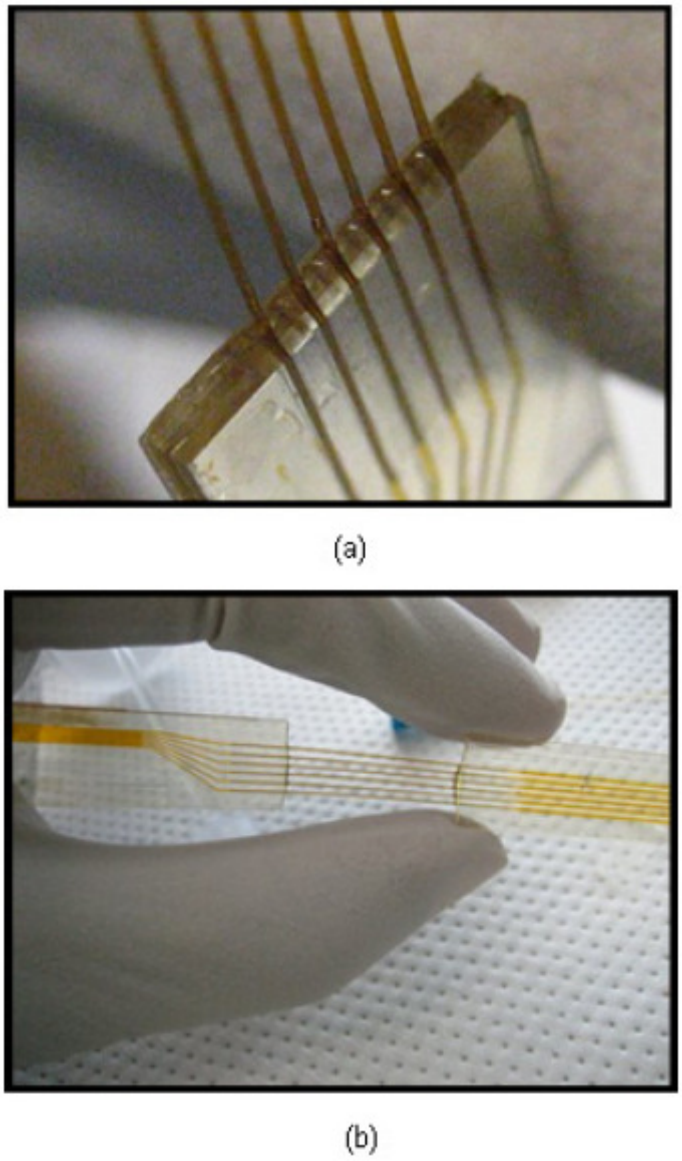

Figure 7.2-2: Pictures showing (a) Microfil™ capillaries connected to our microfluidic chip; (b) Two microfluidic chips connected by Microfil™ tubing.

acrylate based Super Glue, Loctite®, Henkel Consumer Adhesives, Avon, Ohio, USA), capillary action caused the glue to seep into the channels past the capillaries and thereby, clogging the capillaries. On the other hand, if the glue was highly viscous (e.g. common glue sticks (ethylene –vinyl acetate copolymers) used in glue guns), the adhesive was unable to enter the crevices between the capillaries and the microchannel openings, and

resulted into insufficient sealing. Loctite® Extra Time Epoxy (Loctite, Henkel Consumer Adhesives, Avon, Ohio, USA) system was found to be suitable for the proposed designs in this work. However, the choice of the adhesive can vary depending on the design (e.g. size of the crevices between the capillaries and microchannel openings) of the microchannels. Figure 7.2-2(a) shows an example of microfluidic interconnections. Since the connection is made in plane with the flow channels, dead volume is significantly reduced compared to the conventional microfluidic connections. In addition, no drilling of the wafers was required by this interconnection method. Finally, the interconnect scheme is also suitable to connect and establish flow between two or more separate microfluidic devices seamlessly (Figure 7.2-2(b)).

7.2.2. Leak testing

Upon successful packaging of the capillaries with the microfluidic channels, the wafer bonding and the bonding of the capillaries to the microchannels were tested for leakage. Two kinds of leak testing were performed. First, the diced microchannels were connected to the regulator (Prostar, Praxair, Danbury, CT, USA) of a pressurized N_2 cylinder (Praxair, Danbury, CT, USA). The maximum pressure allowed by the regulator was 100 psi. The channels, the outlets and portions of the inlet capillaries were immersed under water in a transparent water tank (CLS 1001L, Sigma-Aldrich, St. Louis, MO, USA). Gas from the pressurized tank was released into the immersed channels. The immersed chip and the inlet/outlet connections were observed for gas bubble formation. Formation of any bubble at the inlet/outlet connection or at any region of the diced channel would indicate the presence of leakage at the respective locations. Five samples

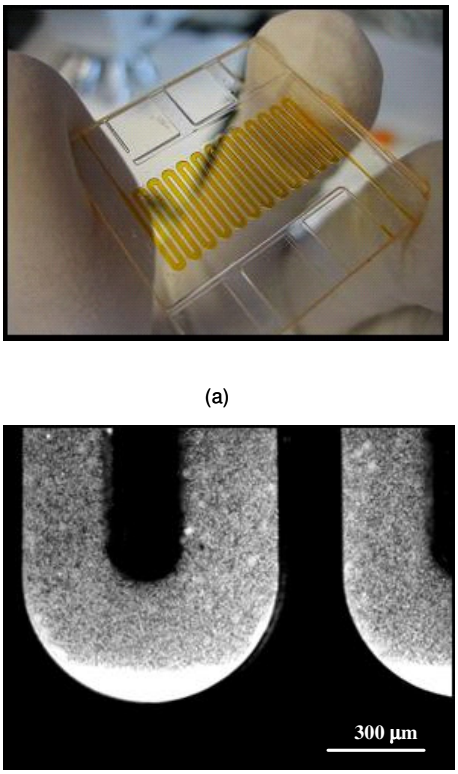

Figure 7.2-3: (a) Picture showing a bonded serpentine channel filled with a dye (Orange G); (b) Fluorescent microscope (5x) picture showing a section of the serpentine channels filled up with ~5µm particles suspended in buffer solution.

from different batchs of bonded wafers were subjected to gas pressure up to 100 psi for two hours and no bubbles were observed.

The second test determined if there was any leakage between two or more channels within the device. For this purpose, a serpentine channel network (Figure 7.2-3(a)) was designed. The serpentine channel represented a more complicated fluidic channel structure compared to the design of the OGMS channel. The purpose of designing this channel was to establish a widespread applicability of the current bonding process. The channel was filled with a dye (Orange G) or a solution of fluorescent micro-particles (~5 µm green fluorescing polymer microspheres, Duke Scientific, Palo Alto, CA). The channels were then investigated under the microscope to see if the orange dye/micro-particles are present in any section other than inside the serpentine channels. Any

presence of the dye between the channels would clearly indicate that there is leakage between different sections of the channel. Figure 7.3-2(b) shows the outcome of a properly bonded channel network where no dye/micro-particles were present in between the channels.

7.3. Open gradient magnetic separation

7.3.1. Experimental setup

Figure 7.3-1 shows a picture of the magnet assembly of the miniaturized OGMS system. The dimensions (Appendix C) of the magnetic module were sent to Dexter Magnetic Technologies, Elk Groove Village, IL, USA. A schematic diagram of the experimental setup is presented in Figure 7.3-2. The channel is attached to the magnetic manifold using tape (Scotch® Multitask Tape, 3M, St Paul, MN, USA). The objective was to capture optical images of the particles in the microfluidic channels under different flow conditions. The magnet and the microfluidic channel were taped on to an aluminum block (3”×10” ×1”) such that the separation zone of the channel is placed inside the air

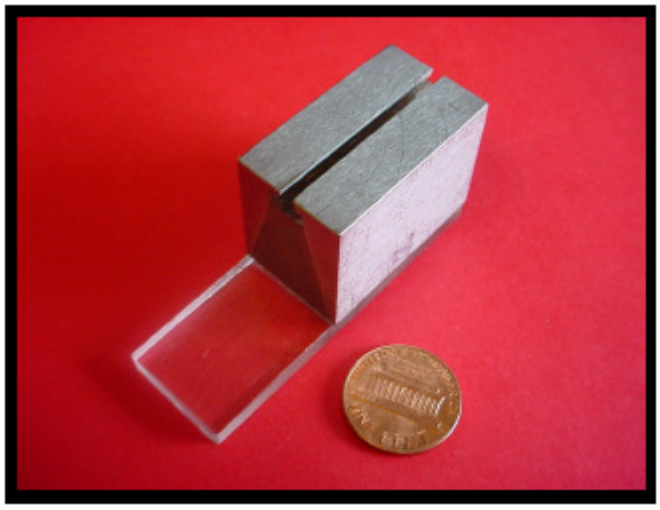

Figure 7.3-1 Photograph showing the miniaturized OGMS magnet.

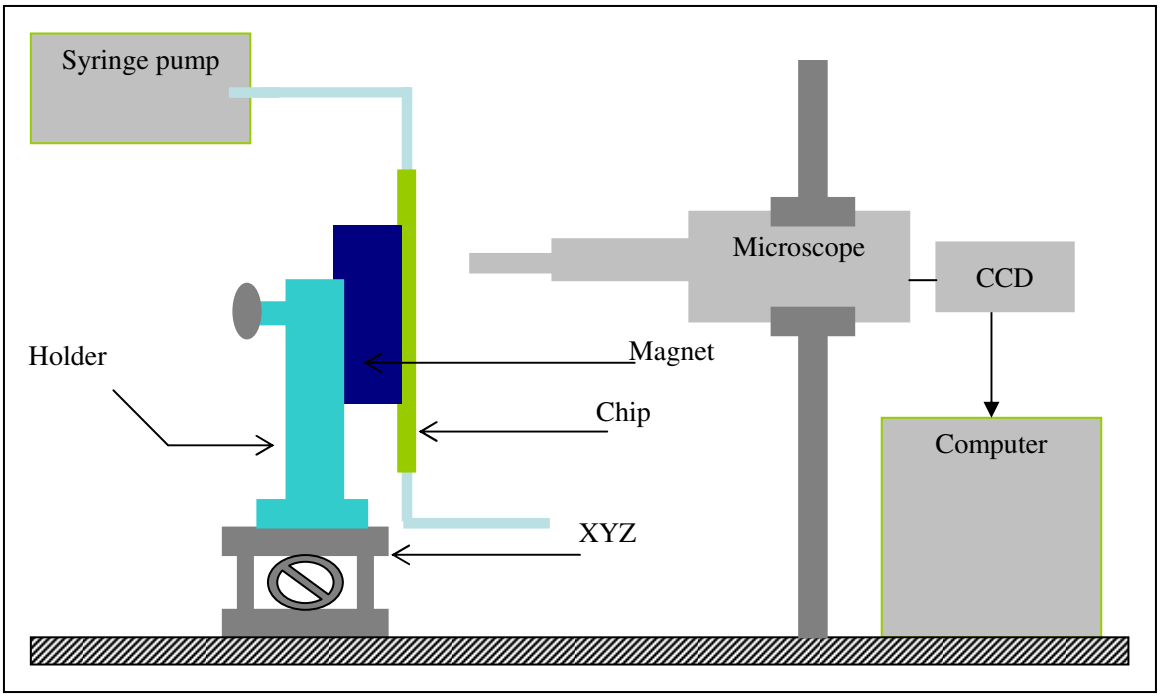

Figure 7.3-2: Schematic diagram showing the experimental setup for flow characterization

gap of the magnet. The aluminum block was placed on a translation stage (model 462-XY-SD, Newport Corp. Mountain View, CA) with the channel positioned in vertical position in order to avoid confounding effects of the gravitational sedimentation. A fluorescent microscope (model BXFM-F, Olympus America Inc, Center Valley, CA) connected to a high-sensitivity, monochrome CCD camera (Retiga EXi, QImaging Corporation, Surrey, BC, Canada) was placed horizontally with the objective facing the microchannel such that images of the flowing particles could be acquired in real time. The CCD camera was connected to a computer (Dell Optiplex GX280, 3.4 GHz Pentium 4, 1 GB RAM, Austin, TX, USA) for data acquisition. The translation stage could be adjusted in the horizontal direction for focusing the channel and in the vertical direction to investigate the flow inside the channel at different locations. The inlets of the channel

were connected to syringe pumps (model '33', Harvard Apparatus, Holliston, MA). The outlets from the channel were connected to collection test tubes.

7.3.2. Image Acquisition

Image acquisition was performed using a high speed digital video recording software (Video Savant 4.0, IO Industries, London, Ontario, Canada). Images were acquired 5-20 frames per second. Images were acquired under different microscope lighting conditions – Bright field, Dark Field and Fluorescent Field (470-490 nm). Data acquisition parameters utilized for different lighting conditions are listed in Table 7.3-1. Video files (AVI format) were compiled with the acquired images using Windows Movie Maker 5.1 (Microsoft Corporation, Redmond, USA) Video Savant was also capable of capturing single frames.

7.3.3. Particles

~5 μm green fluorescing polymer microspheres form Duke Scientific, Palo Alto, CA were utilized as the negative control samples (nonmagnetic particle). On the other hand, 6.4±0.5μm latex particles containing 0.45% (w/w) magnetite were custom ordered from Micromod Partikeltechnologie GmbH, Rostock, Germany as the positive control samples (magnetic particles). The magnetophoretic mobility distribution of these magnetic

Table 7.3-1: Image acquisition parameters

Parameters	Bright Field	Dark Field	Fluorescent Field
Exposure time (millisecond)	250	500	20000
Gain	1200	1200	700
Offset	1200	1200	400

particles was measured using Cell Tracking Velocimetry (CTV) by the Cell Separation Research Laboratory, Cleveland Clinic, Cleveland, Ohio and was found to be (7.29±2.38) × 10^{-4} mm^3/TAs based on the measurements of 486 particles. All particles were suspended in a buffer solution (0.1% FL-70 detergent (SF-105-1, Fisher Scientific, Pittsburg, PA, USA) + 0.02% NaN_3 (S2002, Sigma-Aldrich Co, St. Louis, MO, USA) in DI water) to obtain a sample concentration ~ 1×10^6 Particles/ml. The negative and positive control solutions were mixed in equal volumes to obtain the mixed sample.

7.3.4. Demonstration

Three types of tests were performed with the OGMS channel. First, the channel was tested with nonmagnetic particles (negative control). The experiments with negative control showed how the particles behave under different hydrodynamic focusing conditions. Next, a mixture of nonmagnetic and magnetic particles was utilized to show the ability of separating the magnetic fraction from the nonmagnetic fractions.

The particle samples were introduced into the OGMS channel using Inlet #2 and the carrier solution (contained only the buffer) was introduced using Inlets #1 and #3. The streams from #1 and #3 were used to focus the particle stream from #2 at a desired location of the OGMS channel. The ratios of the inlet flow rates were adjusted by trail and error such that the particles are focused along the stream line they are introduced from Inlet #2. The particle flow under different experimental conditions was observed using video microscopy over five minutes.

Figure 7.3-3 shows a flow situation, where non-magnetic particles are introduced via inlet #2 at 50 µl/min (average velocity through the OGMS channel 0.0017 mm/sec)

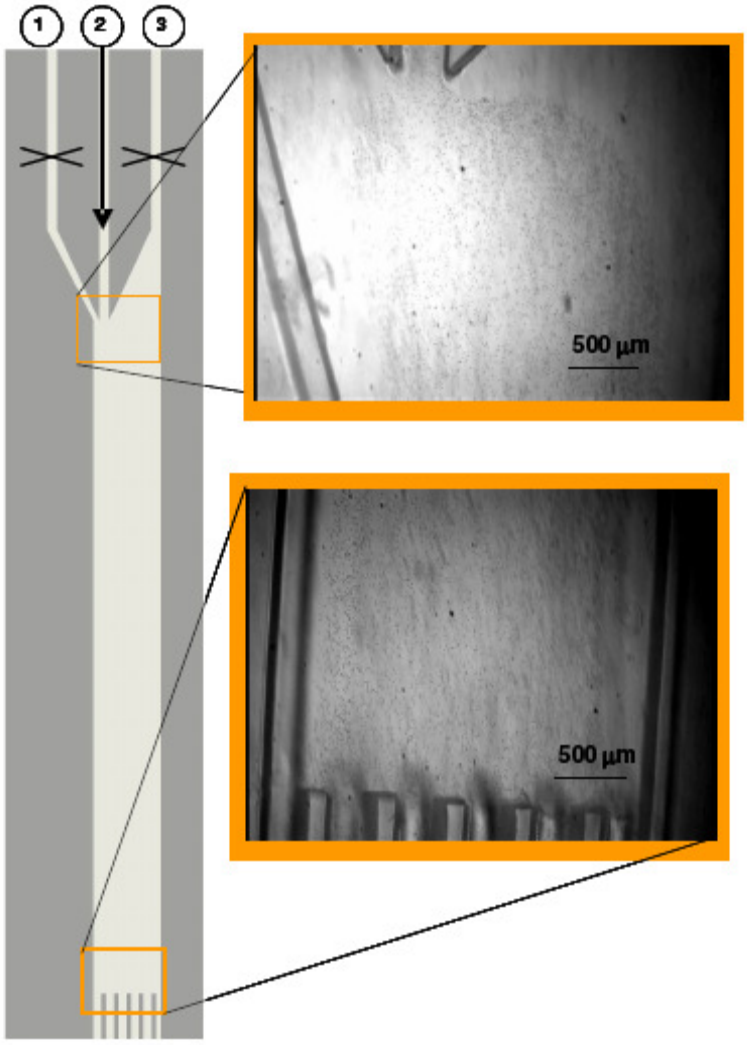

Figure 7.3-3: Optical microscope (5x) picture showing the flow of non magnetic particles inside the OGMS channel with no flows at inlet #1 and #3 - particles are spread through out the cross-section of the channel and come out through all the outlets

without any flow in other inlets. The particles spread through out the cross-section of the channel as the flow become fully developed. At the outlet of the OGMS channel the particles exit through all the six outlets. When flow is introduced at a similar total flow rats through inlets #1 and #3 along with the feed stream at the inlet #2, the feed stream no longer spreads throughout the channel cross-section. Rather, hydrodynamic focusing was obtained of the particles and the width/location of the feed stream could be controlled by

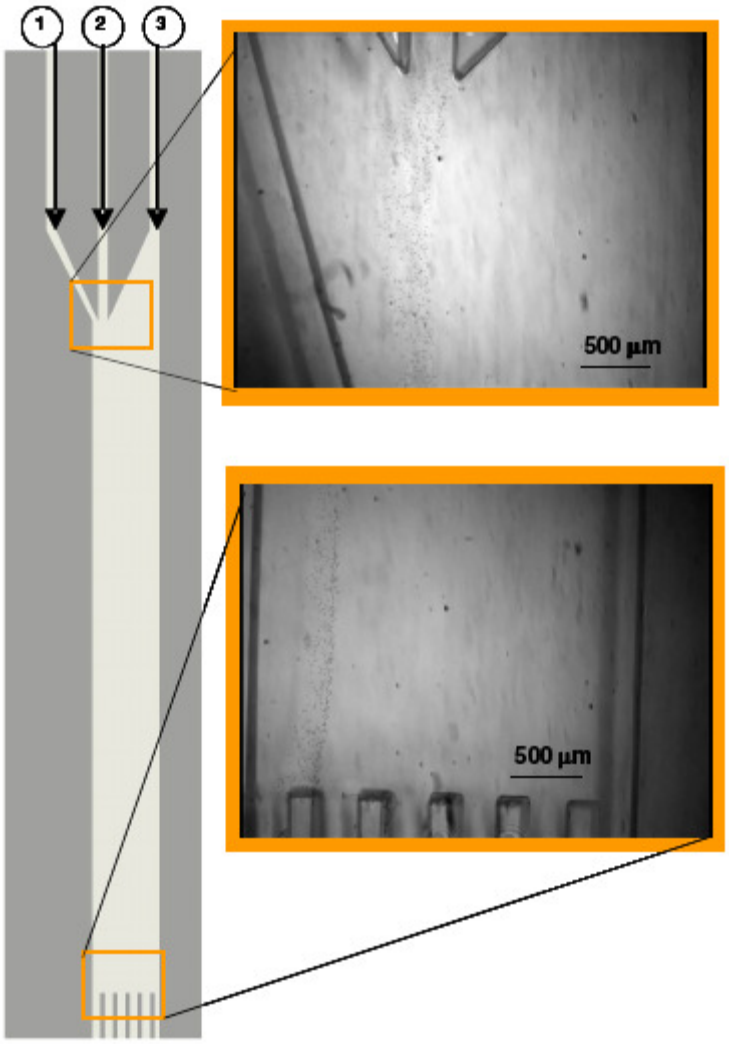

Figure 7.3-4: Optical microscope (5x) picture showing the flow of hydrodynamically focused non magnetic particles inside the OGMS channel

controlling the flow rate ratio in different inlets. A ratio of 7:5:40 (total flow rate of 52 µl/min) showed that the particle stream could be focused right along the stream line it was introduced. Investigation over time showed that the focused stream was very stable and there was no observed diffusive movement of the particles as expected. Based on the size of the particles the diffusion coefficient (based on the Stokes-Einstein equation[155], 3.05×10^{-14} cm^2/sec) for the particles was very small and therefore, the diffusive effect

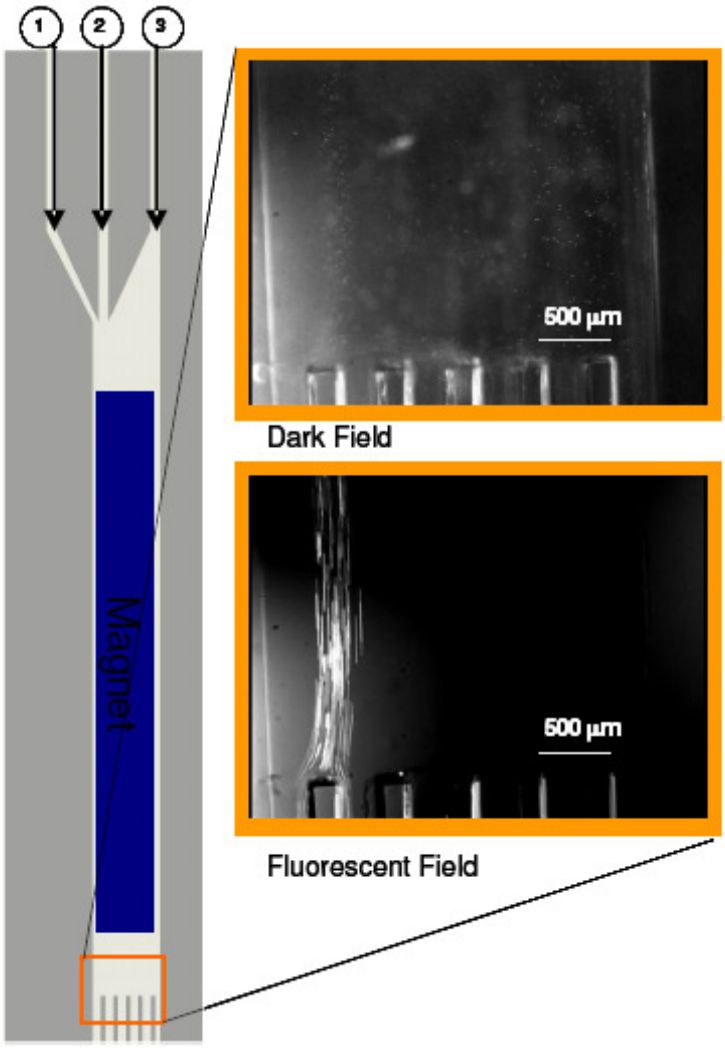

Figure 7.3-5: Optical microscope (5x) picture showing the flow of a mixture of non magnetic (fluorescent) and magnetic particles inside the OGMS channel.

was negligible. Figure 7.3-4 shows a picture of focused particles inside the OGMS channel.

The same experiment was repeated with mixed samples (50:50 magnetic and non-magnetic/fluorescent particles). In order to be able to distinguish the magnetic particles from the nonmagnetic particles, images were taken at both dark field and at fluorescent field. At dark field all the particles were visible. However, under fluorescent lighting only the non magnetic fraction was visible. Images of the outlets of the OGMS channel for the

mixed samples under both the lighting conditions are presented in Figure 7.3-5. It can be clearly seen that the fluorescent (non-magnetic) particles are not deflected from the hydrodynamically focused stream and are all exiting the separation channel at outlet numbers #1 and #2 (Figure 7.3-5).

The distance of the particles from an axis can be determined using the Image Pro software. In this case the axis can be aligned with one end of the channel (channel wall next to outlet #1). From a dark field image of the mixed sample, the distances of all the visible cells from the axis can be measured in terms of microns and these can be plotted in a histogram. The bin size (range) can be set such that each range can represent one outlet. In this case the splitters are 140 μm thick. Based on the images, it was apparent that the particles that were traveling in the direction of the splitters got divided into two streams – one goes into the left of the splitter and the other goes into the right of the splitter. Therefore, while determining the bin size, the locations of the splitters were taken into considerations and the width of the splitters was divided into two and was allotted to the two outlets on each side of that splitters.

The image analysis was carried out based on 200 consecutive images acquired at 10 frames/sec. Since the images were taken consecutively over a period of time, the same particle is counted repeatedly if all 200 images were utilized for the counting. Careful observation of the images showed that it was not possible to track the particles along their full paths because they go in and out of focus. This can happen due to the alignment of the channel with the microscope objective. The average distance was measured from a total of all 200 images, set of every 10^{th} image, set of every 15^{th} image and set of every

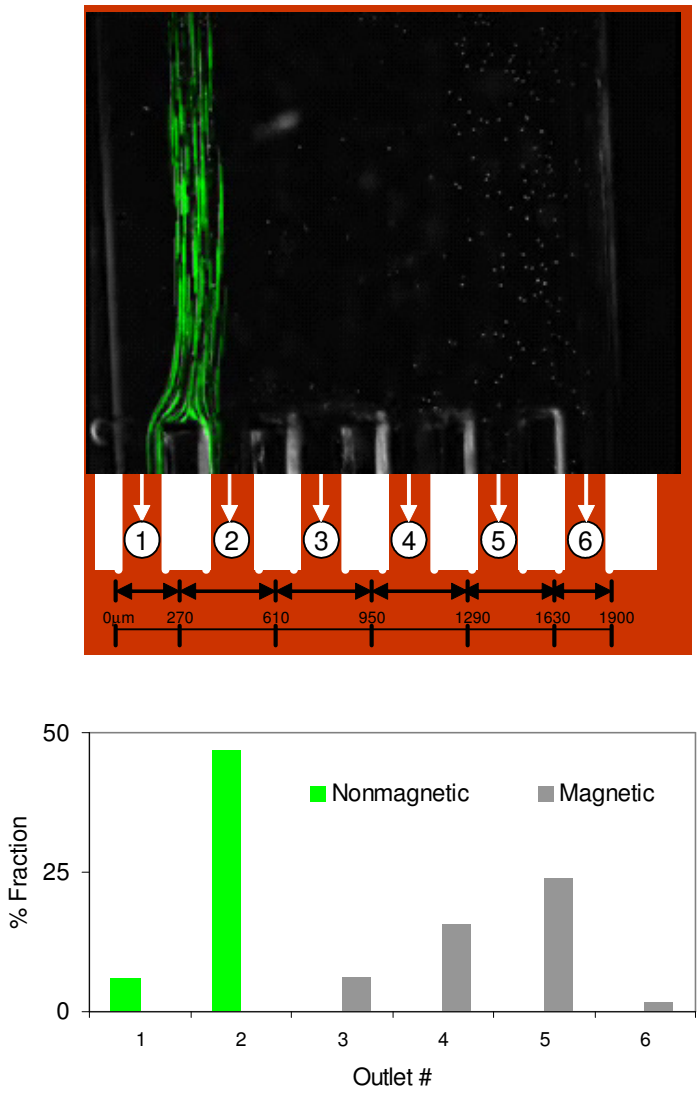

Figure 7.3-6: Superimposed optical microscope (5x) picture of dark field and fluorescent field images showing all fluorescent particles stay in the hydrodynamically focused stream and the graph showing the fractions of particles distributed among the outlets.

25th image. It was found that the average distances traveled by the particles was not statistically (ANOVA, $\alpha = 0.05$) different for each data set. For our calculation we investigated the set of every 10th image. The average velocity inside the chamber was ~1.75 mm/sec. The field of view (image size) was approximately 1.75 mm. Therefore, it can be assumed that analysis of every 10th image will not count the same particle more than once.

Based on the fluorescent and dark field images, it was apparent that all particles beyond outlet 2 were magnetic particles. To further validate this assumption the ratio of particles over outlets #1 - #2 to #3 - #6 were calculated from the image analysis and was found to be 47:53. The magnetic and non magnetic particles were introduced at ~50:50 mixtures. This shows that the ratio of particles calculated from the images are similar to the ratio of particles in the samples, as expected.

Figure 7.3-6 shows a histogram of the distribution of particles in the OGMS channel. Similar experiments were carried out by Schneider et al. using a macro scale isodynamic OGMS[25]. They processed few ml of samples and collected the fractionated particles to count the number of particles in each outlet. In their experiments, non magnetic particles were hydrodynamically focused along outlet #2 at the inlet, and therefore are not expected to be found beyond outlet #2. They also measured their magnetic properties to find the fraction of magnetic and non magnetic particles in their outlets. Non magnetic particles were observed in outlets #2- #5 along with magnetic particles.

On the other hand, the experimental set up for the microfluidic OGMS utilized a microscope to visualize and record real time separation events to investigate the quality of separation. Non magnetic (fluorescent) particles were only present in outlets #1 and #2. Therefore, the separation mode as shown in Figure 7.3-6 is a significant improvement from the macro scale device. Furthermore, the extent of separation reported in this thesis is more compelling since the microfluidic set up had direct access to observing particle motion inside the channel.

The expected deflection was also estimated using equation (23) where it was found that the particles should be deflected by 820 μm -1620 μm (based on the average

magnetophoretic mobility of particles and a average $\left|\nabla \boldsymbol{B^2}\right|$ = 0.35 T^2/mm). The deflections calculated from the images were between 610 – 1900 microns. Due to the assumptions made in the derivation of equation (23) such as that $\left|\nabla \boldsymbol{B^2}\right|$ is constant throughout the cross-section of the channel, the calculated deflection cannot reflect the actual conditions for the OGMS system. The $\left|\nabla \boldsymbol{B^2}\right|$ is not constant everywhere and drops rapidly at ~ 1700 μm along the direction of the deflection in the current system. Nevertheless, these preliminary data indicate that the microfluidic OGMS is capable of separating binary mixtures of magnetic and non magnetic particles better than the macro-scale OGMS.

7.4. Conclusions

It is shown that the bonding process developed in this work was produced enclosed microchannels that are suitable for microfluidic applications. Several customized tests were developed to verify the leakage-free microchannel network. An unconventional microfluidic interconnection scheme was also developed and verified for microfluidic applications. Finally, the channels and the microfluidic interconnections were utilized to successfully demonstrate Open Gradient Magnetic Separation in a microfluidic platform. Qualitative measurements of the deflected particles from the experiments were similar to the estimated particle deflections.

Chapter VIII
Development of a Multistage Bio-ferrograph

8.1. Introduction

In a conventional OGMS, fractionates are collected in collection chambers. The particle counts in the collection chambers are then determined by using a Coulter counter and the magnetic properties of the particles are measured by Cell Tracking Velocimetry (CTV)[25] In some cases, the cells are also tagged with fluorescent particles (sandwich immunoassay) so that they can be further analyzed using flow cytometry[156-158]. In order to perform all these post fractionation measurements significant volume (on the order of a few ml) of the samples has to be processed. One limitation that was anticipated due to the miniaturization of the macro scale OGMS was that this conventional approach of analyzing fractionates would no longer be possible. In a microfluidic platform the total volume of samples to be processed is generally very little (less than a milliliter). Due to the low volume processed in a microfluidic OGMS, the fractionate volume becomes

insufficient for the conventional particle analysis tools such as the Coulter counter or the CTV.

The objective of this chapter is to present the development of an alternate method to analyze fractionates for particle counts and their magnetic properties. A secondary unit is proposed that can be integrated with the OGMS system to measure the particle count in different fractionated outlets. A bio-ferrograph (as discussed in Chapter II) was designed that was suitably small to allow conjugation with the OGMS system. The ultimate objective was to connect a multi-channel multistage bio-ferrograph with all the outlets from the OGMS system. With this combination, the fractionated magnetic components (cells or particles) will be guided to flow through the bio-ferrograph and be trapped on designated locations. The trapped cells/particles could then be counted under optical microscopy. One limitation of the bio-ferrograph is that the deposition efficiency has been reported to be in the order of 20-60% in spite of the high gradients[34]. This is due to limitations in the existing bio-ferrograph design. First the bio-ferrograph utilizes only one magnet to trap the cells. Increasing the number of the magnets can improve the capture efficiencies of these devices. Secondly, the bio-ferrograph deposits cells on a glass slide. An enclosed flow channel is formed with a special removable manifold placing on top of the glass slide[34]) to form a controlled flow environment. However, the channel has to be drained and the manifold has to be removed before the slide can be investigated under the microscope. The draining processes leads to a gas-liquid interface passing over the deposited band of cells/particles. The gas-liquid interface can remove portions of the deposited cells from the surface of the glass slides. Utilization of enclosed microchannels and modification of the deposition protocol (e.g. keeping the microchannel primed with

the sample solution during optical investigation) can avoid the effect of a gas-liquid interface on the deposited cells and thereby, should reveal the true capture efficiency.

In this work, miniaturized permanent magnets were designed that can provide magnetic gradients comparable to a conventional bio-ferrograph. Four optimized magnets in series were utilized to improve the total capture efficiencies. The hypothesis was that the increased number of magnetic deposition zones would increase the total capture efficiency. Microfabrication techniques developed in Chapter V were utilized to fabricate enclosed microchannels that were placed on top of the magnet. Magnetic deposition experiments were carried out using magnetic particles and magnetically labeled cells. The magnetic deposition and flow characteristics were investigated using video microscopy and digital image processing. Although the multistage design was primarily developed to increase the capture efficiency of cells, it was also found that it may be possible to trap cells according to their magnetic susceptibilities on different zones. Experimental data showing the evidence of trapping magnetically labeled cells based on their magnetic susceptibilities will also be presented.

8.2. Multistage bio-ferrograph – Materials and methods

8.2.1. Device design

The force imparted on a particle/cell inside a magnetic filed is directly proportional to the magnetic energy density gradient[11]. Generally, design of a ferrograph is composed of a thin flow channel pressed against the interpolar gap of a permanent magnet circuit. In this case, the design consisted of a microfabricated enclosed channel that would be placed

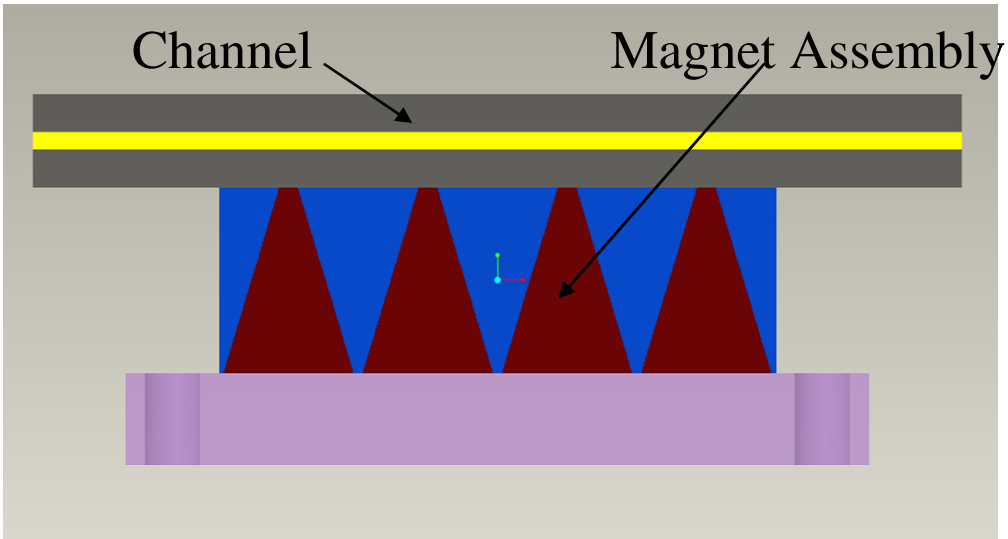

Figure 8.2-1: Schematic diagram showing the multistage bio-ferrograph

on top of a magnetic manifold (Figure 8.2-1). The magnetic manifold was composed of four trapezoidal permanent magnets (NdFeB) placed in series. The magnets were adjoined with low carbon steel to obtain the final manifold. The smaller of the two

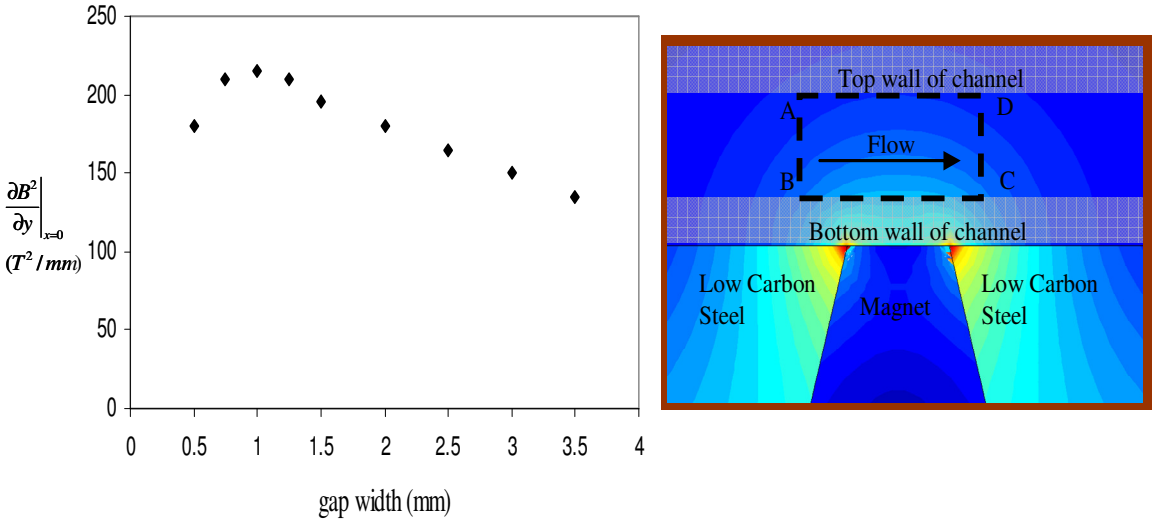

Figure 8.2-2: Graph showing the mean magnetic energy density gradient at the area ABCD (inset) for different interpolar gap widths.

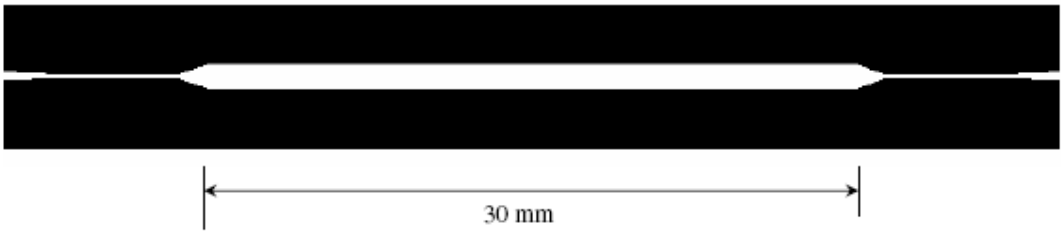

Figure 8.2-3: Graph showing the mean magnetic energy density gradient at the area ABCD (inset) for different interpolar gap widths.

parallel arms of each trapezoid defined the interpolar gaps. The thickness of the channel wall was an important parameter as it defines the distance of the magnetic deposition zones from the surface of the magnet's inter-polar gap. Based on the microfabrication processes developed in Chapter V, the thickness of the channel wall was set to 400 μm. 2D magnetostatic simulation software (MAGNETO 5.1, Integrated Engineering Software, Manitoba, Canada) was utilized to optimize the length of the inter-polar gap so that the magnetic force is maximum inside the channel. The height of the magnet was set to 10 mm while the base of the magnet was set to 6 mm. The depth of the flow channel was 250 μm. The interpolar gap width was varied to obtain the maximum mean magnetic energy density gradient in the area ABCD (Figure 8.2-2), which corresponds to the height of the channel and a width of 5mm centered on the interpolar gap. A 5mm zone was chosen under the assumption that cells will be magnetically deposited within this location for each magnet. The gap width that gave the maximum mean gradient was 1.0 mm (Figure 8.2-2).

The four units of the magnet were placed in series with alternating polarity to ensure maximum utilization of the magnetic field. The magnetic design optimization was carried out in collaboration with Lee Moore at the Cell Separations Research Laboratory, Cleveland Clinic, Cleveland Ohio (~50% contribution).

Figure 8.2-3 shows a schematic layout of the deposition channel. The channels were 30 mm long and 250 μm thick. Channels of two different widths (1.0 mm and 0.5 mm) were fabricated. Most experiments were carried out using the 0.1 mm wide channel. The channels were fabricated using the wafer bonding technique presented in Chapter V.

8.2.2. Magnetic particles and cells

6.4±0.5μm latex particles containing 0.45% (w/w) magnetite were custom ordered from Micromod Partikeltechnologie GmbH, Rostock, Germany. The magnetophoretic mobility distribution of these magnetic particles was measured using Cell Tracking Velocimetry (CTV)[77] by the Cell Separation Research Laboratory, Cleveland Clinic, Cleveland, Ohio and was found to be $(7.29\pm2.38) \times 10^{-4}$ mm^3/TAs based on the measurements of 486 particles. The particles were suspended in a buffer solution (0.1% FL-70 detergent (SF-105-1, Fisher Scientific, Pittsburg, PA, USA) + 0.02% NaN_3 (S2002, Sigma-Aldrich Co, St. Louis, MO, USA) in DI water) to obtain a sample concentration ~ 1×10^6 Particles/ml.

The leukemia-derived Jurkat cell-line was chosen as the model cell system to investigate magnetic deposition. The cells were cultured in RPMI – 1640 media (#30-2001, ATCC, Manassas, VA) supplemented with 10% Fetal Bovine Serum (FBS) (#26140-079, Invitrogen Corp. Carlsbad, CA) 292 μg/ml L-glutamine (#523-100 Cleveland clinic store room, Cleveland, Cleveland, Ohio), 50 μg/ml penicillin and 50 μg/ml streptomycin (Culture condition: 37°C, 80% humidity and 5% CO_2). Predetermined quantities of cells were washed from the culture media by centrifugation at 390g, 4°C for 10 minutes, discarding the supernatant and suspending the pellets in a buffer solution. The buffer solution was composed of 2mM EDTA (#10,631-3, Sigma-

Aldrich, St. Louis, MO) and 0.5% Bovine Serum Albumin (BSA) in Phosphate Buffer Solution (PBS) (degassed under absolute pressure of 0.16 atm and continuous stirring for 30 minutes). The washing step was repeated once more to minimize left over culture media solutions. The cells were labeled with both magnetic nanoparticles and fluorescent labels using a two step sandwich immunoassay. The sandwich immunoassay allows the cells to be tagged with both fluorescent and magnetic labels. It has been shown that for the selected cell labeling conditions, the fluorescent intensities of the tagged cells are proportional to their magnetophoretic mobilities[25]. Therefore, measurement of the fluorescent intensities of the tagged cells would provide a relative measurement of the magnetic susceptibilities of the cells.

The cells suspended in the buffer solution were first centrifuged and then mixed with primary antibody, anti-CD45-PE (Caltag Laboratories, Burlington, CA) at a concentration of 16μl/10^6 cells. The mixture was incubated for 30 minutes at 4^{o}C. Following incubation, the cells were washed to remove any excess primary antibody. The pellets were then mixed and incubated with the secondary antibody, anti-PE-MACS^{TM}(Milteny Biotech Inc., Auburn, CA) in the same concentration as the primary antibody for 15 minutes at 4^{o}C. The unbound antibodies were finally removed by another washing step and suspending in the buffer solution.

The magnetophoretic mobility distribution for the labeled cell sample was measured using CTV (Cell Tracking Velocimetry)[77] by the Cell Separations Research Laboratory at the Cleveland Clinic, Cleveland, Ohio and was found to be (5.25±1.90) × 10^{-4} mm^3/TAs based on the measurement of 1539 particles.

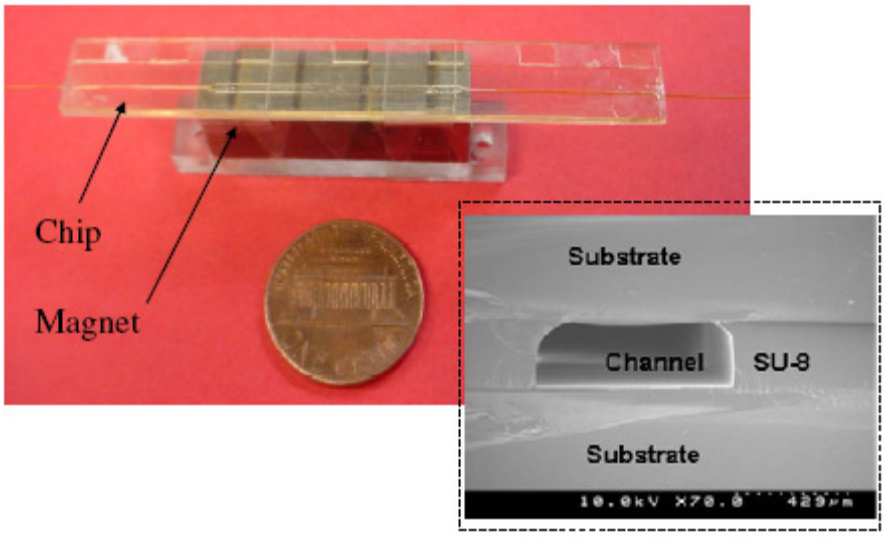

Figure 8.2-4: Picture showing the microchannel and magnet assembly (inset: SEM cross-section of the microchannel)

8.2.3. Experimental setup

Figure 8.2-4 shows a picture of the magnet/channel assembly of the multistage bio-ferrograph. The dimensions (Appendix D) of the magnetic module were sent to Dexter Magnetic Technologies, Elk Groove Village, IL, USA. A schematic diagram of the experimental setup is presented in Figure 8.2-5. The experimental setup used to perform the magnetic deposition experiments was similar to the one used for the OGMS experiments (Chapter VII). The OGMS channel and the magnet was replaced by the multistage bio-ferrograph magnet and the microfluidic channel. The channel was attached to the magnetic manifold using scotch tape. The channel/magnet assembly was then taped onto an aluminum block (3"×10" ×1"). The aluminum block was placed on a translation stage with the channel positioned in vertical position in order to avoid confounding effects of the gravitational sedimentation on the magnetic cell deposition. The inlet of the channel was connected to the syringe pump. The outlet from the channel was connected

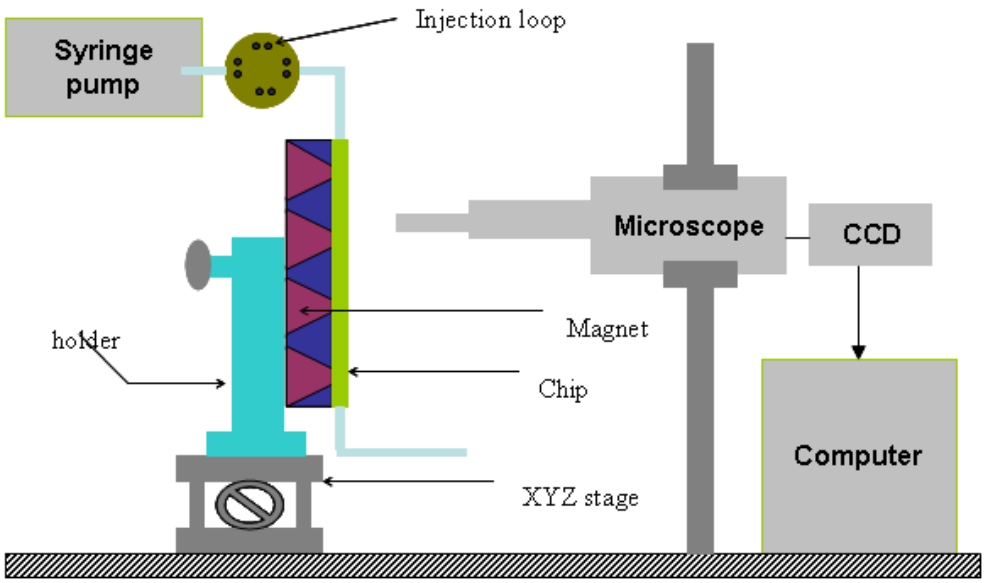

Figure 8.2-5: Schematic diagram showing the experimental setup for the multistage bio-ferrograph.

to a collection test tube. A 6-way analytical injection valve (Rheodyne model 7725, Rohnert Park, CA) with an injection loop of 100µL was connected between the channel and the syringe pump. Optical image acquisition was performed according to the method described in Chapter VII.

8.2.4. Magnetic particles deposition

50 µL of samples at different concentrations (e.g. 1×10^6 particles/ml and 1×10^5 particles/ml) were injected into the injection loop and were passed through the bio-ferrograph channel (1 mm wide) at 10 µl/min using the syringe pump. After all the sample was passed through the bio-ferrograph, images of all the deposition zones were captured using the microscope camera. The deposition zones were selected by focusing the microscope on the top of the surface of the magnetic unit. The permanent magnet material had a darker appearance compared to the low carbon steel and was easily visible through the transparent channels. The xyz stage was utilized to move the magnet/channel

assembly horizontally to change the focusing planes and vertically to locate the position of the inter-polar gaps. Once a gap is located, the assembly was moved horizontally to focus on the bottom surface of the flow channel where the particles were deposited. In order to ensure that all the deposited particles near the interpolar gap is imaged, images were taken up to 1 mm before the interpolar gap, on the interpolar gap and 1 mm after the interpolar gap. The number of deposited particles was calculated manually from the images, assuming that the particles were deposited in a single layer and individual particles could be identified. In some case, the particles were clumped in such a fashion that it was difficult to identify individual particles. The total area of the agglomerated particles was therefore divided by the area of an individual particle to obtain an approximate number of particles in the deposited aggregate. The capture efficiency was calculated by dividing the number of deposited particles by the total number of particles introduced into the system. The total number of particles introduced into the system was calculated by multiplying the injected volume with the sample concentration. Experiments at each concentration were repeated six times.

The capture efficiency was also measured for different flow rates (10 μl/min – 200 μl/min). The concentration of the sample for the different flow rates study was reduced to 1×10^4 particles/ml to avoid clumps of particles being deposited on the deposition zones and to simplify the manual counting of deposited cells. Experiments at each flow rate were repeated three times.

8.2.5. Cell deposition

1×10^5 labeled cells/ml samples were introduced at 10 μl/min into the bio-ferrograph channel (1 mm wide). The cells were introduced directly, bypassing the loop. The loop

had caused the cells to aggregate inside the loop resulting in agglomerated cells being introduced into the channel. Images of the deposited cell were captured under two lighting conditions: bright field and fluorescent field. These images were utilized to measure the fluorescent intensity of each deposited cells using digital image processing.

8.2.6. Digital image processing

A customized macro in a commercial digital image processing software (Image Pro Plus, v6.1, Media Cybernetics, Silver Spring, MD) was developed by Amit Vasanji (Musculoskeletal Imaging Core, Cleveland Clinic, Cleveland, Ohio) to measure the average fluorescent intensity of the cells deposited on each zone. The macro consisted of the following steps: (1) A region of interest (ROI) was selected within the of bright-field images; (2) the appearance of cells in acquired images was enhanced by using edge-emphasizing, large spectral filters; (3) the resultant images were median-filtered to remove noise and thresholded by intensity and area (to remove debris and large objects not consistent with cell size). This step generated binary masks of segmented cells. (4) A watershed filter was applied to split apart the cells that are connected; (5) a product of cell masks set and corresponding cell fluorescence images set was used to produce images that consisted of fluorescently labeled cells that were isolated from background and nonspecific fluorescence (replaced with black pixels), but still retained their original intensity levels; (6) using an intensity range of 0-255 gray-levels, the mean intensity for each cell in the masked images was calculated and exported to Microsoft Excel (Microsoft Office Professional 2003, Microsoft Corporation, Redmond, USA) spreadsheet. Objects not consistent with average cell size were removed via size/shape exclusion prior to intensity measurement. From uploading the image to Image Pro to

obtaining the spreadsheet data took less than a minute for each image. Image Pro Plus also features a cell counting module which could count the deposited cells automatically based on the filtered and thresholded images.

8.3. Multistage bio-ferrograph – Results and discussions

8.3.1. Effect of gas liquid interface

Video microscopy allowed capturing the deposition process in real time. We observed particle accumulation only in the areas close to the locations defined by the interpolar gaps of the magnets. When the same experiment was performed with non magnetic particles, no significant accumulation of particles was observed (not shown). The effect of a gas-liquid interface on the deposited particles was investigated using video microscopy in a 500 μm wide channel. A large bubble was introduced into the channel

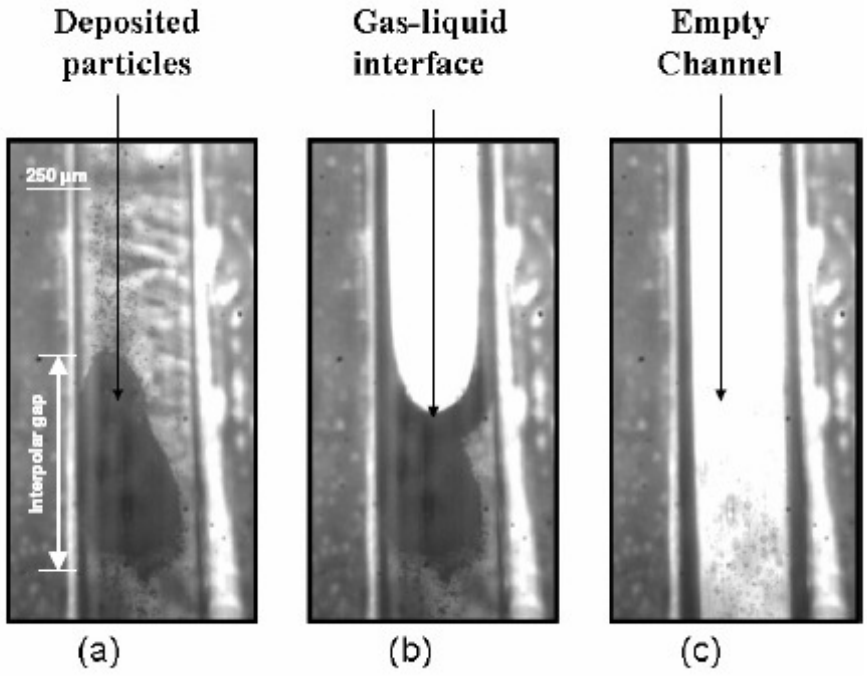

Figure 8.3-1: Microscope pictures (5x) showing (a) before, (b) during and (c) after the gas-liquid interface crosses the deposition zone (500 μm wide channel).

after some particle accumulation on the deposition zones. Figure 8.3-1 shows pictures of a deposition zone before, at the time and after the gas-liquid interface crosses the deposition zone. It can be seen that a large portion of the particles were swept off by the gas-liquid interface. This shows that conventional approach used in bio-ferrography, which allows the gas liquid interface to pass through the deposition zone, can introduce additional forces that cause the loss of deposited particles. The alternate method suggested in this work was to use an enclosed microchannel for the deposition. In the present work, images were taken right after the deposition experiments without removing the magnet/channel assembly from the experimental set up. However, in a more practical setting, where a horizontal microscope or a sophisticated xyz stage may not be available, one could run the experiment with the channel/magnet assembly in the vertical position and then use valves to close the inlet and the outlet of the channel keeping the channel primed with the buffer solution. In this manner, the channel/magnet assembly can be transported to a microscope for acquiring images.

8.3.2. Capture Efficiencies

Particles were found to deposit only at or near the four inter- polar gaps (deposition zones). The total capture efficiencies for the magnetic particles were 84.6±9% and 79.8±6% at 10 μl/min with 1×10^6 particles/ml and 1×10^5 particles/ml, respectively. However, based on the experiments at different flow rates it was found that increasing the flow rate reduced the capture efficiency. Figure 8.3-2 shows the effect of different flow rates on the capture efficiencies for a sample of 1×10^4 particles/ml.

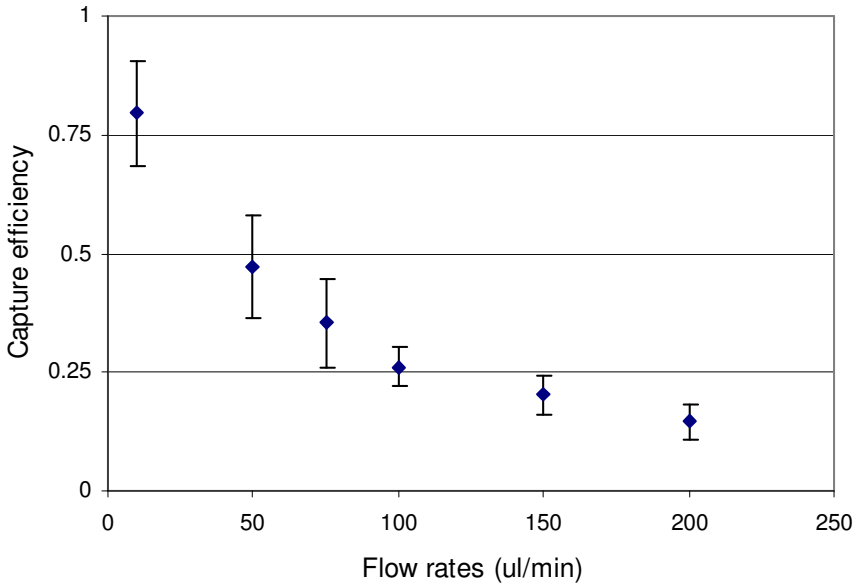

Figure 8.3-2: Graphs showing capture efficiencies of the multistage bio-ferrograph at different flow rates for a magnetic particle sample concentration of 1×10^4 particles/ml.

Table 8.3-1: Comparison between automated cell counting by digital image processing with manual cell counting

Image #	Manual count	Image Pro Count	% error
1	1432	1487	3.84
2	260	286	10
3	174	180	3.45
4	881	875	0.68
5	1450	1503	3.66

Capture efficiency of the device was further investigated using labeled cells. The ability of the automated cell counting from an image of the deposited cells was first verified by using five different images with varied numbers (Table 8.3-1) of deposited cells. The number of cells was counted manually and by Image Pro to compare the accuracy of the automated cell counting protocol. It was found that the automated cell counting protocol was able to count the number of deposited cells within ±10% of the manual counts. For the capture efficiency calculation with cells, the total number of cells introduced was kept less than ~5000 per experiment. Introducing a higher number of labeled cells seemed to result in the cells being deposited in multiple layers, which made it difficult to get a true count of total number of deposited cells. Since no injection loop was used for the cell deposition studies, the experiments were designed to run for 10 minutes at 10 μl/min flow rates with a sample concentration of 1×10^5 cells/ml. The total number of cells introduced into the system was calculated by adding the total number of cells deposited and the total number of cells that escape through the outlet. Deposited cells were calculated from the images of the deposition zones and the total number of cells that escaped from the system was calculated by counting the cells that passed through the outlet. Images of the outlet of the channel were captured at a rate of 10 frames/sec during the course of the experiments. The images were then investigated in a video format to manually count the total number of cells passing through the outlet. Based on three experiments the capture ratio for cells was found to be 99.46±0.26%.

The total number of cells captured in each individual zone was also determined from the image analysis and are plotted in Figure 8.3-3. As the cells are introduced into the channel they are distributed randomly throughout the cross-section of the channel

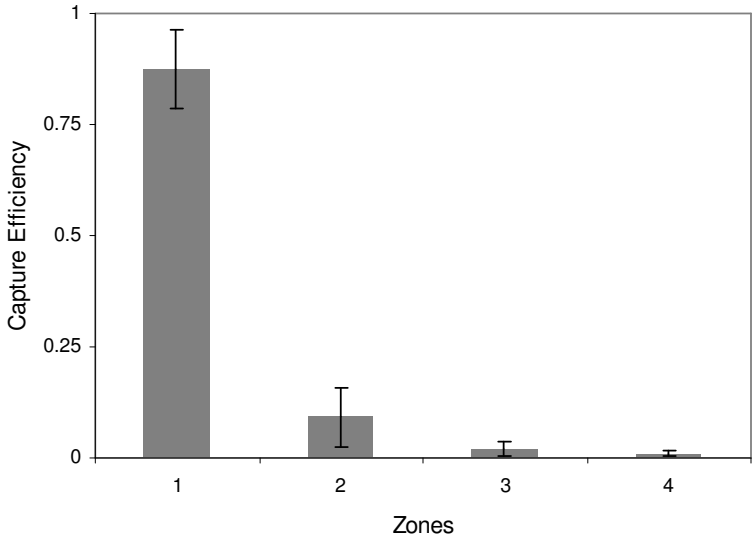

Figure 8.3-3: Graphs showing capture efficiencies on different zones at 10 µl/min flow rate for labeled Jurkat cells (1×10^5 particles/ml).

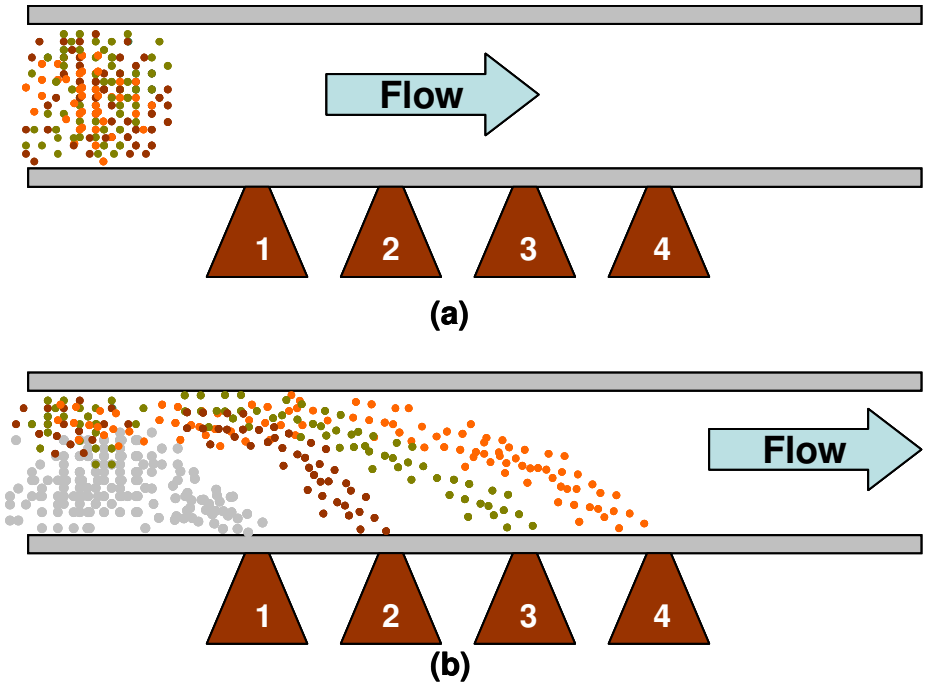

Figure 8.3-4: Schematic diagram showing the mechanism of cell/particle deposition in the multistage bio-ferrograph. The grey dots represent cells that are trapped in the first zone irrespective of their magnetic properties. Brown, Green and Orange color dots represent magnetic particles/cells of different magnetic properties (Brown>Green>Orange).

(Figure 8.3-4(a)). However, when they reach the first zone, the cells are attracted by the magnetic force. As a result, based on the location of the cells relative to their distance from the bottom surface of the channel and their velocity, a portion of the cells will be dragged all the way to the bottom surface and get deposited. At 10 μl/min flow rate we observe that 87.4±9% of the total deposited cells are trapped in the first zone. This indicates that cells that are not trapped are the ones that are located at the furthest distance from the bottom surface. In this manner, cells that escape the first zone will be located close to the top surface of the channel as they approach the next zone. Consequently, cells are no longer distributed throughout the channel cross-section as they approach zone 2, rather they are focused near the top surface of the channel (Figure 8.3-4(b)). So, the mechanism of trapping the cells on zones beyond zone 1 will be different from the trapping mechanism on the zone 1. In zone 1, the cells are trapped irrespective of their magnetic properties. On the other hand, for zone 2, 3 and 4, cells will be deposited based on their trajectories with an initial location near the top surface of the channel. Cells that are more magnetic will travel faster across along the depth of the channel and will reach the deposition zone 2, whereas the cells that are less magnetic will reach deposition zones that are further down the stream. This effect was further investigated by measuring the fluorescent intensities of the deposited cells on zones 2-4.

8.3.3. Fluorescent Image Analysis

The Image Pro Plus macro described in section 8.2.6 was utilized to measure the pixel intensities of the cells in zones 2-4. Figure 8.3-5 shows an example of an image at different stages of the image processing steps. Cells become more identifiable after

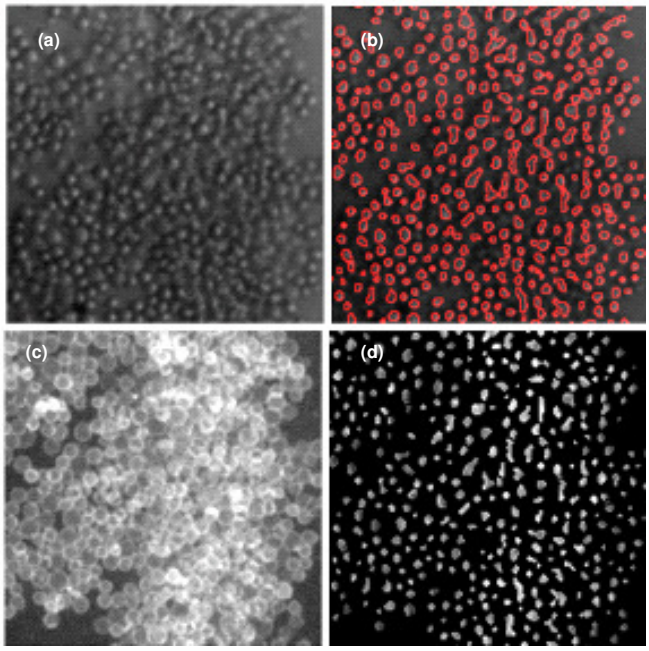

Figure 8.3-5: Microphotographs showing different stages of the digital image processing: (a) original bright field image; (b) segmented image after applying filter; (c) original fluorescent image; (d) after the background is isolated.

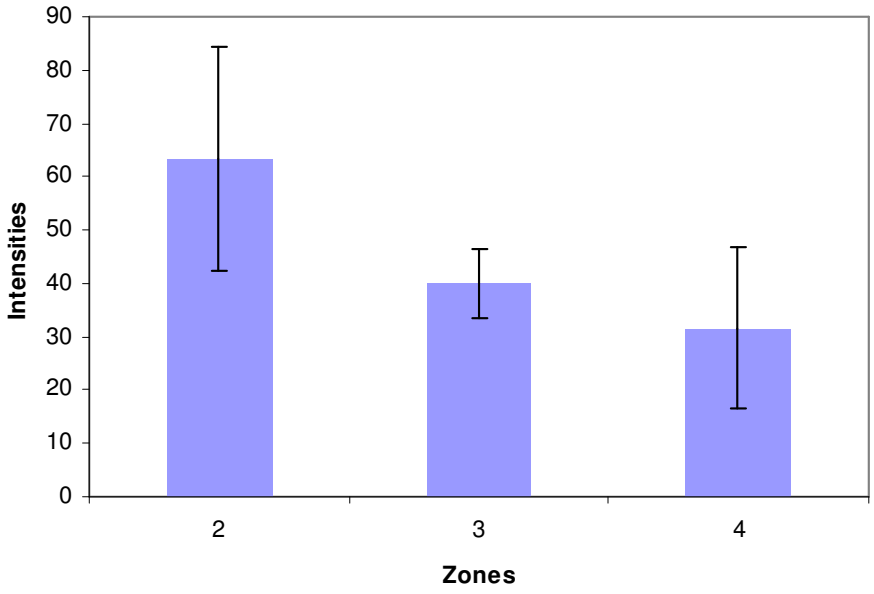

Figure 8.3-6: Graphs showing Fluorescence intensities of deposited cells on zones 2-4 at 10 µl/min flow rate for labeled Jurkat cells (1×10^5 particles/ml).

applying the macro. The total number of cells deposited in each zone and their average pixel intensities are tabulated in Table 8.3-2 for each individual experiment. Statistical analysis of the data can be carried out for each experiment ('within' the experiment) to investigate whether the average pixel intensities are significantly smaller than the average pixel intensities of the preceding zones. Each experiment was investigated using one-way Analysis of Varience (ANOVA) for a significance level of 0.05 (α) using Minitab statistical software (version 15, Minitab Inc, State College, PA, USA). Pair wise comparison was performed based on Tukey's family error rate and the decisions on significance with in each experiment is presented in Table 8.3-3. In all three experiments, the differences in mean intensities between zone 2 and zone 4 were found to be significant.

Since the experiments were repeated three times, statistical analysis 'between' experiments could provide information with respect to repeatability of the experiments. For this, the average intensities and the standard deviations of cells based on all the experiments for each of the zones were calculated and plotted in Figure 8.3-6. One-way ANOVA 'between' the experiments for each pair of zones suggested that the differences in means were not significant. Nevertheless, the Figure 8.3-2 suggests that the average fluorescent intensities of these zones follow a decreasing trend with the increasing zone numbers. Since fluorescence intensity depends linearly on the magnetic properties of the cells, the decreasing trend suggested that the cells are being deposited according to their magnetic properties. The current design was not optimized to trap cells according to their magnetic properties. However, preliminary data suggest that it may be possible to deposit cells based on their magnetic properties with the help of a multistage bio-ferrograph. The

Table 8.3-2: Cell count and mean fluorescent intensities in zones 2-4 for different experiments with 1×10^5 labeled Jurkat cells/ml at 10 μl/min flow rate.

Zones	Exp#1		Exp#2		Exp#3	
	Cell Count	Mean Intensities	Cell Count	Mean Intensities	Cell Count	Mean Intensities
2	179	50.9±24.0	189	51.3±21.8	1018	87.6±28.1
3	28	46.8±16.9	42	34.0±20.2	237	38.4±23.4
4	21	23.2±18.9	25	22.5±19.1	96	49.1±22.2

Table 8.3-3: Decisions on significance between fluorescent intensities of zones with in each experiment based on Tuckey's test

	p-value		
Between Zones	**Exp#1**	**Exp#2**	**Exp#3**
2&3	Not significant	Significant	Significant
3&4	Significant	Significant	Not significant
2&4	Significant	Significant	Significant

design of the inlet flow may be modified such that all cells are introduced (e.g. via hydrodynamic focusing) near the top wall of the channel (Figure 8.3-7). An optimized design of the channel and magnet arrangement may lead to a standalone diagnostic device that can separate and deposit cells on designated locations based on their magnetic step.

8.4. Conclusions

A miniaturized multistage bio-ferrograph was developed. The bio-ferrograph composed of a miniaturized magnetic unit that consisted of four magnetic deposition zones in series and enclosed microchannel. Experimental protocols were developed to capture magnetic

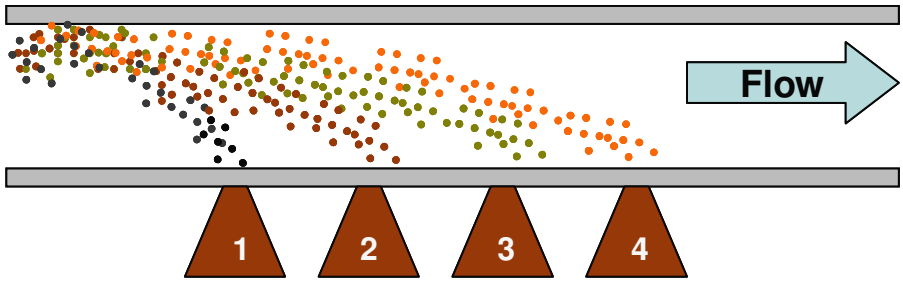

Figure 8.4-1: Schematic diagram showing the mechanism of cell/particle deposition in the multistage bio-ferrograph with focused introduction of particles/cells at the inlet. (Black>Brown>Green>Orange).

particles/cells inside the enclosed microchannels and analyze deposited particles/cells using digital image processing. Although the multistage design was adopted to increase capture efficiency, it was found that magnetic particles/cells may be deposited based on their magnetic properties.

Chapter IX
Conclusions and Recommendations

9.1. Summary

The objective of this dissertation was to present the early stage developments of a portable system for rapid isolation and detection of rare cells in a biologically relevant sample. The isolation principal was based on immunomagnetic cell separation. The first step of the work involved designing a microfluidic/magnetic platform for isodynamic open gradient magnetic separation. The goal was to design a miniaturized microfluidic/magnetic system that was able to generate and isodynamic magnetic field gradient inside the microfluidic channel and was suitable for easy installation of the channels inside the magnetic field. The design utilized a set of planar pole-pieces embedded on the channel walls and a small external permanent magnetic circuit. It was found that the embedded pole-pieces not only helped to maintain nearly constant magnetic field gradient inside the flow channel but also allowed sufficient scope for installing the channels without rigorous alignments. The uniqueness of the design lies within the construction and the shape of the embedded pole-pieces. The embedded pole-

pieces were designed to have planar geometries so that they could be fabricated using microfabrication techniques. The design also showed that it is possible to obtain an isodynamic magnetic field over a considerable region to perform open gradient magnetic cell separation.

However, there were certain limitations with the design. The minimum saturation magnetization and thickness of the materials used for the embedded pole-pieces had to be 1.5 T and 100 μm, respectively. Materials having such a combination of magnetic properties and thickness are not common in microfabrication technologies. Moreover, the design also involved microstructures that are very thick and occupied a large area (e.g. 250 μm thick, 30 mm long channels). SU-8, an epoxy based negative photoresist, was chosen for its ability to fabricate thick microstructures using simple microfabrication techniques. Pyrex was chosen as the transparent substrate. The difficulty of using SU-8 with Pyrex substrates is that, adhesion of SU-8 is poor. A highly cross-linked thin layer of SU-8 was utilized to improve adhesion of SU-8 to Pyrex. The next challenge was to obtain enclosed microchannels with SU-8 as the bonding layer. Common SU-8 based wafer bonding techniques are sensitive to thickness variation of the SU-8 structural film. A new process was developed that was not very sensitive to the thickness variation of the structural layer and was able to perform wafer bonding with structural film thickness variation of ±15 μm. The bonding was also suitable for fabrication of large area (~ 600 mm^2) devices.

Another challenge for the proposed device was the development of the embedded discrete pole-pieces – 100 μm thick materials with 1.5 T saturation magnetization is not common in MEMS applications. Electrodeposition is the most common approach to

fabricate such materials. An electrodeposition process is generally composed of two major steps – fabrication of plating molds and electroplating steps. The plating molds were prepared as a part of the current development and then were sent to Integran Technologies for developing the plating process. In order to develop the thick plating molds on Pyrex substrates SU-8 was first investigated. A multilayer fabrication process was developed that improved the adhesion of SU-8 to Pyrex for mold formation. However, the adhesion was not strong enough to withstand the harsh plating environment. For this reason, a new polymer KMPR was considered. The process developed with KMPR was stable and showed good adhesion characteristics after preliminary plating experiments. Plating experiments were able to plate ~50 μm thick 70% Fe and 30% Ni alloy on the plating molds. This process will have to be optimized by Intergran Technologies to obtain 100 μm thick alloys of 50% Fe and 50% Ni alloy.

The integration of the plating molds and the enclosed microchannels was an essential component for the development of the completed device. The unique challenge for the integration was that the plating molds will have to be developed on both sides of bonded wafers. The process to integrate the plating molds and the enclosed microchannels was also developed as a part of the present dissertation.

Different experimental techniques were developed to investigate several aspects of the development process. A new microfluidic interconnection scheme was developed that did not require any drill holes and reduced dead volumes at the interconnections. The scheme also allowed seamless connection between multiple microfluidic devices. The interconnections and the wafer bonding techniques were tested for leakages using custom designed experiment that was practical and close to actual application conditions.

Although a completed device with electroplated embedded pole-pieces was not achieved, the experimental setup to validate magnetic separation was developed. The objective was to test the microfluidic channels without the discrete pole-pieces for flow optimization, hydrodynamic focusing and magnetic separation. These experiments provided preliminary data with respect to designing future experiments with the final devices.

A second magnetic sorter was also developed that could be conjugated with the microfluidic open gradient magnetic sorter so that that fractionates from the first device could be captured and analyzed for counting the fractionated cells. The second device was designed based on a conventional bio-ferrograph. The miniaturized bio-ferrograph was designed to be small so that it could be a part of the portable system. The magnet was designed to have four magnetic deposition zones. Each unit of magnet was designed to have a magnetic energy density gradient comparable to the large scale bio-ferrographs. The multistage bio-ferrograph was characterized for flow and capture ratio of particles/cells. The particle capture ratio was as high as 80-85% at a flow rate of 10 µl/min. It was further shown that it might be possible to deposit magnetically labeled cells based on their magnetic properties. The analysis of deposited cells (e.g. counting) was performed using digital image processing.

9.2. Original Contributions

The current dissertation contributes several new techniques in the area of magnetic separation and microfabrication. The key innovations are –

- A planar magnetic design for isodynamic Open Gradient Magnetic Separation

- Several research groups are developing magnetic cell sorters based on magnetic deflections[26,58,60,66,159,160] in a microfluidic platform. However, none of these approaches utilizes an isodynamic magnetic field. Utilization of an isodynamic magnetic field can provide a more controlled separation environment than non isodynamic magnetic fields. The embedded discrete pole-piece approach in our design can allow further benefits such as adapting a slide in/out cartridge application. This is also an important improvement from its macro-scale counterpart and makes the current design more suitable for developing easy to use portable magnetic sorters for point of care diagnostic applications.

- An adhesive wafer bonding technique utilizing a selectively exposed SU-8 bonding layer
  - The utilization of a selectively exposed SU-8 bonding layer to obtain wafer bonding and an enclosed microchannel offers several benefits over other SU-8 based bonding techniques described in the literature[103,106,107,134-136,143,147]. For example, most SU-8 based bonding techniques are sensitive to the thickness uniformity of the structural layer[147]. Our method was not so sensitive to the thickness non-uniformity (up to ±15 microns) of the structural layer and was able to form enclosed microchannels without clogging the channels. The bonding was also suitable for fabricating large area (~500 mm^2) devices. In addition to fabrication of microchannels for Lab-on-a-chip applications, this technique can find further use in other areas such as MEMS packaging.
- A fabrication method to obtain thick electroplating molds on Pyrex substrates

- Pyrex is a common substrate in Lab-on-a-chip applications. The ability to fabricate thick (~100 microns) electroplating molds on Pyrex can enable fabricating different kinds of MEMS components such as more powerful electromagnets[161] and microcoils[122-124] (e.g. for microfluidic Nuclear Magnetic Resonance systems).The microfabrication process developed in this work is therefore an important milestone for the future development of different kinds of MEMS and Lab-on-a-chip components.

- A fabrication method to fabricate epoxy based polymer (SU-8 & KMPR) structures on both sides of a wafer
  - Fabricating thick SU-8 or KMPR films on both sides of a bonded wafer is not common in microfabrication. While the need for such fabrication processes would be very specific to the kind of development at hand (such as the device in this work), it can be utilized to fabricate 3D microfabricated structures for different engineering applications.
- A microfluidic interconnection scheme that does not require drill-holes, reduces dead volume and can establish seamless interconnection between two or more microfluidic devices.
- A miniaturized Open Gradient Magnetic Separation system
  - The open gradient magnetic separation system developed in this work utilizes a microfluidic platform and a small portable magnet. It was shown that the microfluidic platform was able to separate a binary mixture of magnetic and nonmagnetic particles. When compared with its macro-scale counterpart, improved separation characteristics were observed in the preliminary separation experiments.

Table 9.2-1 Total flow rates in different microfluidic magnetic sorters

Reference	Technique	Type of Samples	Total Flow Rate
Blankenstein et. al.[58]	Magnetic deflection	Magnetic particles (1-10 μm)	10-100 μl/min
Pamme et. al.[26]	Magnetic deflection	Dynabeads (2.8 -4.5 μm)	<10 μl/min
Xia et. al.[159]	Magnetic deflection	Microbeads (1.6 μm) and E-coli	<10 μl/min
Han et. al.[66]	Magnetic deflection	Red blood cells	No flow
Inglis et. al.[60]	Magnetic deflection	Labeled Leucocytes	240 μm/sec in a 15 μm thick channel; total flow rate not reported
Berger et. al.[160]	Magnetic deflection	Blood	Insufficient data with respect to magnetic separation

Several other continuous flow cell sorters based on magnetic deflection have been reported in the literature[26,58,60,66,159,160]. A direct comparison of these sorters with our device may not be possible due to the differences in the design of experiments reported in the various publications. For example, the deflection of particles/cells depends on the type of magnetic particles/cells utilized in the respective devices. Since, our development was directed towards rare cell isolation and detection, one parameter that could be globally compared with these other published works is the total flow rate in the device. In order to account for statistically significant 'rare cells', it is necessary to process large samples sizes (e.g. several ml of blood for cancer diagnostics[8]). Generally, microfluidic devices are designed to operate with very small sample sizes (few micro liters).

Table 9.2-1 shows the flow rates utilized in different continuous flow magnetic cell sorters reported in the literature. Our device was operated at a total flow rate of 50 μl/min. The only comparable device (with respect to flow rate) was the device

developed by Blankenstein et.al. Then again, the total flow rate is also dependent on the type of samples utilized for demonstration of separation. In our case, we utilize custom magnetic particles, the iron content of which was controlled to obtain magnetophoretic mobilities that are comparable to cells labeled with superparamagnetic nanoparticles.

- A miniaturized multistage bio-ferrograph
  - Single stage tabletop bioferrographs have reported capture efficiencies of labeled cells as high as 60%[31]. We report capture efficiencies of cells as high as >99% by utilizing the multistage bio-ferrograph. This is a significant improvement from the conventional bio-ferrographs. However, the flow rate was only ~10 μl/min, which may not be very suitable for rare cell detection applications. On the other hand, the design of the bio-ferrograph is very simple and can be easily extended to obtain a multiplexed system to increase the overall throughput.

9.3. Limitations and recommendations

In this work, the development of two prototypes for magnetic cell sorting for medical diagnostics is presented. This work sets the stage for numerous further investigations. The two devices have been tested individually to demonstrate their ability to separate magnetic cells/particles. From a fabrication point of view, the fabrication of a complete isodynamic OGMS is not completed. All major fabrication steps have been completed except the development of the electroplated materials. The electroplating process development was assigned to Integran Technologies Inc. and they have shown promising preliminary data. However, the plating process will have to be optimized to obtain the desired material properties (thickness and composition). In addition to plating

process parameters (e.g. temperature), the optimization process may involve modifying the design of the plating molds and the seed layer. Continued collaboration with Integran Technology Inc. will be a key to the final development of the isodynamic OGMS chip.

The two microfluidic platforms, the OGMS and the multistage bio-ferrograph, were developed with the intention of their utilization in series. The concentration of rare cells in a relevant biological sample can be very low (e.g. number of Tumor cells can range from 10-150 per ml of sample of blood) and therefore, the total volume of samples to be processed can be as large as 10 ml. Microfluidic devices are not generally designed to handle large fluid samples. However, the OGMS system is a continuous flow system which makes it eligible to process a large amount of sample. Hence the OGMS could be utilized as a cell pre-concentration unit. The multistage Bio-ferrograph can then be connected to the outlets of the OGMS for trapping the targeted cells. The microfluidic interconnection scheme developed in this work has shown that it is possible to connect the two types of channels in these devices with minimal flow interruption. Consequently, a set of experiments will have to be designed where the two systems are tested in series.

All the experiments carried out in this work used particles or model cell systems with concentrations ranging from 10^4/ml to 10^6/ml. Since rare cells occur in actual samples at a much lower concentration, further experiments will have to be designed that investigate cells at a much lower concentrations. Biological samples such as pure blood can be spiked with magnetically tagged cells at a very low concentration (e.g. 10-100/ml) to imitate a more realistic situation. Investigation of the ability of these current devices to detect the magnetically labeled cells in such samples would provide valuable information regarding their applicability for a practical hand held diagnostic system.

While the systems were designed such that the OGMS separates cells based on their magnetic properties and the multistage Bio-ferrograph traps the fractionated cells, preliminary data from the multistage Bio-ferrograph characterization showed that it might be possible to trap cells based on their magnetic properties in the same device. However, the initial design of the multistage Bio-ferrograph was not optimized to perform deposition of cells based on their magnetic properties. Therefore, further design and experiments should be carried out to optimize the multistage Bio-ferrograph to establish the device as a new generation of magnetic deposition system that can be utilized to separate multiple targeted cells in a single operation.

Another opportunity for the future with the current devices is to incorporate digital image processing tools to quantify the separation. It has already been shown that automated cell counting of the deposited cells and measurement of the fluorescent intensities of the cells can be carried out using digital image processing. Digital image processing is a powerful tool that can find further application in the current systems. For example, the number of cells going into the different outlets of the OGMS system can be counted using digital image processing. The ability to count the cells in a flow would require optimized algorithms that account for the velocity of the cells inside the channels, frame acquisition rate and the focal depth of the microscope objectives. The flow arrangement may have to be modified (e.g. incorporate 2D particle focusing) so that the particles stay within the planes of the focal depths of the microscope objective such that all the particles are in focus during image acquisition. Nevertheless, these modifications will provide excellent opportunities to obtain a complete system that is able to separate and count rare cells in a flowing solution.

Bibliography

[1] P. J. Campbell, S. Aurelius, G. Blowes et al., "Decrease in CD4 lymphocyte counts with rest; implications for the monitoring of HIV infection," International Journal of STD and AIDS **8** (7), 423-426 (1997).

[2] Jose G. Moreno, M. Craig Miller, Steve Gross et al., "Circulating tumor cells predict survival in patients with metastatic prostate cancer," Urology **65** (4), 713-718 (2005).

[3] L. M. Yu, P. J. Easterbrook, and T. Marshall, "Relationship between CD4 count and CD4% in HIV-infected people," International Journal of Epidemiology **26** (6), 1367-1372 (1997).

[4] L. Zhu, W. T. Y. Loo, and L. W. C. Chow, "Circulating tumor cells in patients with breast cancer: possible predictor of micro-metastasis in bone marrow but not in sentinel lymph nodes," Biomedicine & Pharmacotherapy **59**, S355-S358 (2005).

[5] Stefan Sleijfer, Jan-Willem Gratama, Anieta M. Sieuwerts et al., "Circulating tumour cell detection on its way to routine diagnostic implementation?" European Journal of Cancer **43** (18), 2645-2650 (2007).

[6] Patrizia Paterlini-Brechot and Naoual Linda Benali, "Circulating tumor cells (CTC) detection: Clinical impact and future directions," Cancer Letters **253** (2), 180-204 (2007).

[7] Alan C. Jung and Douglas S. Paauw, "Diagnosing HIV-Related Disease - Using the CD4 Count as a Guide," Journal of General Internal Medicine **13** (2), 131-136 (1998).

[8] P. Grodzinski, J. Yang, R. H. Liu et al., "A Modular Microfluidic System for Cell Pre-concentration and Genetic Sample Preparation," Biomedical Microdevices **5** (4), 303-310 (2003).

[9] Andreas Radbruch and Diether Recktenwald, "Detection and isolation of rare cells," Current Opinion in Immunology **7** (2), 270-273 (1995).

[10] R K Kumar and A W Lykke, "Cell Separation: a review," Pathology **16** (1), 53-62 (1984).

[11] Maciej Zborowski, in *Scientific and Clinical Applications of Magnetic Carriers*, edited by Urs Häfeli, Wolfgang Schütt, and Maciej Zborowski (Springer, 1997), pp. 205-233.

[12] Ivo Safarik and Mirka Safarikova, "Use of magnetic techniques for the isolation of cells," Journal of Chromatography B: Biomedical Sciences and Applications **722** (1-2), 33-53 (1999).

[13] Nicole Pamme, "Magnetism and microfluidics," Lab on a Chip **6** (1), 24-38 (2005).

[14] R. N. Arun Kumar and Joseph E. Arrowsmith, "Point-of-care testing," Surgery (Oxford) **24** (10), 341 (2006).

[15] J. Svoboda and T. Fujita, "Recent developments in magnetic methods of material separation," Minerals Engineering **16** (9), 785-792 (2003).

[16] R S Molday, S P S Yen, and A Rembaum, "Application of magnetic microspheres in labelling and separation of cells," Nature **268**, 437-438 (1977).

[17] Udo Bilkenroth, Helge Taubert, Dagmar Riemann et al., "Detection and enrichment of disseminated renal carcinoma cells from peripheral blood by immunomagnetic cell separation," International Journal of Cancer **92** (4), 577 - 582 (2001).

[18] Luminita A. Stanciu, Janis Shute, Stephen T. Holgate et al., "Production of IL-8 and IL-4 by positively and negatively selected CD4+ and CD8+ human T cells following a four-step cell separation method including magnetic cell sorting (MACS)," Journal of Immunological Methods **189** (1), 107-115 (1996).

[19] H. Th J. Roerdink, M. R. Schaafsma, F. Olthuis et al., "CD34 cell selection with high gradient magnetic cell sorting and transplantation in patients with breast cancer," The Netherlands Journal of Medicine **50** (5), A4-A5 (1997).

[20] Lee R. Moore, Maciej Zborowski, Liping Sun et al., "Lymphocyte fractionation using immunomagnetic colloid and a dipole magnet flow cell sorter," Journal of Biochemical and Biophysical Methods **37** (1-2), 11-33 (1998).

[21] J. Svoboda, *Magnetic Techniques for the Treatment of Materials*. (Kluwer Academic Publishers, Dordrecht, 2004), pp.138-147, 299-319.

[22] R. S. Molday and L. L. Molday, "Separation of cells labeled with immunospecific iron dextran microspheres using high gradient magnetic chromatography," FEBS Letters **170** (2), 232-238 (1984).

[23] Gareth P. Hatch and Richard E. Stelter, "Magnetic design considerations for devices and particles used for biological high-gradient magnetic separation (HGMS) systems," Journal of Magnetism and Magnetic Materials **225** (1-2), 262-276 (2001).

[24] J. Y. Hwang, M. Takayasu, F. J. Friedlaender et al., "Application of magnetic susceptibility gradients to magnetic separation," Journal of Applied Physics **55** (6), 2592-2594 (1984).

[25] Thomas Schneider, Lee R. Moore, Ying Jing et al., "Continuous flow magnetic cell fractionation based on antigen expression level," Journal of Biochemical and Biophysical Methods **68** (1), 1-21 (2006).

[26] Nicole Pamme, Jan C. T. Eijkel, and Andreas Manz, "On-chip free-flow magnetophoresis: Separation and detection of mixtures of magnetic particles in continuous flow," Journal of Magnetism and Magnetic Materials **307** (2), 237-244 (2006).

[27] S G Frantz, Patent No. 2,056,426 (1936).

[28] M. R. Smolkin and R. D. Smolkin, "Calculation and Analysis of the Magnetic Force Acting on a Particle in the Magnetic Field of Separator. Analysis of the Equations Used in the Magnetic Methods of Separation," IEEE Transactions on Magnetics **42** (11), 3682-3693 (2006).

[29] B. J. Roylance, "Ferrography - then and now," Tribology International **38** (10), 857-862 (2005).

[30] Peter A. Zimmerman, Jodi M. Thomson, Hisashi Fujioka et al., "Diagnosis of Malaria by magnetic deposition microscopy," The American Journal of Tropical Medicine and Hygene **74** (4), 568-572 (2006).

[31] M. Zborowski, C. B. Fuh, and R. Green, "Immunomagnetic isolation of magnetoferritin-labeled cells in a modified ferrograph," Cytometry **24**, 251-259 (1996).

[32] P. Zhang and W. P. Johnson, "Rapid selective ferrographic enumeration of bacteria," Journal of Magnetism and Magnetic Materials **194** (1-3), 267-274 (1999).
[33] Maciej Zborowski, Chwan Bor Fuh, Ralph Green et al., "Analytical Magnetapheresis of Ferritin-Labeled Lymphocytes," Analytical Chemistry **67** (20), 3702-3712 (1995).
[34] Bingbing Fang, Maciej Zborowski, and Lee R. Moore, "Detection of rare MCF-7 breast carcinoma cells from mixtures of human peripheral leukocytes by magnetic deposition analysis," Cytometry **36** (4), 294 - 302 (1999).
[35] C. Bor Fuh, Y. S. Su, and H. Y. Tsai, "Determination of magnetic susceptibility of various ion-labeled red blood cells by means of analytical magnetapheresis," Journal of Chromatography A **1027** (1-2), 289-296 (2004).
[36] M Zborowski, Y Tada, P. S. Malchesky et al., "Quantitative and Qualitative Analysis of Bacteria in Er(III) Solution by Thin-Film Magnetopheresis," APPLIED AND ENVIRONMENTAL MICROBIOLOGY **59** (4), 1187-1193 (1993).
[37] D M Meyer, A Tillinghast, Hanumara N C et al., "Bio-Ferrography to Capture and Separate Polyethylene Wear Debris from Hip Simulator Fluid and Compared With Conventional Filter Method," Journal of Tribology **128** (2), 436-441 (2006).
[38] Jack W. Judy, "Microelectromechanical systems (MEMS): fabrication, design and applications," Smart Materials and Structures **10** (6), 1115-1134 (2001).
[39] Robert Bogue, "MEMS sensors: past, present and future," Sensor Review **27** (1), 7-13 (2007).
[40] Publisher, "Labs-on-a-Chip: origin, highlights and future perspectives," Lab on a Chip **6** (10), 1266-1273 (2006).
[41] Changqing Yi, Cheuk-Wing Li, Shenglin Ji et al., "Microfluidics technology for manipulation and analysis of biological cells," Analytica Chimica Acta **560** (1-2), 1-23 (2006).
[42] Douglas B. Weibel and George M. Whitesides, "Applications of microfluidics in chemical biology," Current Opinion in Chemical Biology **10** (6), 584-591 (2006).
[43] S Takayama, J C McDonald, E Ostuni et al., "Patterning cells and their environments using multiple laminar fluid flows in capillary networks," PNAS **96**, 5545-5548 (1999).
[44] Hideaki Hisamoto, Shun-ichi Funano, and Shigeru Terabe, "Integration of Valving and Sensing on a Capillary-Assembled Microchip," Analytical Chemistry **77** (7), 2266-2271 (2005).
[45] Claire Simonnet and Alex Groisman, "Two-dimensional hydrodynamic focusing in a simple microfluidic device," Applied Physics Letters **87** (11), 114104-114104-114103 (2005).
[46] D J Beebe, G A Mensing, and G M Walker, "Physics and applications of microfluidics in biology," Annual Review of Biomedical Engineering **4**, 261-286 (2002).
[47] Thomas Laurel, Filip Petersso, and Andreas Nilsso, "Chip integrated strategies for acoustic separation and manipulation of cells and particles," Chemical Society Reviews **36** (3), 492-506 (2007).

[48] Michael P. Hughes, "Strategies for dielectrophoretic separation in laboratory-on-a-chip systems," Electrophoresis **23** (16), 2569 - 2582 (2002).
[49] Jitendra N. Mehrishi and Johann Bauer, "Electrophoresis of cells and the biological relevance of surface charge," Electrophoresis **23** (13), 1984 - 1994 (2002).
[50] Timothy A. Crowley and Vincent Pizziconi, "Isolation of plasma from whole blood using planar microfilters for lab-on-a-chip applications," Lab on a Chip **5** (9), 922-929 (2005).
[51] Xuanhong Chen, Daniel Irimi, Meredith Dixo et al., "A microfluidic device for practical label-free CD4+ T cell counting of HIV-infected subjects," Lab on a Chip **7** (2), 170-178 (2007).
[52] H M Shapiro, *Practical Flow Cytometry*. (Wiley-Liss, New York, 1995).
[53] David Holme, Joseph K. Sh, Peter L. Roac et al., "Bead-based immunoassays using a micro-chip flow cytometer," Lab on a Chip **7** (8), 1048-1056 (2007).
[54] Z. Wan, J. El-Al, M. Engelun et al., "Measurements of scattered light on a microchip flow cytometer with integrated polymer based optical elements," Lab on a Chip **4** (4), 372-377 (2004).
[55] Gwo-Bin Lee, Che-Hsin Lin, and Guan-Liang Chang, "Micro flow cytometers with buried SU-8/SOG optical waveguides," Sensors and Actuators A: Physical **103** (1-2), 165-170 (2003).
[56] Supratim Choudhuri, "Microarrays in biology and medicine," Journal of Biochemical and Molecular Toxicology **18** (4), 171 - 179 (2004).
[57] Jin-Woo Choi, Kwang W. Oh, Arum Han et al., "Development and Characterization of Microfluidic Devices and Systems for Magnetic Bead-Based Biochemical Detection," Biomedical Microdevices **3** (3), 191-200 (2001).
[58] G Blankenstein, in *Scientific and clinical applications of magnetic carriers*, edited by Urs Häfeli, Wolfgang Schütt, and Maciej Zborowski (1997), pp. 233-248.
[59] Vasile I. Furdu and D. Jed Harriso, "Immunomagnetic T cell capture from blood for PCR analysis using microfluidic systems," Lab on a Chip **4** (6), 614-618 (2004).
[60] David W. Inglis, R. Riehn, R. H. Austin et al., "Continuous microfluidic immunomagnetic cell separation," Applied Physics Letters **85** (21), 5093-5095 (2004).
[61] Benjamin B. Yellen, Randall M. Er, Hui S. So et al., "Traveling wave magnetophoresis for high resolution chip based separations," Lab on a Chip **7** (12), 1681-1688 (2007).
[62] Hitoshi Watarai and Makoto Namba, "Capillary magnetophoresis of human blood cells and their magnetophoretic trapping in a flow system," Journal of Chromatography A **961** (1), 3-8 (2002).
[63] Kristian Smistrup, Peter T. Tang, Ole Hansen et al., "Microelectromagnet for magnetic manipulation in lab-on-a-chip systems," Journal of Magnetism and Magnetic Materials **300** (2), 418-426 (2006).
[64] Chengxun Liu, Liesbet Lagae, Roel Wirix-Speetjens et al., "On-chip separation of magnetic particles with different magnetophoretic mobilities," Journal of Applied Physics **101** (2), 024913-024913-024914 (2007).

[65] Kang-Yi Lie, Jr-Lung Li, Cheng-Yu Li et al., "Purification and enrichment of virus samples utilizing magnetic beads on a microfluidic system," Lab on a Chip **7** (7), 868-875 (2007).

[66] Ki-Ho Han and A. Bruno Frazier, "Continuous magnetophoretic separation of blood cells in microdevice format," Journal of Applied Physics **96** (10), 5797-5802 (2004).

[67] Yousef Haik, Vinay Pai, and Ching-Jen Chen, "Development of magnetic device for cell separation," Journal of Magnetism and Magnetic Materials **194** (1-3), 254-261 (1999).

[68] Susanne Dam Nielsen, Jens Ole Nielsen, and John-Erik Stig Hansen, "In vitro separation and expansion of CD4 lymphocytes from HIV-infected individuals without activation of HIV infection," Journal of Immunological Methods **200** (1-2), 107-112 (1997).

[69] Jin-Woo Choi, Chong H. Ahn, Shekhar Bhansali et al., "A new magnetic bead-based, filterless bio-separator with planar electromagnet surfaces for integrated bio-detection systems," Sensors and Actuators B: Chemical **68** (1-3), 34-39 (2000).

[70] Tsung-Shune Chin, "Permanent magnet films for applications in microelectromechanical systems," Journal of Magnetism and Magnetic Materials **209** (1-3), 75-79 (2000).

[71] Pulak Nath, Shuvo Roy, Terrence Conlisk et al., "A System for Micro/Nano Fluidic Flow Diagnostics," Biomedical Microdevices **7** (3), 169 - 177 (2005).

[72] Pulak Nath, Lee R. Moore, Maciej Zborowski et al., "A method to obtain uniform magnetic-field energy density gradient distribution using discrete pole pieces for a microelectromechanical-system-based magnetic cell separator," Journal of Applied Physics **99** (8), 08R905-908R905-903 (2006).

[73] Chien-Hung Ho, Kan-Ping Chin, Chii-Rong Yang et al., "Ultrathick SU-8 mold formation and removal, and its application to the fabrication of LIGA-like micromotors with embedded roots," Sensors and Actuators A: Physical **102** (1-2), 130-138 (2002).

[74] Nosang V. Myung, D.-Y. Park, B.-Y. Yoo et al., "Development of electroplated magnetic materials for MEMS," Journal of Magnetism and Magnetic Materials **265** (2), 189-198 (2003).

[75] J. L. McCrea, G. Palumbo, G. D. Hibbard et al., "Properties and Applications for Electrodeposited Nanocrystalline Fe-Ni Alloys," Review on Advances Materials Science **5**, 252-258 (2003).

[76] Ki-Ho Han, Rachel D. McConnell, Christopher J. Easley et al., "An active microfluidic system packaging technology," Sensors & Actuators: B. Chemical **122** (1), 337-346 (2007).

[77] Jeffrey J. Chalmers, Yang Zhao, Masayuki Nakamura et al., "An instrument to determine the magnetophoretic mobility of labeled, biological cells and paramagnetic particles," Journal of Magnetism and Magnetic Materials **194** (1-3), 231-241 (1999).

[78] Wen H. Ko, "Trends and frontiers of MEMS," Sensors & Actuators: A. Physical **136** (1), 62-67 (2007).

[79] Stefan Haeberl and Roland Zengerl, "Microfluidic platforms for lab-on-a-chip applications," Lab on a Chip **7** (9), 1094-1110 (2007).
[80] William H. Fissell, Aaron J. Fleischman, H. David Humes et al., "Development of continuous implantable renal replacement: past and future," Translational Research **150** (6), 327-336 (2007).
[81] Geoffrey Kotzar, Mark Freas, Phillip Abel et al., "Evaluation of MEMS materials of construction for implantable medical devices," Biomaterials **23** (13), 2737-2750 (2002).
[82] Richard R. A. Syms and David F. Moore, "Optical MEMS for telecoms," Materials Today **5** (8), 26-35 (2002).
[83] Peter Gammel, Georg Fischer, and Jereme Bouchaud, "RF MEMS and NEMS technology, devices, and applications," Bell Labs Technical Journal **10** (3), 29 - 59 (2005).
[84] Ravi Khanna, "MEMS fabrication perspectives from the MIT Microengine Project," Surface and Coatings Technology **163-164**, 273-280 (2003).
[85] P. Vettiger, J. Brugger, M. Despont et al., "High-aspect-ratio, ultrathick, negative-tone near-UV photoresist and its applications for MEMS," Sensors and Actuators A: Physical **64** (1), 33-39 (1998).
[86] L. T. Romankiw, "A path: from electroplating through lithographic masks in electronics to LIGA in MEMS," Electrochimica Acta **42** (20-22), 2985-3005 (1997).
[87] Chantal Khan Malek and Volker Saile, "Applications of LIGA technology to precision manufacturing of high-aspect-ratio micro-components and -systems: a review," Microelectronics Journal **35** (2), 131-143 (2004).
[88] L. A. Tse, P. J. Hesketh, D. W. Rosen et al., "Stereolithography on silicon for microfluidics and microsensor packaging," Microsystem Technologies **9** (5), 319 - 323 (2003).
[89] X. Zhang, X. N. Jiang, and C. Sun, "Micro-stereolithography of polymeric and ceramic microstructures," Sensors and Actuators A: Physical **77** (2), 149-156 (1999).
[90] I. W. Rangelow, "Reactive ion etching for high aspect ratio silicon micromachining," Surface and Coatings Technology **97** (1-3), 140-150 (1997).
[91] Samuel K. Sia and George M. Whitesides, "Microfluidic devices fabricated in Poly(dimethylsiloxane) for biological studies," Electrophoresis **24** (21), 3563 - 3576 (2003).
[92] Jessamine M. K. Ng, Irina Gitlin, Abraham D. Stroock et al., "Components for integrated poly(dimethylsiloxane) microfluidic systems," Electrophoresis **23** (20), 3461 - 3473 (2002).
[93] Jong Soo K, Hyun C. Yoo, Haesik Yan et al., "A polymer-based microfluidic device for immunosensing biochips," Lab on a Chip **3** (2), 106-113 (2003).
[94] Larry J. Mille, Matthew E. Stewar, Jonathan V. Sweedle et al., "Microfluidic devices for culturing primary mammalian neurons at low densities," Lab on a Chip **7** (8), 987-994 (2007).
[95] Christelle Guill, James M. Karlinse, and James P. Lander, "On-chip pumping for pressure mobilization of the focused zones following microchip isoelectric focusing," Lab on a Chip **7** (1), 112-118 (2006).

[96] Liju Yan, Padmapriya P. Banad, Mohammad R. Chatn et al., "A multifunctional micro-fluidic system for dielectrophoretic concentration coupled with immuno-capture of low numbers of Listeria monocytogenes," Lab on a Chip **6** (7), 896-905 (2006).

[97] Sungyoung Choi and Je-Kyun Park, "Microfluidic system for dielectrophoretic separation based on a trapezoidal electrode array," Lab on a Chip **5** (10), 1161-1167 (2005).

[98] J. Y. Kim, J. Y. Baek, K. A. Lee et al., "Automatic aligning and bonding system of PDMS layer for the fabrication of 3D microfluidic channels," Sensors and Actuators A: Physical **119** (2), 593-598 (2005).

[99] H. Lorenz, M. Despont, N. Fahrnl et al., "SU-8: a low-cost negative resist for MEMS," Journal of Micromechanics and Microengineering **7** (3), 121-124 (1997).

[100] H. Lorenz, M. Despont, P. Vettiger et al., "Fabrication of photoplastic high-aspect ratio microparts and micromolds using SU-8 UV resist," Microsystem Technologies **4** (3), 143 - 146 (1998).

[101] J. Zhang, K. L. Tan, and H. Q. Gong, "Characterization of the polymerization of SU-8 photoresist and its applications in micro-electro-mechanical systems (MEMS)," Polymer Testing **20** (6), 693-701 (2001).

[102] J. M. Ruano -Lopez, M. Aguirregabiria, M. Tijero et al., "A new SU-8 process to integrate buried waveguides and sealed microchannels for a Lab-on-a-Chip," Sensors & Actuators: B. Chemical **114** (1), 542-551 (2006).

[103] Santeri Tuomikoski and Sami Franssila, "Wafer-Level Bonding of MEMS Structures with SU-8 Epoxy Photoresist," Physica Scripta **2004** (T114), 223-226 (2004).

[104] J. C. Ribeiro, G. Minas, P. Turmezei et al., "A SU-8 fluidic microsystem for biological fluids analysis," Sensors & Actuators: A. Physical **123-124**, 77-81 (2005).

[105] Maria Agirregabiria, Francisco Javier Blanco, Javier Berganzo et al., "SDS-CGE of proteins in microchannels made of SU-8 films," Electrophoresis **27** (18), 3627 - 3634 (2006).

[106] F. J. Blanco, M. Agirregabiria, J. Garcia et al., "Novel three-dimensional embedded SU-8 microchannels fabricated using a low temperature full wafer adhesive bonding," Journal of Micromechanics and Microengineering **14** (7), 1047-1056 (2004).

[107] J. Carlier, S. Arscott, V. Thomy et al., "Integrated microfluidics based on multi-layered SU-8 for mass spectrometry analysis," Journal of Micromechanics and Microengineering **14** (4), 619-624 (2004).

[108] Yun-Ju Chuang, Fan-Gang Tseng, Jen-Hau Cheng et al., "A novel fabrication method of embedded micro-channels by using SU-8 thick-film photoresists," Sensors and Actuators A: Physical **103** (1-2), 64-69 (2003).

[109] Lung-Jieh Yang, Yu-Tang Chen, Shung-Wen Kang et al., "Fabrication of SU-8 embedded microchannels with circular cross-section," International Journal of Machine Tools and Manufacture **44** (10), 1109-1114 (2004).

[110] M. Lindblom, H. M. Hertz, and A. Holmberg, "SU-8 plating mold for high-aspect-ratio nickel zone plates," Microelectronic Engineering **84** (5-8), 1136-1139 (2007).
[111] Sung-Jin Kim, Haesik Yang, Kyuwon Kim et al., "Study of SU-8 to make a Ni master-mold: Adhesion, sidewall profile, and removal," Electrophoresis **27** (16), 3284 - 3296 (2006).
[112] J. A. Van Kan, I. Rajta, K. Ansari et al., "Nickel and copper electroplating of proton beam micromachined SU-8 resist," Microsystem Technologies **8** (6), 383 - 386 (2002).
[113] Wen Dai and Wanjun Wang, "Selective metallization of cured SU-8 microstructures using electroless plating method," Sensors & Actuators: A. Physical **135** (1), 300-307 (2007).
[114] Ju-Nan Kuo, Chia-Chun Hsieh, Sung-Yi Yang et al., "An SU-8 microlens array fabricated by soft replica molding for cell counting applications," Journal of Micromechanics and Microengineering **17** (4), 693-699 (2007).
[115] Alvaro Mata, Cynthia Boehm, Aaron J. Fleischman et al., "Growth of connective tissue progenitor cells on microtextured polydimethylsiloxane surfaces," Journal of Biomedical Materials Research **62** (4), 499 - 506 (2002).
[116] Mary B. Chan-Park, Jun Zhang, Yehai Yan et al., "Fabrication of large SU-8 mold with high aspect ratio microchannels by UV exposure dose reduction," Sensors and Actuators B: Chemical **101** (1-2), 175-182 (2004).
[117] B. Y. Shew, C. H. Kuo, Y. C. Huang et al., "UV-LIGA interferometer biosensor based on the SU-8 optical waveguide," Sensors and Actuators A: Physical **120** (2), 383-389 (2005).
[118] M Nordstroum, J Hubner, and Anja Boisen, "Sloped side walls in SU-8 structures with Step-and-Flash processing," Microelectronic Engineering **83** (4-9), 1269-1272 (2006).
[119] Manhee Han, Woonseob Lee, Sung-Keun Lee et al., "3D microfabrication with inclined/rotated UV lithography," Sensors and Actuators A: Physical **111** (1), 14-20 (2004).
[120] Alvaro Mata, Aaron J. Fleischman, and Shuvo Roy, "Fabrication of multi-layer SU-8 microstructures," Journal of Micromechanics and Microengineering **16** (2), 276-284 (2006).
[121] Hironobu Sato, Daisuke Yagyu, Seiki Ito et al., "Improved inclined multi-lithography using water as exposure medium and its 3D mixing microchannel application," Sensors & Actuators: A. Physical **128** (1), 183-190 (2006).
[122] Hyoung J. Cho, Shekhar Bhansali, and Chong H. Ahn, "Electroplated thick permanent magnet arrays with controlled direction of magnetization for MEMS application," Journal of Applied Physics **87** (9), 6340-6342 (2000).
[123] Chang Liu, "Development of surface micromachined magnetic actuators using electroplated permalloy," Mechatronics **8** (5), 613-633 (1998).
[124] D. Niarchos, "Magnetic MEMS: key issues and some applications," Sensors and Actuators A: Physical **109** (1-2), 166-173 (2003).
[125] T. Fritz, M. Griepentrog, W. Mokwa et al., "Determination of Young's modulus of electroplated nickel," Electrochimica Acta **48** (20-22), 3029 - 3035 (2003).

[126] Yong-hua Zhang, Gui-fu Ding, Yu-li Cai et al., "Electroplating of low stress permalloy for MEMS," Materials Characterization **57** (2), 121-126 (2006).
[127] C. Massin, G. Boero, F. Vincent et al., "High-Q factor RF planar microcoils for micro-scale NMR spectroscopy," Sensors and Actuators A: Physical **97-98**, 280-288 (2002).
[128] Tetsuya Osaka, "Recent development of Magnetic recording head core materials by plating method," Electrochimica Acta **44** (21-22), 3885-3890 (1999).
[129] E. I. Cooper, C. Bonhote, J. Heidmann et al., "Recent developments in high-moment electroplated materials for recording heads," IBM Journal of Research and Development **49** (1), 103-126 (2005).
[130] J. Y. Park and M. G. Allen, "Development of magnetic materials and processing techniques applicable to integrated micromagnetic devices," Journal of Micromechanics and Microengineering **8** (4), 307-316 (1998).
[131] M. Agirregabiria, F. J. Blanco, J. Berganzo et al., "Fabrication of SU-8 multilayer microstructures based on successive CMOS compatible adhesive bonding and releasing steps," Lab on a Chip **5** (5), 545-552 (2005).
[132] Wen Dai, Kun Lian, and Wanjun Wang, "A quantitative study on the adhesion property of cured SU-8 on various metallic surfaces," Microsystem Technologies **11** (7), 526 - 534 (2005).
[133] Ewan H. Conradie and David F. Moore, "SU-8 thick photoresist processing as a functional material for MEMS applications," Journal of Micromechanics and Microengineering **12** (4), 368-374 (2002).
[134] Yu-Tzu Chen and Denz Lee, "A bonding technique using hydrophilic SU-8," Journal of Micromechanics and Microengineering **17** (10), 1978-1984 (2007).
[135] Sheng Li, Carl B. Freidhoff, Robert M. Young et al., "Fabrication of micronozzles using low-temperature wafer-level bonding with SU-8," Journal of Micromechanics and Microengineering **13** (5), 732-738 (2003).
[136] Liming Yu, Francis E. H. Tay, Guolin Xu et al., "Adhesive bonding with SU-8 at wafer level for microfluidic devices," Journal of Physics: Conference Series **34** (1), 776-781 (2006).
[137] F. Niklaus, G. Stemme, J. Q. Lu et al., "Adhesive wafer bonding," Journal of Applied Physics **99** (3), 031101-031101-031128 (2006).
[138] http://www.microchem.com/products/su_eight.htm.
[139] Q. Y. Tong, "Wafer bonding for integrated materials," Materials Science and Engineering: B **87** (3), 323 - 328 (2001).
[140] Anish Saran, Don C. Abeysinghe, and Joseph T. Boyd, "Microelectromechanical system pressure sensor integrated onto optical fiber by anodic bonding," Applied Optics **45** (8), 1737-1742 (2006).
[141] A. Sayah, D. Solignac, T. Cueni et al., "Development of novel low temperature bonding technologies for microchip chemical analysis applications," Sensors and Actuators A: Physical **84** (1-2), 103-108 (2000).
[142] J. Oberhammer, F. Niklaus, and G. Stemme, "Selective wafer-level adhesive bonding with benzocyclobutene for fabrication of cavities," Sensors and Actuators A: Physical **105** (3), 297-304 (2003).

[143] F. Niklaus, H. Andersson, P. Enoksson et al., "Low temperature full wafer adhesive bonding of structured wafers," Sensors and Actuators A: Physical **92** (1-3), 235-241 (2001).
[144] C. T. Pan, P. J. Cheng, M. F. Chen et al., "Intermediate wafer level bonding and interface behavior," Microelectronics Reliability **45** (3-4), 657-663 (2005).
[145] Hui Yu, Oluwaseyi Balogun, Biao Li et al., "Fabrication of three-dimensional microstructures based on singled-layered SU-8 for lab-on-chip applications," Sensors & Actuators: A. Physical **127** (2), 228-234 (2006).
[146] Francis E. H. Tay, J. A. van Kan, F. Watt et al., "A novel micro-machining method for the fabrication of thick-film SU-8 embedded micro-channels," Journal of Micromechanics and Microengineering **11** (1), 27-32 (2001).
[147] P. Svasek, E. Svasek, B. Lendl et al., "Fabrication of miniaturized fluidic devices using SU-8 based lithography and low temperature wafer bonding," Sensors and Actuators A: Physical **115** (2-3), 591-599 (2004).
[148] Muralidhar K. Ghantasala, Jason P. Hayes, Erol C. Harvey et al., "Patterning, electroplating and removal of SU-8 moulds by excimer laser micromachining," Journal of Micromechanics and Microengineering **11** (2), 133-139 (2001).
[149] http://www.microchem.com/products/kmpr.htm.
[150] E. Kukharenka and M. Kraft, "Realization of electroplating molds with thick positive SPR 220-7 photoresist," Journal of Materials Science: Materials in Electronics **14** (5-7), 319-322 (2003).
[151] E. Kukharenka, M. M. Farooqui, L. Grigore et al., "Electroplating moulds using dry film thick negative photoresist," Journal of Micromechanics and Microengineering **13** (4), S67-S74 (2003).
[152] E. Koukharenko, M. Kraft, G. J. Ensell et al., "A comparative study of different thick photoresists for MEMS applications," Journal of Materials Science: Materials in Electronics **16** (11-12), 741 - 747 (2005).
[153] http://www.microchem.com/products/pdf/SU-8-Adhesion-Results.pdf.
[154] S Garst, M Schuenemann, M Solomon et al., "Fabrication of multilayered microfluidic 3D polymer packages," 55th Electronic Components and Technology Conference, 2005, 603-610 (2005).
[155] R B Bird, W E Stewart, and E L Lightfoot, *Transpoert Phenomena*, 2 ed. (Jhon Wiley & Sons Inc, New York, 2002), p.529.
[156] Liping Sun, Maciej Zborowski, Lee R. Moore et al., "Continuous, flow-through immunomagnetic cell sorting in a quadrupole field," Cytometry **33** (4), 469 - 475 (1998).
[157] Ying Jing, Lee R. Moore, P. Stephen Williams et al., "Blood progenitor cell separation from clinical leukapheresis product by magnetic nanoparticle binding and magnetophoresis," Biotechnology and Bioengineering **96** (6), 1139 - 1154 (2007).
[158] Oscar Lara, Xiaodong Tong, Maciej Zborowski et al., "Comparison of two immunomagnetic separation technologies to deplete T cells from human blood samples," Biotechnology and Bioengineering **94** (1), 66 - 80 (2006).
[159] Nan Xia, Tom P. Hunt, Brian T. Mayers et al., "Combined microfluidic-micromagnetic separation of living cells in continuous flow," Biomedical Microdevices **8** (4), 299 - 308 (2006).

[160] Michael Berger, Judith Castelino, Richard Huang et al., "Design of a microfabricated magnetic cell separator," Electrophoresis **22** (18), 3883 - 3892 (2001).

[161] Jin-Woo Choi, Trifon M. Liakopoulos, and Chong H. Ahn, "An on-chip magnetic bead separator using spiral electromagnets with semi-encapsulated permalloy," Biosensors and Bioelectronics **16** (6), 409 - 416 (2001).

Appendix A
Mask Layout

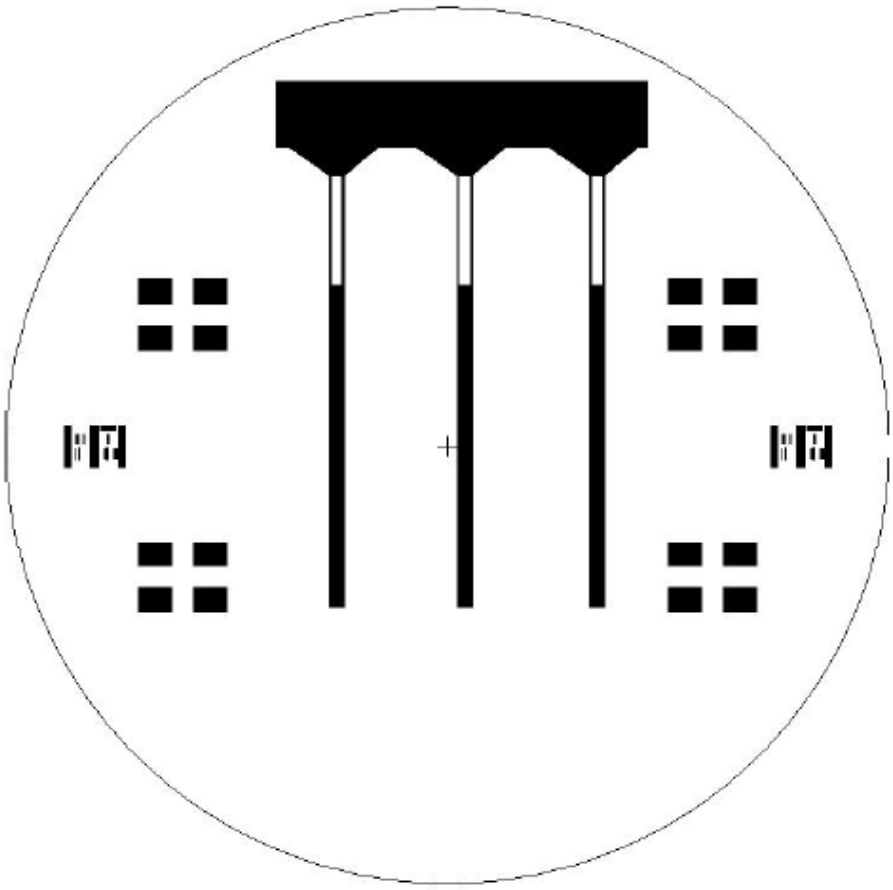

Figure A-1: Mask layout for fabricating open seed layers on the substrate wafer of the isodynamic OGMS channels (Polarity – digitized area is “dark”, mirror option – “no”)

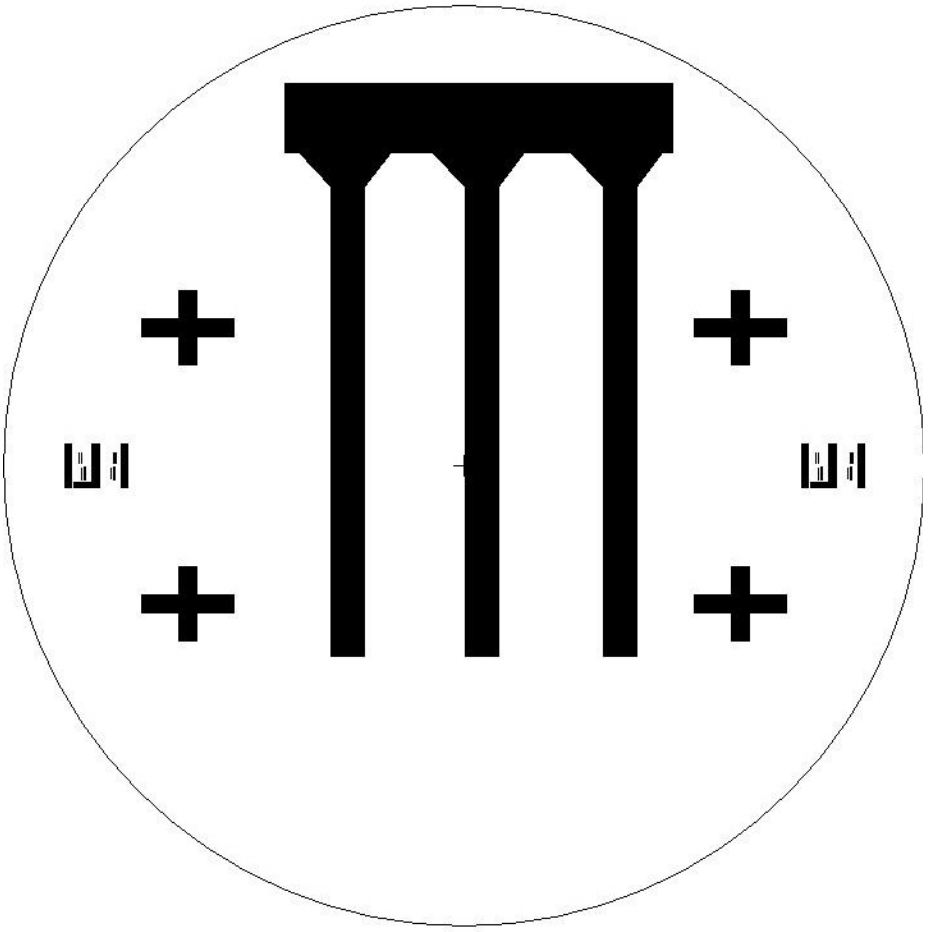

Figure A-2: Mask layout for fabricating seed layer on the cap wafer of the isodynamic OGMS channels (Polarity – digitized area is "dark", mirror option – "no")

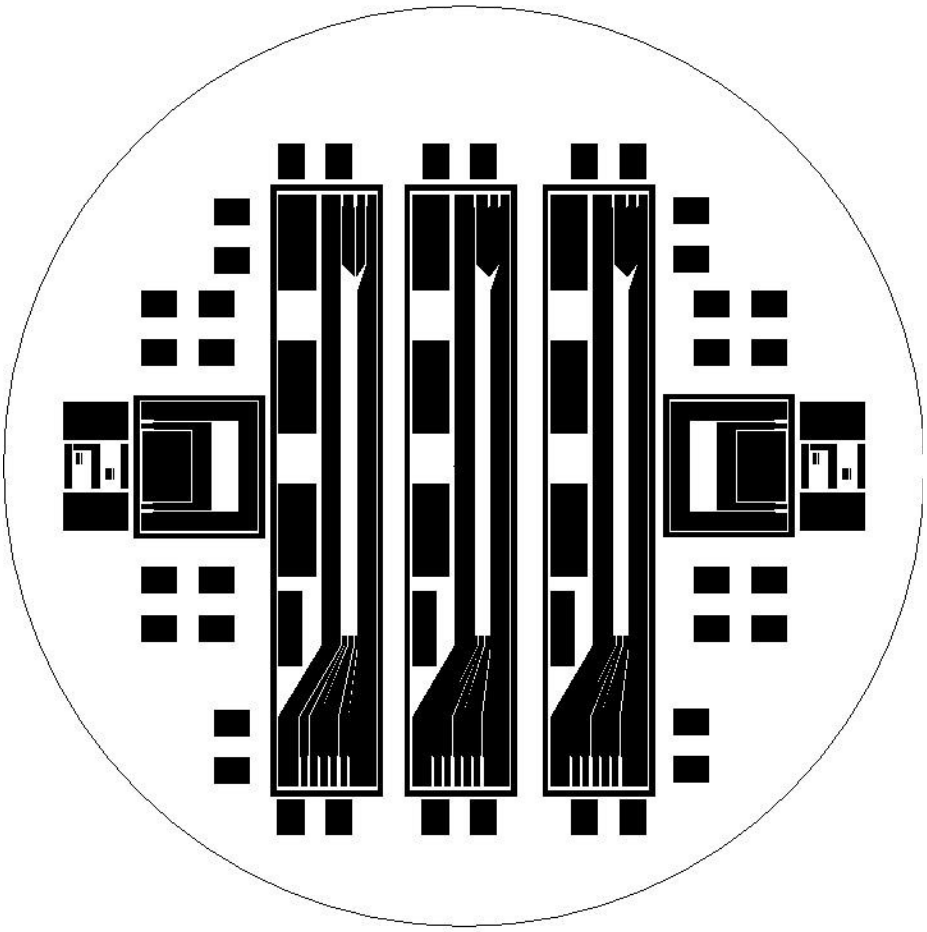

Figure A-3: Mask layout for fabricating open OGMS channels on the substrate wafer (Polarity – digitized area is “clear”, mirror option – “no”)

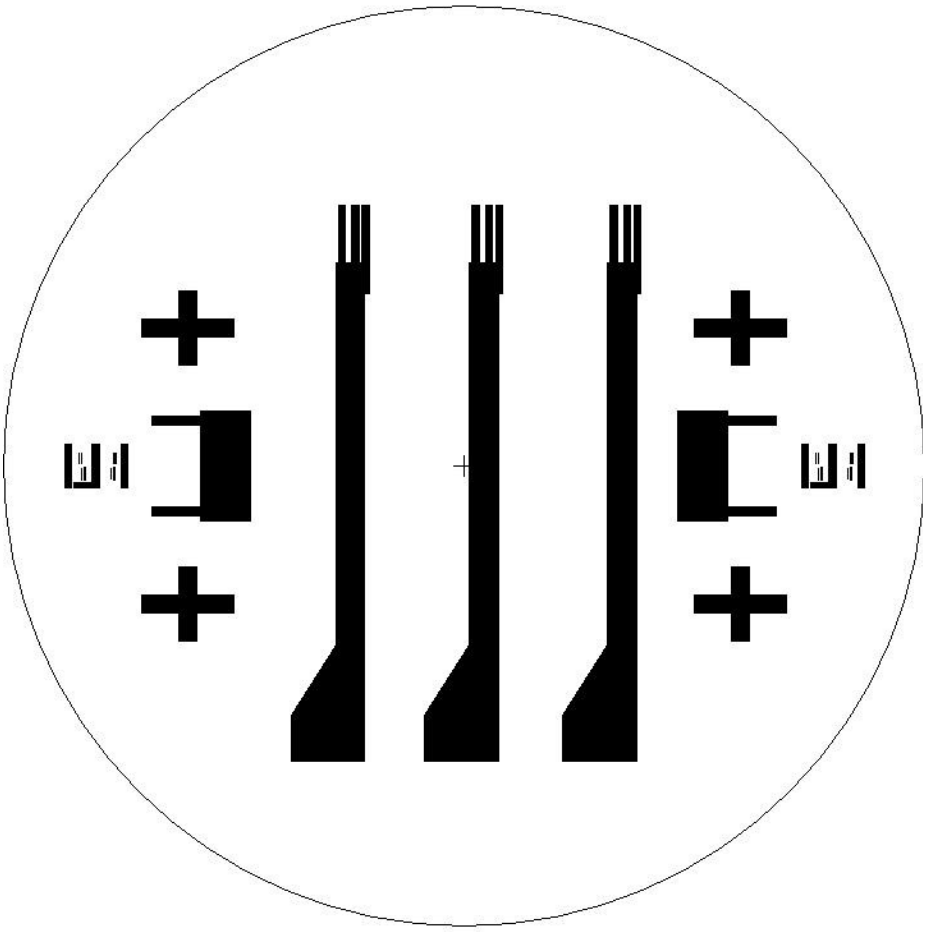

Figure A-4: Mask layout for fabricating selectively exposed bond layer on the cap wafer to form enclosed OGMS channels (Polarity – digitized area is “clear”, mirror option – “no”)

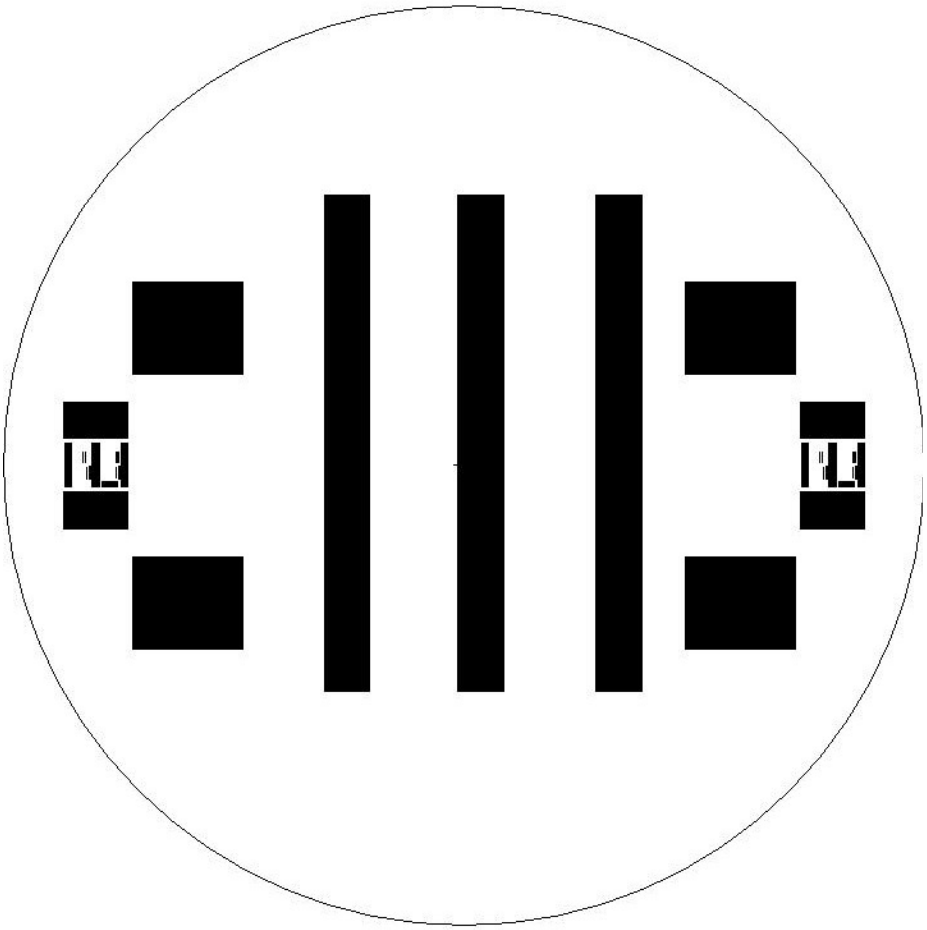

Figure A-5: Mask layout (two masks) for fabricating mold layers on the substrate wafer (Polarity – digitized area is “clear”, mirror option – “no” for one mask and “yes” for the other)

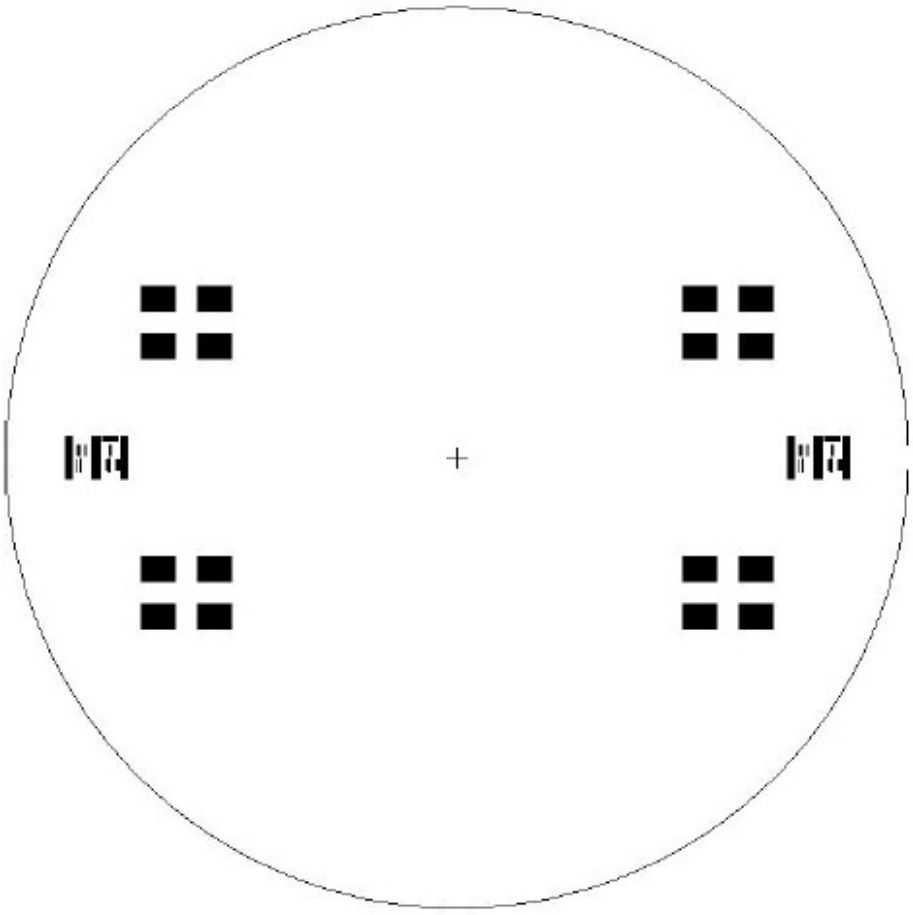

Figure A-6: Mask layout for fabricating metal layer for bond alignment on the cap wafer for fabricating enclosed microchannels (Polarity – digitized area is “dark”, mirror option – “no”)

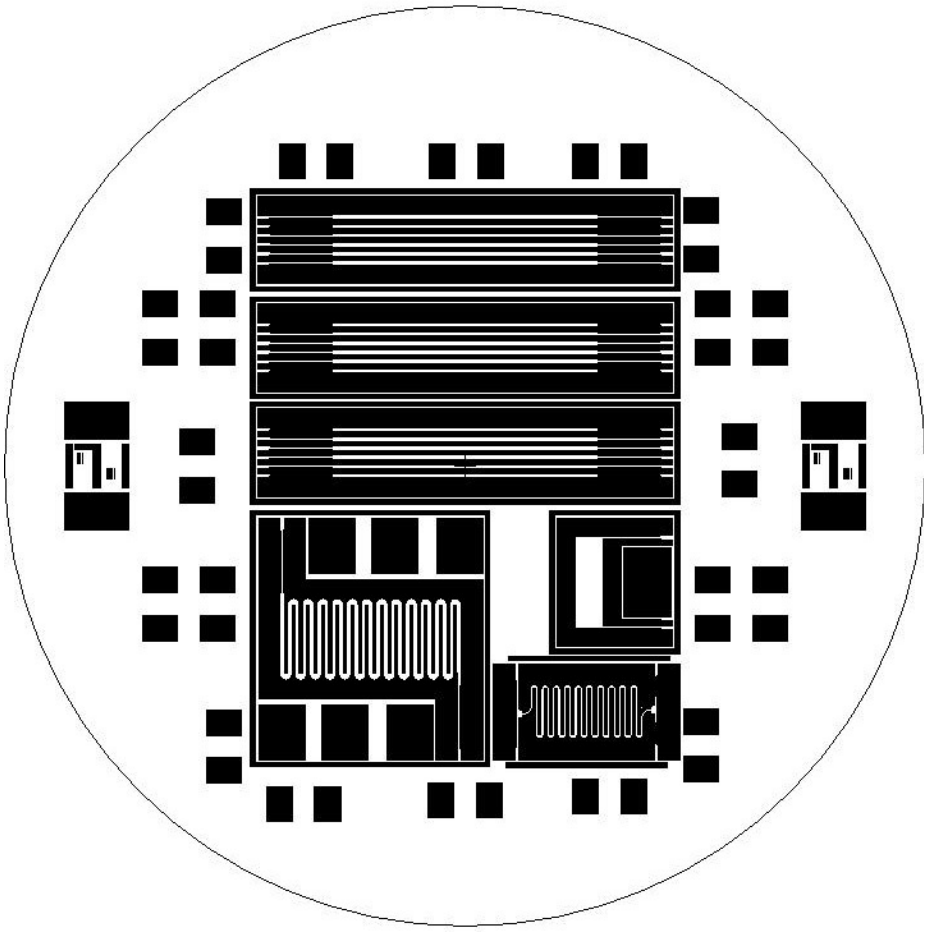

Figure A-7: Mask layout for fabricating open deposition channels (multi-channel design) on the substrate wafer (Polarity – digitized area is “clear”, mirror option – “no”)

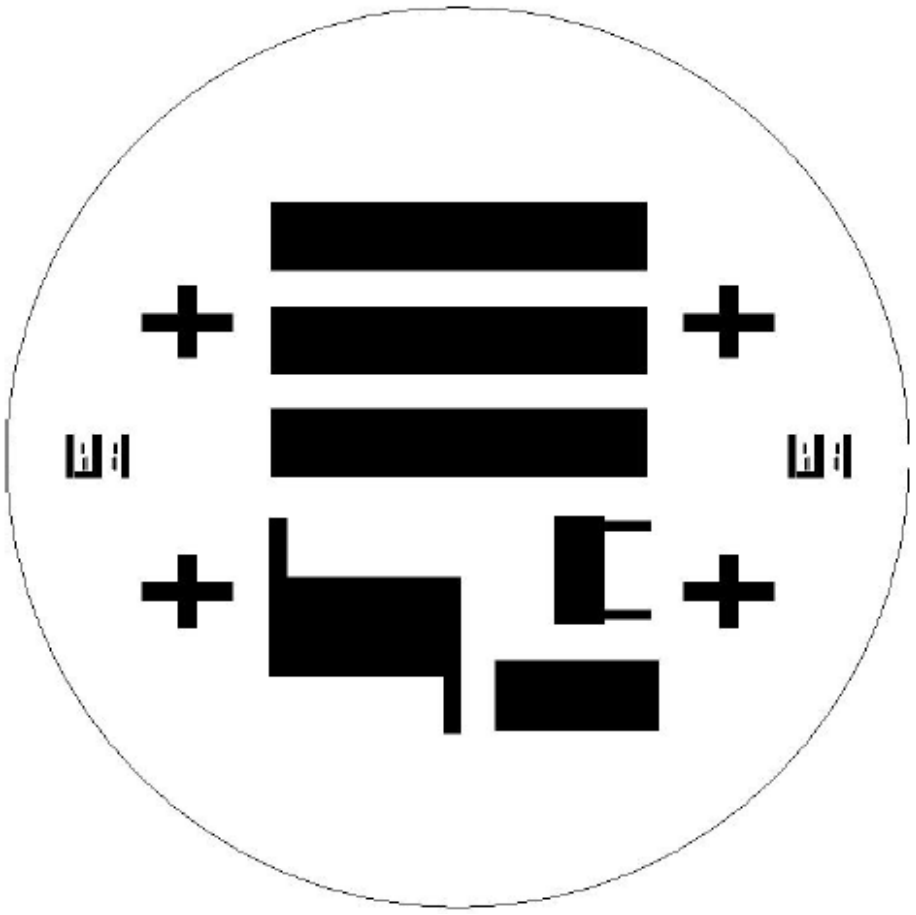

Figure A-8: Mask layout for fabricating selectively exposed bond layer on the cap wafer to form enclosed deposition channels (multi-channel design) (Polarity – digitized area is “clear”, mirror option – “no”)

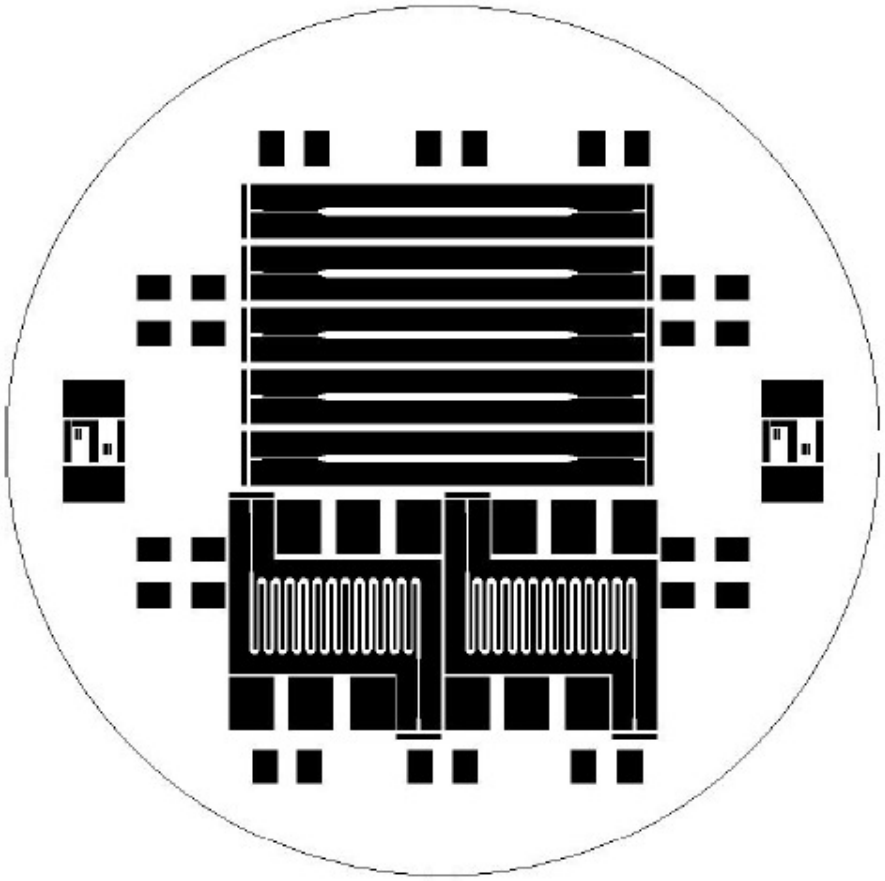

Figure A-9: Mask layout for fabricating open deposition channels (single-channel design) on the substrate wafer (Polarity – digitized area is “clear”, mirror option – “no”)

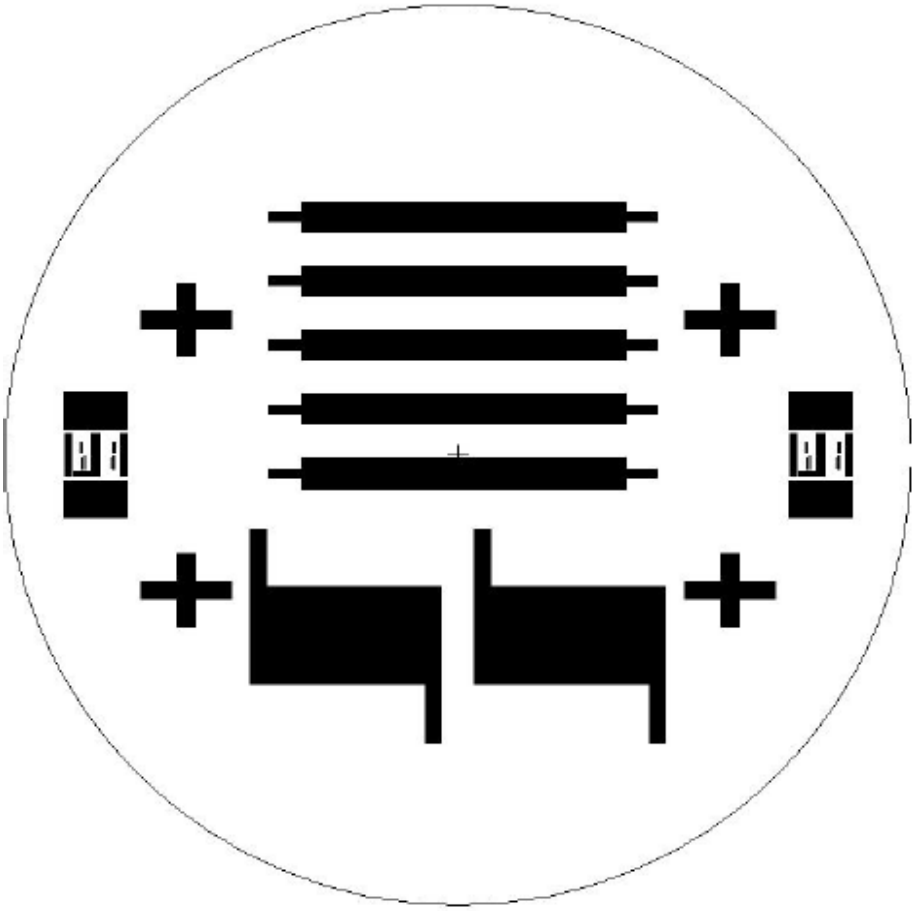

Figure A-10: Mask layout for fabricating selectively exposed bond layer on the cap wafer to form enclosed deposition channels (single-channel design) (Polarity – digitized area is “clear”, mirror option – “no”)

Appendix B
Microfabrication Protocols

Formation of Seed Layer		
Steps	**Process**	**Comments**
1.	Prianha clean Pyrex Wafer	
2.	Sputter deposition ~200Å Cr.~2000Å Ni In Discovery ™ – 24, Vacuum Deposition System, Denton Vacuum Inc, Moorestown, NJ	Use program "xanna", Cr delay = 45 sec., Ni delay = 450 sec.
3.	Spin coat Standard Photoresist (Microposit ™ S1813™ Positive Photoresist, Rohm and Haas Electronic Materials, Marlborough, MA): 4000 rpm, 30 sec.	Spinner (Model# 5110/C, Solitec Inc., Santa Clara, CA) Parameters: Solvent = 230 (t = 004) Resist = 0 (t = 00.4) Spread = 0 (t = 1.5) Spin = 400 (t = 030)
4.	Soft Bake: Hotplate, 95C, 1 min, individually	
5.	Exposure: 4 sec., through mask, hard, contact, top side alignment	Mask #1: Mask #2: Use these masks to get two different set of wafers – one will be small seed layer and the other will be big seed layer.
6.	Develop: - In developer solution (MicroDev, Microposit ™ developer concentrate, Rohm and Haas Electronic Materials, Marlborough, MA) - ~ 2 min, individual wafers, constant agitation with moving the boat inside the solution	Removal of PR is not uniform and removal time varies from wafer to wafer varies. If multiple wafers are used, some times they shatter while vigorously moving inside the developer solution. It is suggested that each wafer is developed individually
7.	Hard Bake: Hotplate, 115C, 1 min, individually	
8.	Ni Etch: - In Nickel Etchant solution (Nickel Etchant, Type TFB, Transene Company, Danvers, MA) placed on a magnetic stirrer with "Heat' setting at ~3 and 'Stir' setting at 6. - ~ 2 min, individual wafer, end point based on observation (see comments)	After placing the wafer inside the etchant solution, stay alert and keep inspecting the wafer. The wafer will go through a sharp color change (from shiny to dark complexion). When the color change happens immediately remove wafer from the etchant and wash in DI water. The wafer will

		become semi-transparent. If the wafer is kept longer, all the metal layers (except the patterned portion) is removed and the wafer becomes transparent, however, in this way undercut occurs and often times small features like alignment marks are lost. Hence metal etch is done in two steps – First, major portion of the Ni layer is etched in Nickel Etchant and then the remaining nickel and thin Cr is etched ion Ni-Cr Etchant.
9.	Ni-Cr Etch: - Dip in/out into the Pink Ni-Cr etchant (Nichrome Etchant, Type 10, Transene Company, Danvers, MA) few times until the wafer becomes completely transparent except the patterned area.	Ni-Cr etchant is slower than the Ni etchant, and thus allows detecting the end point without significant undercut of critical zones.
10.	PR removal: The PR on the patterned metal layers is removed by washing the wafer in Acetone.	
11.	Dehydration: Dehydrate wafers overnight at 175C.	
Formation of Micro channel Layer (3 layer process)		
12.	Start with dehydrated Pyrex wafer with **small seed** patterns on it.	Make sure SU-8 process is applied on the side of the wafer with no metal layers
13.	Spin Coat Su-8 2010 on a PI spinner (WS 400D-6NPP- Lite, Laurell Technologies, North Wales, PA) Spin Cycle: rpm – 2250, Accl: 2210[26], time - 45 sec EBR Cycle: rpm – 300, Accl – 255 [3], time – 30 sec	This is layer 1, which acts as the **adhesion layer**. Care needs to taken while placing the wafer on the spinner chuck. The wafer should be placed such that when the wafer is spun it spins uniformly about the center as much as possible.
14.	Pre-bake I: Hotplate, 65C, 1 min	
15.	Pre-bake II: Oven, 95C, 6 min	
16.	Cool down - ~5 min	

17.	Exposure 15 sec, no mask, flood	Under exposure at this layer will cause tremendous cracking when the next thick layer is processed on it.
18.	Post Exposure Bake: Oven, 95C, 15 min	
19.	Cool Down: ~ 5 min	
20.	Spin Coat Su-8 2100 on a PI spinner Spin Cycle: rpm – 2500, Accl: 2456[29], time - 45 sec EBR Cycle: rpm – 300, Accl – 255 [3], time – 30 sec	This is Layer 2 of the channel network; Su-8 2100 is spun in two steps to get the desired thickness (~250 microns). The idea is to use rpm>2000, so that the final thickness is more uniform
21.	Pre-bake I: Hotplate, 65C, 2 min	
22.	Pre-bake II: Oven, 95C, 55 min	
23.	Cool Down: ~ 5 min	
24.	Spin Coat Su-8 2100 on a PI spinner Spin Cycle: rpm – 2500, Accl: 2456[29], time - 45 sec EBR Cycle: rpm – 300, Accl – 255 [3], time – 30 sec	This is layer 3 of the channel network.
25.	Pre-bake I: Hotplate, 65C, 3 min	
26.	Pre-bake II: Oven, 95C, 55 min	
27.	Cool Down: ~ 5 min	
28.	Exposure: 36 sec at 15mW/cm^2., Through mask, Hard, contact, backside alignment	Mask #3: channels_set 4
29.	Post Exposure Bake Oven, 95C, 60 minute	
30.	Cool Down: ~ 5 min	
31.	Develop: -In SU-8 developer, placed on a magnetic stirrer with “Heat’ setting at ~3 and ‘Stir’ setting at 7. - ~ 12 min, individual wafer, end point based on observation (see comments)	The end point is determined by squirting IPA solution on the SU-8 structures, preferably on the alignment marks. If white residue appears, it means developing is incomplete. Put the wafer

		back into the developer solution and check again after 2 minutes. Repeat until no white residue appears.
32.	Post Development Bake: (optional) Oven, 95C, 15-30 min	After development baking the wafer seems to improve the quality of the features when observed under the microscope. Small cracks and shadow like appearance of the features are seen after development. However, gentle heating at 95 C for about 15-30 minutes can get rid off these small cracks and shadow like appearances.
Formation of Enclosed Microchannels / Bonding		
33.	Start with dehydrated Pyrex wafer with **big seed** patterns on it.	Make sure SU-8 process is applied on the side of the wafer with no metal layers
34.	Spin Coat Su-8 2010 on a PI spinner Spin Cycle: rpm – 2250, Accl: 2210[26], time - 45 sec EBR Cycle: rpm – 300, Accl – 255 [3], time – 30 sec	This is layer 1, which acts as the **adhesion layer**. Care needs to taken while placing the wafer on the spinner chuck. The wafer should be placed such that when the wafer is spun it spins uniformly about the center as much as possible.
35.	Pre-bake I: Hotplate, 65C, 1 min	
36.	Pre-bake II: Oven, 95C, 6 min	
37.	Cool down - ~5 min	
38.	Exposure 15 sec, no mask, flood	Under exposure at this layer will cause tremendous cracking when the next thick layer is processed on it.
39.	Post Exposure Bake: Oven, 95C, 15 min	
40.	Cool Down: ~ 5 min	
41.	Spin Coat Su-8 2010 on a PI spinner Spin Cycle: rpm – 2250, Accl: 2210[26], time	This is Layer 2, first of the two bonding layers

	- 45 sec EBR Cycle: rpm – 300, Accl – 255 [3], time – 30 sec	
42.	Pre-bake: Hotplate, 65C, 2 min	In this case wafer is not subjected to Oven at 95C. It was found that putting the wafer at 95C causes all the solvent in SU-8 to evaporate and that makes it very dry and during bonding this dry SU-8 doesnot flow sufficiently to compensate the thickness non-uniformity of the channel layer and results into inadequate bonding
43.	Exposure I: 5 sec, Blank, Flood	Exposure is done in two steps. First the whole layer is partially exposed so that it becomes nominally hard. The idea is to make the layer hard enough so that they don't flow into the channels during bonding, but soft enough so that there is a weak bong formed with the channel walls.
44.	Exposure II: 10 sec, Through mask, hard, contact, backside alignment, keep the mask on the aligner, it will be used in the next exposure step	Masks: -For "Channels_Set4" use "Cap_Channels_Set4" -For "Depchennels_Set4" use Cap_Depchann_Set4" -For "Depchannels_set5" use "Cap_Depchenn_Set5"
45.	Post Exposure Bake: Hotplate, 65C, 1 min	Post exposure bake is done at a lower temperature and for a shorter period of time to retain some solvent with in the SU-8 layer. The idea is to keep the SU-8 soft enough to flow during the bonding process. However, selected area is sufficiently exposed so that SU-8 on critical areas such as on top

		of the wafer does not flow into the channels and clog them.
46.	Spin Coat Su-8 2010 on a PI spinner Spin Cycle: rpm – 3500, Accl: 3485[41], time - 45 sec EBR Cycle: rpm – 300, Accl – 255 [3], time – 30 sec	
47.	Pre-bake: Hotplate, 65C, 1 min	
48.	Exposure: 10 sec, through mask, hard, contact, back side alignment	Mask: same as step 44
	Bonding in the Bonder	
49.	Measure thickness (x, mm) of the channel wafer (substrate + the structures), thickness (y, mm) of the cap wafer (substrate + SU-8 film)	Take at least 5 point measurement and then use the minimum thicknesses that you get from the measurements.
50.	Determine stack height: x + y + 0.075+3.122	0.075 mm is the thickness of the Pins 3.122 is the thickness of the graphite plate
51.	Set stack height on the bonder	This can be set by rotating the large caliper like scale on top of the bonding chamber
52.	Place channel wafer facing the open channels up wards on the chuck	The chuck has three pins, place “flat” of the wafer according to the pins
53.	Use computer (manual control window) and press the **[F]** button to bring the flags “in”	Pressing the **[F]** button allows the pin to move back and forth
54.	Align and Place cap wafer on to of the pins with the Su-8 layer facing down wards (facing the open channels of the substrate wafer)	Alignment is very important in this step – use the “gross-align” marks to align the cap wafer with the substrate wafer. Note: this kind of alignment is possible when the cap wafer is transparent.
55.	Place the Graphite plate on top of the wafer stack such the metal pins on the graphite pin is facing up wards.	-Make sure the alignment of the wafer is not disturbed while placing the graphite plate.

		-Make sure that the graphite wafer is not placed on top of the pins – this will break the graphite plate
56.	Close the lid of the bonder	Use finger tight to tighten the screws to close the lid.
57.	Use computer (automatic control window) to load the file : SU-8 bond3. aba.	
58.	Press **"Run"**	
59.	Wait a few minutes to confirm the process has started	Check "process monitor" window – it shows the process steps -when each step is done, it will become green and the step that is running will be red. Another way to ensure is to feel if the vacuum pump has started after pressing "Run".
60.	Come back in ~ four hours and take the bonded stack out	Bonded wafer usually gets stuck on the graphite plate – use caution to release the bonded wafer so that the bond is not affected.
Formation of KMPR mold		
61.	Start on the **small seed** patterns side.	
62.	Spin Coat KMPR 1050 on a PI spinner Spin Cycle: rpm – 3000; time - 30 sec EBR Cycle: rpm – 300; time – 30 sec	
63.	Pre-bake: 95C, 15 min, Bake Oven	
64.	Cool Down: ~5 min	
65.	Spin Coat KMPR 1050 on a PI spinner Spin Cycle: rpm – 3000; time - 30 sec EBR Cycle: rpm – 300; time – 30 sec	
66.	Pre-bake: 95C, 40 min, Bake Oven	
67.	Cool Down: ~5 min	
68.	Exposure: 150 sec at 15mW/cm^2., Through mask, Hard, contact, front side alignment	
69.	Post Exposure Bake: Bake Oven, 95C, 5 min	
70.	Cool Down: ~ 30 min	Note that cool down is 30 minutes. It is important that

		you wait 30 minutes to ensure that when you place this side on the vacuum chuck, film do not deform. Colling it 30 minutes as opposed to 5 minutes will help to maintain the film not to be deformed too much
71.	Flip bonded wafers to apply KMPR on the **big seed** side	
72.	Spin Coat KMPR 1050 on a PI spinner Spin Cycle: rpm – 3000; time - 30 sec EBR Cycle: rpm – 300; time – 30 sec	
73.	Pre-bake: 95C, 20 min, Bake Oven	
74.	Cool Down: ~5 min	
75.	Spin Coat KMPR 1050 on a PI spinner Spin Cycle: rpm – 3000; time - 30 sec EBR Cycle: rpm – 300; time – 30 sec	
76.	Pre-bake: 95C, 40 min, Bake Oven	
77.	Cool Down: ~5 min	
78.	Exposure: 150 sec at 15mW/cm^2., Through mask, Hard, contact, backside side alignment	
79.	Post Exposure Bake: Bake Oven, 95C, 15 min	
80.	Cool Down: ~ 5 min	
81.	Develop: -In SU-8 developer, placed on a magnetic stirrer with “Heat’ setting at ~3 and ‘Stir’ setting at 7. - ~ 12-15 min, individual wafer, end point based on observation (see comments)	The end point is determined by squirting IPA solution on the SU-8 structures, preferably on the alignment marks. If white residue appears, it means developing is incomplete. Put the wafer back into the developer solution and check again after 2 minutes. Repeat until no white residue appears.

Appendix C
OGMS magnet Drawings

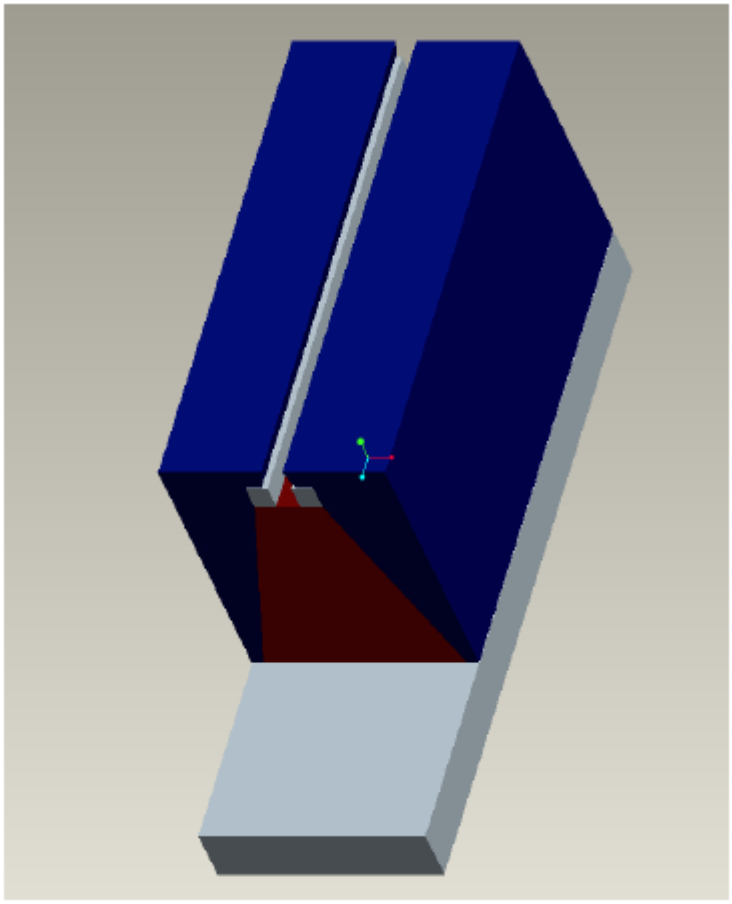

Figure C-1: Isometric view of the OGMS external magnet

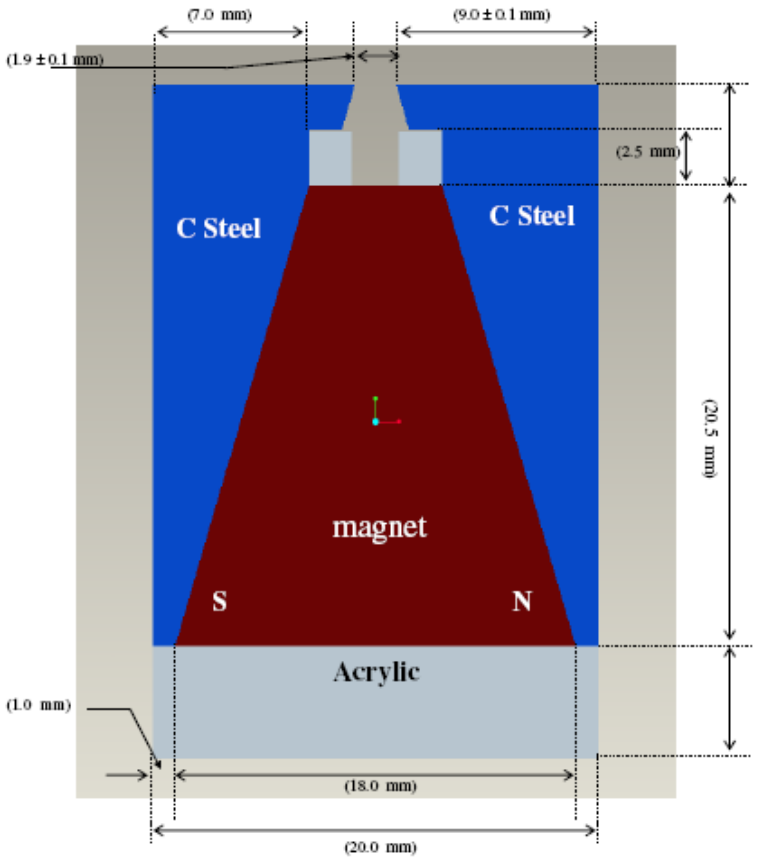

Figure C-2: Side view of the OGMS magnets with dimensions

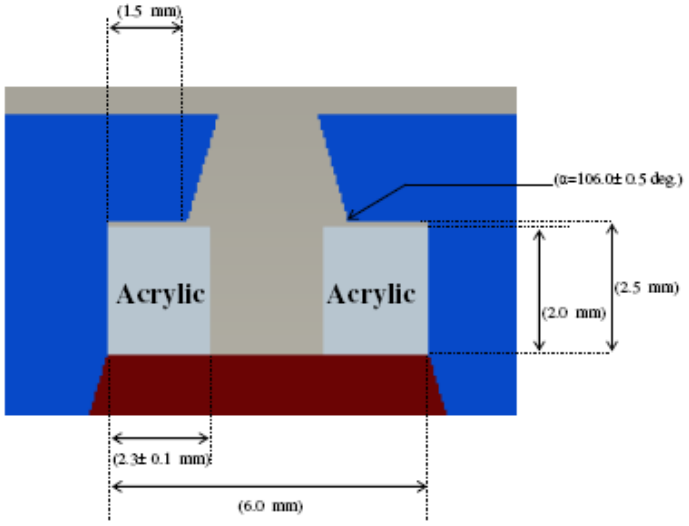

Figure C-3: Close up on the air gap

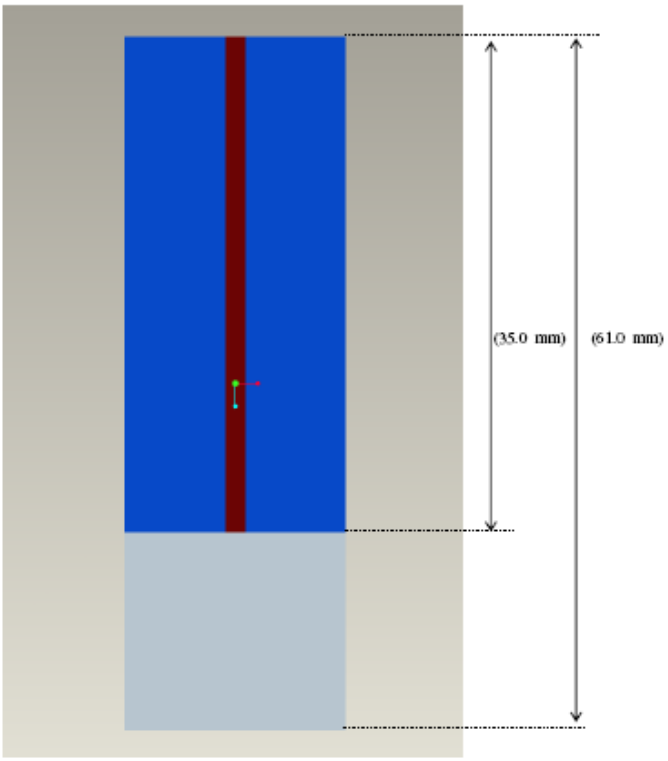

Figure C-4: Side view of the OGMS magnets with dimensions

Appendix D
Multistage bio-ferrograph magnet drawings

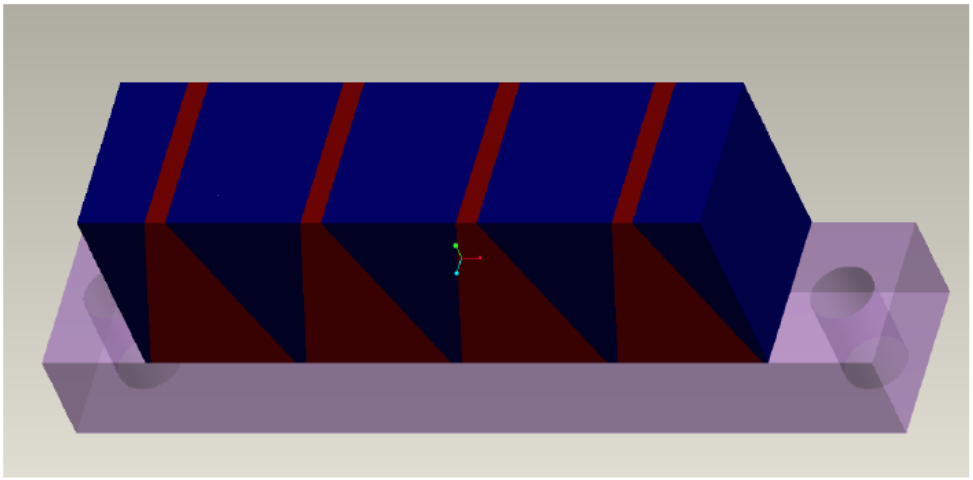

Figure D-1: Isometric view of the multistage bio-ferrograph magnet

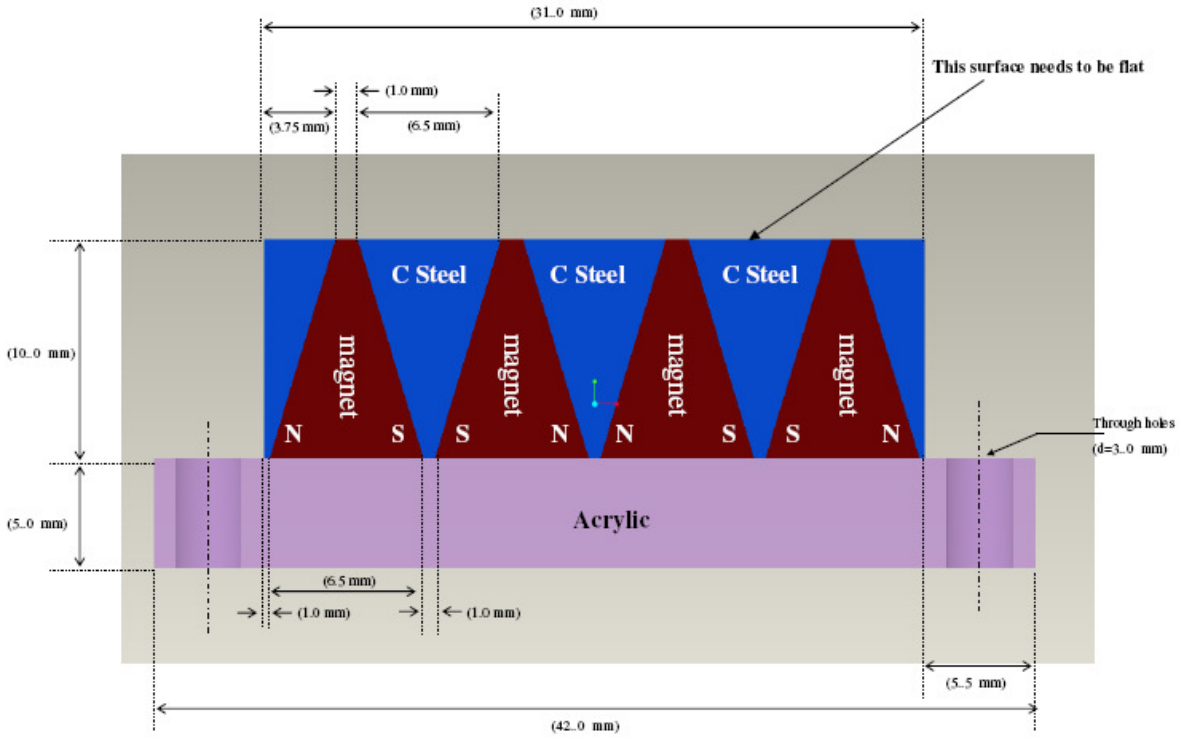

Figure D-2: Side view of the multistage bio-ferrograph magnet with dimensions

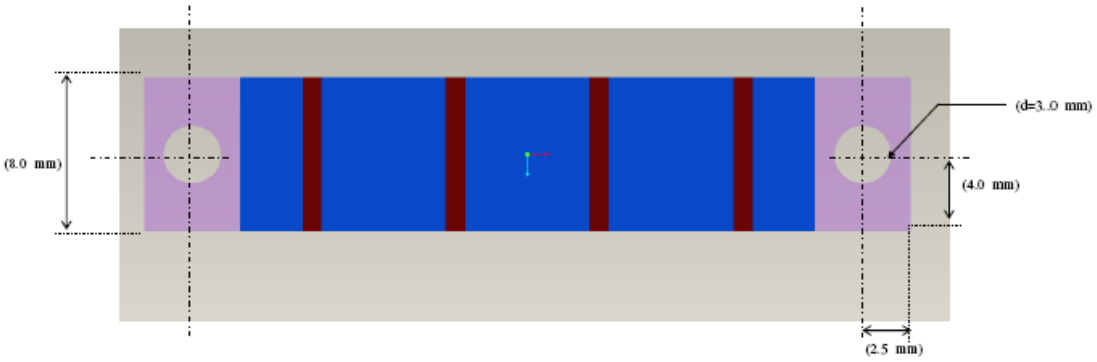

Figure D-3: Top view of the multistage bio-ferrograph magnet with dimensions